In-line synthesis of multi-octave phase-stable infrared waveforms

Hadil Kassab

München 2023

In-line synthesis of multi-octave phase-stable infrared waveforms

Hadil Kassab

Dissertation
der Fakultät für Physik
der Ludwig-Maximilians-Universität
München

vorgelegt von
Hadil Kassab
aus Aleppo

München, den 02.10.2023

Erstgutachter: Prof. Dr. Ferenc Krausz
Zweitgutachter: Dr. Hanieh Fattahi
Tag der mündlichen Prüfung: 28.11.2023

Contents

List of Figures

List of Tables

List of acronyms

AOI: angle of incidence
AR: anti-reflective
CEP: carrier-envelope phase
DFG: difference-frequency generation
DQWG: distributed quasi-waveguide
EFL: effective focal length
EOS: electro-optical sampling
FROG: frequency-resolved optical gating
FRS: field-resolved spectroscopy
FTIR: Fourier-transform infrared
FTL: Fourier-transform limit
FWHM: full-width half-maximum
GDD: group delay dispersion
HHG: high-harmonic generation
HR: highly reflective
HWP: half waveplate
IPDFG: intra-pulse difference-frequency generation
IR: infared
LGS: $LiGaS_2$
MIR: mid-infrared
NIR: near-infrared
OPA: optical parametric amplification
OSA: optical spectrum analyzer
PD: photo diode
ROC: radius of curvature
Sa: sapphire
SFG: sum-frequency generation
SHG: second-harmonic generation
SNR: signal-to-noise ratio
SPF: short pass filter
SPM: self-phase modulation
TFP: thin-film polarizer
THG third-harmonic generation

Ti: Titanium
TOD: third-order dispersion
WP: Wollaston prism
YAG: yttrium aluminium garnet
Yb: Ytterbium
ZnSe: zinc selenide

Zusammenfassung

Die parametrische Abwärtskonvertierung, angetrieben von modernen Hochleistungsquellen mit 10 fs Pulsen im nahen infraroten Bereich (NIR), insbesondere der intrapulsdifferenzfrequenz-generierten IPDFG, ermöglicht eine Kombination von Eigenschaften, die für die molekulare Schwingungsspektroskopie im mittleren infraroten Bereich (MIR) wünschenswert ist: eine breite spektrale Abdeckung, eine hohe Brillanz sowie eine räumliche und zeitliche Kohärenz. Dennoch bleibt die gleichzeitige Implementierung dieser Eigenschaften in einer robusten und kompakten Strahlungsquelle eine bedeutende Herausforderung. In dieser Arbeit behandeln wir diesen Umstand, indem wir verschiedene Konfigurationen der IPDFG untersuchen, jeweils angetrieben von einem 100 W Yb:YAG-Dünnscheiben-Oszillator, welcher nachträglich komprimierte Pulse mit 10,6 fs Dauer bei einer Wiederholungsrate von 10,6 MHz erzeugen kann. Im ersten Teil dieser Arbeit stellen wir kurz die am Anfang dieser Arbeit verfügbare Laserquelle vor, welche Pulse im NIR mit einer zeitlichen Dauer von wenigen Zyklen generieren kann, und konzentrieren uns auf die wichtigsten Modifikationen dieser Laserquelle. Zunächst wurde ein zweistufiger Ansatz zur spektralen Verbreiterung verfolgt, welcher auf dem mehrfachen Durchgang in einer sogenannten „Multi-Pass-Cell“ (MPC) basiert, gefolgt von einer spektralen Verbreiterung in einem verteilten quasi-Wellenleiter (DQWG). Letzteres überwindet die Einschränkungen bei der Feinabstimmung der Dispersion sowie der Nichtlinearität pro Durchgang in einer MPC und der spektralen Sättigung. Im Rahmen dieser Arbeit haben wir eine weitere, vorgeschaltene Pulskompression in der DQWG Stufe eingeführt. Dieser Schritt zur Pulskompression ermöglicht denselben spektralen Verbreiterungsfaktor und vermeidet gleichzeitig eine optische Beschädigung in den nichtlinearen Verbreitungsmaterialien, da diese aufgrund der sehr hohen Spitzenleistungen nahe der materialbedingten Zerstörschwelle betrieben werden. Folglich weist unser modifiziertes System eine erhöhte Stabilität im täglichen Betrieb auf und behält gleichzeitig eine äquivalente zeitliche Pulsdauer sowie Strahlqualität bei. Im zweiten Teil dieser Arbeit stellen wir eine Methode zur Maximierung der Konvertierungseffizienz in der IPDFG bei gleichzeitiger, breiter spektraler Abdeckung vor. Diese Methode verwendet mehrere Kristalle und beinhaltet (i) die Polarisationsoptimierung der Treiberpulse mit einer bichromatischen Wellenplatte (BWP) und (ii) den IPDFG-Prozess mit einer Sequenz aus zwei Kristallen, LiIO3 und $LiGaS_2$. Als Ergebnis wird eine gleichzeitige Abdeckung des spektralen Bereichs von 800 bis 3000 cm^{-1} (bei -30 dB Intensität) mit 130 mW durchschnittlicher Leistung erreicht.

Um das erzeugte IR-Licht von den Treiberpulsen zu trennen, verwenden wir einen eigens hierfür entwickelten und hausintern hergestellten, ultra-breitbandigen Strahlteiler. Darüber hinaus stellen wir ein theoretisches Modell basierend auf der nichtlinearen Wellengleichung vor, um die Aufrechterhaltung der optischen Phasenkohärenz in der hier beschriebenen „in-line“ kollinear Geometrie zu demonstrieren. Dies ermöglicht ein tieferes Verständnis der nichtlinearen Prozesse in den verwendeten Kristallen. Die Simulationsergebnisse zeigen eine gute Übereinstimmung mit den gemessenen Spektren und bestätigen das numerische Modell. Darüber hinaus zeigen die Simulationen die optische Phasenstabilität der erzeugten Strahlung im MIR, mit vernachlässigbarer Variation der zeitlichen Phase über die gesamte Bandbreite am Ausgang der Lichtquelle. Um die Stabilität der Wellenform im MIR, wie theoretisch vorhergesagt, zu überprüfen, haben wir einen Aufbau zur ultra-breitbandigen, elektrooptischen Abtastung (EOS) verwendet. Um ein EOS Signal, das dem optischen elektrischen Feld nahekommt, genau aufzeichnen zu können, haben wir einen 3 µm dünnen GaSe-Kristall verwendet, welcher optisch mit einer 500 µm dicken, aus der chemischen Dampfphase (CVD) hergestellten Diamantplatte verbunden wurde. Diese spezielle Anordnung bietet die kombinierten Vorteile einer ultra-breitbandigen Instrumentenreaktion und der Unterdrückung von mehrfachen Reflexionen innerhalb des EOS-Kristalls, auch „Echoeffekt“ genannt. Diese Ergebnisse ebnen den Weg für kohärente, spektroskopische Verfahren wie beispielsweise der feldaufgelösten und Frequenzkamm-Spektroskopie, sowie der nichtlinearen, ultraschnellen Spektroskopie und der Synthese optischer Wellenformen im gesamten Bereich des infraroten, molekularen Fingerabdrucks.

Abstract

Parametric downconversion driven by modern, high-power sources of 10-fs-scale near-infrared pulses, in particular intrapulse difference-frequency generation (IPDFG), affords combinations of properties desirable for molecular vibrational spectroscopy in the mid-infrared range: broad spectral coverage, high brilliance, and spatial and temporal coherence. Yet, unifying these in a robust and compact radiation source has remained a key challenge. In this thesis, we address this need by investigating IPDFG in several configurations, driven by the 100-W-level, 10.6-fs pulses of a 10.6-MHz-repetition-rate, nonlinearly post-compressed Yb:YAG thin-disk oscillator.

The first part of this work, briefly reviews the few-cycle near-infrared (NIR) laser source available at the beginning of the doctorate, focusing on the main modifications. Initially, a dual-stage multi-pass cell (MPC) spectral broadening approach was used, followed by spectral broadening employing a distributed quasi-waveguide (DQWG). The latter approach overcomes the limitations of fine-tuning the per-pass dispersion, nonlinearity within MPCs, and spectral saturation. This work introduced an intermediate temporal pulse compression in the DQWG. This pulse compression step enables the same spectral broadening factor while avoiding any optical damage in the nonlinear broadening media when exposed to very high peak power intensity on the level of the material damage threshold. Consequently, our system exhibits increased day-to-day stability while maintaining equivalent temporal pulse duration and beam quality factor.

Subsequently, we present a method to maximize conversion efficiency in IPDGF while achieving broad spectral coverage. This method employs several crystals and involves (i) polarization tailoring of the driving pulses using a bichromatic waveplate (BWP) and (ii) the IPDFG process using a sequence of two crystals, LiIO3 and $LiGaS_2$. As a result, simultaneous coverage of the 800 to 3000 cm^{-1} spectral range (at -30-dB intensity) is achieved with 130 mW of average power. Additionally, we introduce a new design of an ultra-broadband beam splitter, manufactured in-house, to separate the generated IR light from the driving pulses.

To demonstrate the maintenance of optical-phase coherence in the in-line geometry, a theoretical modeling approach based on the nonlinear wave equation is presented. This provides a deeper understanding of the nonlinear processes in the crystals. The simulation results show good agreement with the measured spectra, validating the numerical model. Moreover, the simulations confirm the optical-phase stability of the generated mid-IR radiation, with negligible variation in the temporal phase across the output bandwidth.

In order to verify the stability of the mid-IR waveform as predicted theoretically, we utilized an ultra-broadband electro-optic sampling (EOS) setup. To achieve this goal and accurately record an EOS signal that closely resembles the optical electric field, we used a 3-µm-thin GaSe crystal, which was optically contacted onto a 500-µm-thick CVD (chemical vapor deposition) diamond plate. This particular assembly offers the combined benefits of an ultra-broadband instrument response and effectively suppresses multiple reflections (that is, the "echo effect") within the EOS crystal.
These results pave the way for coherent spectroscopy schemes, such as field-resolved and frequency-comb spectroscopy, as well as nonlinear, ultrafast spectroscopy and optical-waveform synthesis across the entire infrared molecular fingerprint region.

Chapter 1

Introduction and Outline

1.1 Introduction and motivation

Optical spectroscopy is a ubiquitous tool used in scientific disciplines including physics, chemistry, and the biosciences [8, 35, 78, 93, 98]. It involves the interaction between light and matter, such as atoms, molecules, gases, liquids, and solids. One particular branch of optical spectroscopy probes vibrations of molecular bonds. Two commonly employed techniques for studying these vibrations are Raman spectroscopy and infrared (IR) spectroscopy. Raman spectroscopy detects inelastically scattered light to gather molecular information [69, 74], while infrared spectroscopy measures light absorption and re-emission [13, 54]. Both methods provide sample-specific signals which are often dubbed "molecular fingerprints" in reference to their uniqueness.

Traditional Fourier transform infrared (FTIR) spectroscopy has been the gold standard for vibrational spectroscopy since its first demonstration in 1956 [50]. It possesses advantages over dispersive spectrometers, such as the ability to simultaneously record information from all spectral elements (multiplex advantage) and increased irradiance on the detector (throughput advantage) [54]. However, FTIR spectrometers using thermal sources have limitations in terms of brightness, and spatial and temporal coherence.

In Fig. 1.1 (adapted from [60]), the infrared molecular fingerprints (IMFs) acquired encompassed the spectral range spanning from 1000 and 3000 cm^{-1} and were measured utilizing FTIR spectrometer. This range includes distinctive absorption bands associated with proteins (such as amide I/II, mainly at 1548 cm^{-1} and 1654 cm^{-1}), carbohydrates (mostly within 1000 to 1200 cm^{-1}), and lipids (1741 cm^{-1}, 2854 cm^{-1} and 2929 cm^{-1}) [60].

In the time domain, the availability of a shorter mid-infrared (MIR) pulse improved the contrast, thus ensuring exceptional sensitivity, which is crucial for high-sensitivity spectroscopy in biomedical applications. Aside from the instrument's capacity to record electric fields with great sensitivity, the temporal characteristics of FRS (Field Resolved Spectroscopy) ensure the resilient detection of molecular emission, even in the presence of excitation fluctuations [109, 63].

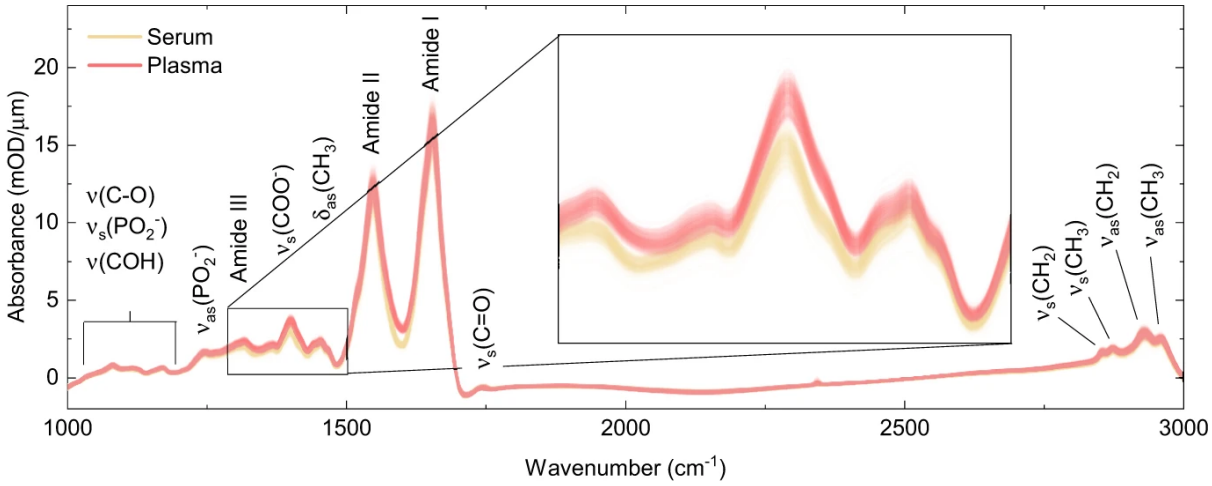

Figure 1.1: Unprocessed infrared absorption spectra of liquid blood sera (yellow) and plasma samples (red) were measured from 318 participants utilizing an FTIR spectrometer. Inset: Close-up showing 636 individual traces of 318 blood sera and plasma measurements each. The absorption peaks are associated with the major molecular vibrations: ν stretching, δ bending, symmetric, and asymmetric vibrations. Figure adapted from [60]

Large-scale facilities like synchrotrons [6] and free-electron lasers [39] can provide high-brightness broadband IR radiation, but are not practical for everyday measurements. Striving to find ways to overcome these limitations, advances in femtosecond laser technology have offered a promising alternative for precise optical metrology and spectroscopy. Modelocked laser architectures generate highly reproducible pulses with durations in the femtosecond range [24]. Although these ultrashort-pulse sources are mostly limited to the near-infrared and visible spectral regions, frequency down-conversion processes have been utilized to generate femtosecond laser pulses in the mid-infrared range [110].

One prominent upconversion process underlying technologies reaching high precision for temporal as well as frequency-domain optical measurements has been intrapulse difference-frequency generation (IPDFG) [31]. These advancements have led to the development of MIR laser sources with broad bandwidth, high average power, and excellent coherence characteristics [26, 48, 124, 146]. The femtosecond MIR laser sources generate pulses significantly shorter than the typical dephasing time of molecular vibrations, enabling the background-free observation of resonant MIR molecular vibrations in the time domain [83].

Field-resolved spectroscopy (FRS) is a technique that combines waveform-stable MIR pulses with electro-optic sampling (EOS) to detect the electric field emitted by sample molecules following impulsive excitation [110]. FRS offers advantages over conventional techniques, as the signal strength scales linearly with the electric field of the MIR waveform. This makes FRS suitable for studying thick and strongly attenuating samples,

as well as for rapidly dephasing molecular vibrations in biological samples [61, 63, 109]. FRS, profiting from high-brightness, temporally coherent laser sources, as well as from high-sensitivity field-resolved detection, offers increased molecular detection sensitivity in vibrational spectroscopy. It directly reveals the complete amplitude and phase information of the sampled radiation. FRS mitigates the need for noisy MIR detectors by detecting in the NIR spectral region, where detectors with lower noise are available [54]. The temporal resolution and background-free nature of FRS allow for the observation of the free induction decay of vibrationally excited molecules with picosecond decay times[83].
Our team specializes in the development of tools for this purpose. To perform FRS, we employ high-power, ultrashort NIR pulses that are focused onto a nonlinear crystal for IPDFG. The latter results in broadband infrared (IR) spectra covering the molecular fingerprint region, ensuring simultaneous detection of resonances from different molecules and bonds.
Figure 1.2 (adapted from [63]) demonstrates the measurement of the temporal response using an ultrashort MIR excitation pulse. This allows the sample's molecular response to be separated from the stronger excitation energy. By reducing the interference of excitation fluctuations with the trailing molecular response, the weaker signal from the former can be extracted by subtracting the reference signal from the sample measurement. After a few hundred femtoseconds, the adverse impact of source noise on the subtraction outcome becomes insignificant due to the swift decay of the excitation pulse. This creates an opportunity to conduct background-free measurements of the molecular signal [109].

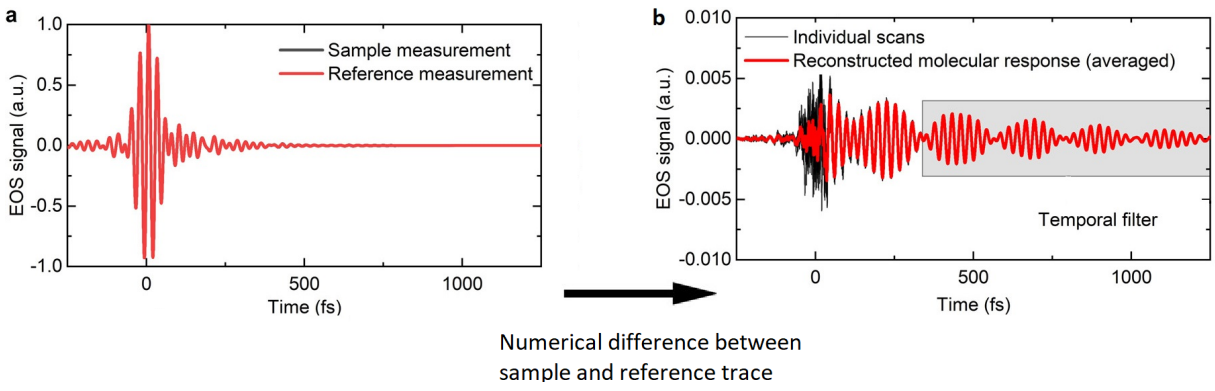

Figure 1.2: FRS measurement of a solution of DMSO2 in water. (a) EOS traces of a reference and a test sample (a liquid cuvette filled with pure water and one with a 1 mg/mL solution of DMSO2 in water, respectively). The difference between the two traces is small (it cannot be discerned by the eye). (b) The molecular response in the time domain of DMSO2 was obtained by subtracting the sample from the reference trace numerically, as shown in (a). The figure is adapted from [63]

At the beginning of this doctoral work, the key limitation of FRS technology available for biomedical applications was the restricted bandwidth of both the sources and the

detection capabilities. Furthermore, these first-generation spectrometers primarily probed the linear susceptibility of samples, further narrowing the range of obtainable information. Thus, the major goal of this work was to extend the bandwidth of electric-field-resolved molecular fingerprinting and, thereby, biomedical spectroscopy. The necessity for a broadband MIR laser source is paramount to achieving simultaneous resonance detection and enhanced contrast, ultimately facilitating breakthroughs in biomedical research and analysis. It was furthermore the goal to demonstrate the feasibility of generating broadband MIR pulses with energies high enough to be suitable for multi-dimensional nonlinear spectroscopy, and repetition rates in the MHz range. The latter is a necessary prerequisite for the practicability of large-scale measurement campaigns.

1.2 Structure of the work

After providing an introduction and motivation in this chapter, the key nonlinear optical processes that have been exploited in the framework of the laboratory's experimental work are presented in **Chapter 2**. These processes include frequency down- and up-conversion via $\chi^{(2)}$ and $\chi^{(3)}$ nonlinearities as well as self-induced nonlinear processes such as self-phase modulation.
Chapter 3 covers details of the laser front-end, a Kerr-lens mode-locked femtosecond oscillator, in which the (Yb)-doped gain material is in a thin-disk geometry [107], and which is complemented with extra-cavity pulse compression based on nonlinear spectral broadening and temporal recompression [55].
Building upon the results obtained in the preceding chapter, **Chapter 4** describes the development of a multi-octave waveform-stable MIR source. Experimental setups for MIR generation employing an intra-pulse difference frequency generation are presented, where few-cycle near-infrared laser pulses have been used to drive the process in a multi-crystal in-line geometry.
Chapter 5 discusses the numerical and experimental verification of the optical-phase stability of the polarization-tailored multi-crystal IPDFG source to closely approach the real electric field of the MIR pulses. The experimental part of this chapter presents an electro-optic sampling detection instrument.
Lastly, **Chapter 6** provides a summary of the experimental findings and offers an outlook on future prospects.

Chapter 2

Theory of ultrafast nonlinear optics

2.1 Introduction

Our understanding of light and its interaction with matter has been built and developed over the course of many centuries. Since about 500 BC numerous theories have emerged. While a thorough review would exceed the scope of this work, here we survey the most important theories on light [137]:

1. Newton's corpuscular theory of light: Isaac Newton suggested that light consists of non-spherical particles (corpuscles), having different sizes based on their color. This was the basis of his corpuscular theory of light, where the propagation laws of these particles were explained and published in 1704.

2. Huygens wave theory: Christiaan Huygens supported the wave nature of light, which was later published in his work, Treatise on Light, in 1690. Huygens postulated that light is a longitudinal wave propagated through the aether medium, which is believed to permeate the entire universe. According to his theory, a wavefront is formed by a group of particles oscillating in phase with each other. In the case of point sources, spherical wavefronts are emitted, while sources located at infinity generate plane wavefronts.

3. Maxwell's electromagnetic wave theory: James Clerk Maxwell identified light as an electromagnetic wave and in 1864 formulated the electromagnetic wave equations. Later Oliver Heaviside reformulated these equations using vector notation, which simplified their mathematical representation and facilitated further developments in electromagnetism. Nowadays, this classical electrodynamics theory is widely used in physics and engineering.

4. Planck's radiation law: in 1900 Planck derived a formula for blackbody radiation based on a concept of quantized emitted energy. This formula was built on the idea that the radiation from oscillating molecules is not continuous but was emitted in discrete strands of energy called quanta [105, 106].

Those groundbreaking theories helped scientists over the last decades to develop tools that enabled precise control over the electric field of light. In recent years many advanced tools came out, for example, those that revealed the time-domain nature of vacuum fluctuations and the time-domain nature of the quantum optical properties of light[114]. Most of the photonic tools and phenomena developed in the frame of this work can be conveniently explained using classical electromagnetic theory, i.e. "Maxwell's theory". We deliberately chose the simplest theory, because it is the most suitable one for the theoretical framework of this thesis and it works very well for our measurement uncertainty. Some effects and phenomena that are not accounted for by Maxwell's theory are: quantum-mechanical effects, fine structure of spectral lines, electron spin, and magnetic moments, high-energy particle interactions, and gravitational effects.

2.2 Introduction to nonlinear optics

Nonlinear optics comprises the phenomena that occur as a result of the modification of the optical properties of a material by the presence of intense light, for example, laser light. The beginning of the field of nonlinear optics goes back to the discovery of the second harmonic generation phenomenon in 1961 [45], shortly after the development of the first laser by Theodore Maiman.
Optical phenomena are referred to as "nonlinear" when they occur due to a nonlinear response of a material system to the strength of the applied optical field. A strong optical field, for example, in the range of few 10^{15}-10^{12} W/cm^2, is sufficient to induce a slight dynamic separation of bound charges, between atomic nuclei and electrons in the material. This induces electric dipole moments or what is commonly referred to as electric displacement field given by:

$$\overrightarrow{\mathbf{D}}(\omega) = \epsilon_0 \overrightarrow{\mathbf{E}}(\omega) + \overrightarrow{\mathbf{P}}(\omega). \tag{2.1}$$

Here $\mathbf{P}(\omega)$ is the dipole moment per unit volume, or polarization density, of a material system and it depends on the strength $\mathbf{E}(\omega)$ of an applied optical field. In a linear, homogeneous, and isotropic medium, this dependency is given by the following relationship:

$$\overrightarrow{\mathbf{P}}(\omega) = \epsilon_0 \chi^{(1)}(\omega) \overrightarrow{\mathbf{E}}(\omega) \tag{2.2}$$

in the frequency domain, and

$$\overrightarrow{\mathbf{P}}(t) = \epsilon_0 \chi^{(1)} * \overrightarrow{\mathbf{E}}(t) \tag{2.3}$$

in the time domain, where $\chi^{(1)}$ the linear susceptibility and ϵ_0 is the permittivity of free space.

Substituting 2.2 in 2.1 gives:

$$\overrightarrow{\mathbf{D}}(\omega) = \epsilon_0 (1 + \chi^{(1)}(\omega)) \overrightarrow{\mathbf{E}}(\omega) = \epsilon(\omega) \overrightarrow{\mathbf{E}}(\omega) \tag{2.4}$$

The time derivation of the electric displacement field gives the **displacement current density**:

$$\overrightarrow{\mathbf{J}_D} = \frac{\partial \overrightarrow{\mathbf{D}}\,(t)}{\partial t} = \epsilon_0 \frac{\partial \overrightarrow{\mathbf{E}}\,(t)}{\partial t} + \frac{\partial \overrightarrow{\mathbf{P}}\,(t)}{\partial t}. \tag{2.5}$$

If the material is nonmagnetic we can write:

$$\mathbf{B}(t) = \mu_0 \mathbf{H}(t) \tag{2.6}$$

where $\mathbf{H}$ is magnetic field strength. However in the case of vacuum, $\mathbf{P}(t)$ becomes

$$\mathbf{P}(t) = 0. \tag{2.7}$$

In a medium with no free charges, $\nabla \cdot \mathbf{E}$ will be equal to zero, and in the absence of free currents $\mathbf{J}(t)$ will also be equal to zero. However, we allowed for local (bound) charges to describe the nonlinear response of materials to an external electric field $\mathbf{E}(t)$ and, thus, **Maxwell's equations** can be re-written as:

$$\nabla \cdot \overrightarrow{\mathbf{E}} = 0 \tag{2.8}$$

$$\nabla \cdot \overrightarrow{\mathbf{B}} = 0 \tag{2.9}$$

$$\nabla \times \overrightarrow{\mathbf{E}} = -\frac{\partial \overrightarrow{\mathbf{B}}}{\partial t} \tag{2.10}$$

$$\nabla \times \overrightarrow{\mathbf{B}} = \frac{1}{c_0^2}\frac{\partial \overrightarrow{\mathbf{E}}}{\partial t} + \mu_0 \frac{\partial \overrightarrow{\mathbf{P}}}{\partial t} = \mu_0 \cdot \overrightarrow{\mathbf{J}_D}. \tag{2.11}$$

When **low irradiance** is applied to a linear medium, (i) the polarization will be

$$\mathbf{P}(\omega) \sim \mathbf{E}(\omega) \tag{2.12}$$

and (ii) the deviation of the wave equation is as follows:

$$\Delta \mathbf{E}(t) - \frac{1}{c_0^2}\frac{\partial^2 \mathbf{E}(t)}{\partial t^2} = \mu_0 \frac{\partial^2 \mathbf{P}(t)}{\partial t^2} \tag{2.13}$$

in the time domain, and

$$\Delta \mathbf{E}(\omega) - \frac{1}{c_0^2}(i\omega)^2 \mathbf{E}(\omega) = \mu_0 (i\omega)^2 \mathbf{P}(\omega) \tag{2.14}$$

in the frequency domain, where $\epsilon_0 \mu_0 = \frac{1}{c_0^2}$.

By substituting 2.4 in the 2.14 and considering propagation in Z-direction only we obtain:

$$\frac{\partial^2 \mathbf{E}(\omega)}{\partial z^2} + \frac{1+\chi^{(1)}(\omega)}{c_0^2}\omega^2 \mathbf{E}(\omega) = 0 \tag{2.15}$$

and the solution will be:

$$\forall \omega : \mathbf{E}(z,t) = \sum_{\omega_i} \mathbf{E}_0 \cos(\omega_i t - k(\omega_i) z) \tag{2.16}$$

where: $\omega = c(\omega) \cdot k(\omega)$, $c(\omega) = \frac{c_0}{n(\omega)}$ and $n(\omega) = \sqrt{1+\chi^{(1)}(\omega)}$ is the **linear refractive index**.
We see from 2.16 that the general solution of the wave equation is a phase-coherent superposition of monochromatic solutions.

In the **high irradiance** case, the connection between the induced polarization and the electric field can lose its linearity. Then, $\mathbf{P}(\omega) \neq \mathbf{E}(\omega)$ and the assumption we made in (2.58) is no longer valid, neither in the time domain nor in the frequency domain. This implies that a new expression for $\vec{\mathbf{P}}$ and a suitable wave equation to describe the problem are needed.
For illustration purposes, we will make a strong assumption that $\mathbf{P}$ is instantaneous, i.e. the nonlinear susceptibility is ω-independent. Under this assumption, we can expand $\mathbf{P}(t)$ as a Taylor series in $\mathbf{E}$:

$$\begin{aligned} P(t) &= P^{(1)}(t) + P^{(2)}(t) + P^{(3)}(t) + \cdots \\ &= P^{(1)}(t) + P^{\text{Nonlinear}}(t) \\ &= P^{\text{L}}(t) + P^{\text{NL}}(t) \\ &= \epsilon_0 \left[\chi^{(1)} E(t) + \chi^{(2)} E^2(t) + \chi^{(3)} E^3(t) + \cdots\right] \end{aligned} \tag{2.17}$$

The case where $\mathbf{P}$ is not instantaneous will be discussed in the following section. The last section of this chapter aims to provide more in-depth explanations of the key nonlinear optical processes, particularly those that form the theoretical foundation of the lab's experimental work. An illustration of one such process, *surface second harmonic generation*, is shown in Fig. 2.1. This process is a unique form of second harmonic generation that occurs due to the break in the symmetry of the electronic potential caused by a material interface [16].

2.3 Wave equation in nonlinear media

When $\mathbf{P}$ is noninstantaneous, we will not be able to expand $\mathbf{P}(t)$ as Taylor series in $\mathbf{E}$, but as **Volterra series** as follows:

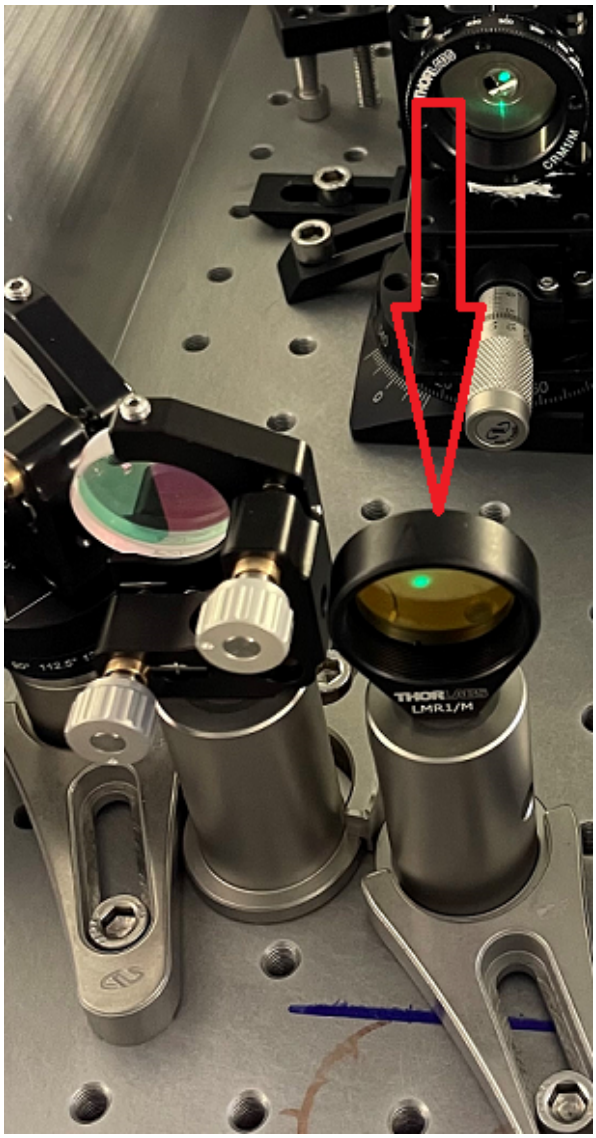

Figure 2.1: A practical example of surface second harmonic generation of a laser beam at a wavelength of 1030 nm. While the fundamental laser beam is invisible, its second harmonic is visible and appears green, corresponding to a wavelength of 515 nm.

$$
\begin{aligned}
P(t) &= P^{(1)}(t) + P^{(2)}(t) + P^{(3)}(t) + \cdots \\
&= \epsilon_0 \int_{t_1<t} \chi^{(1)}(t_1) E(t-t_1)\, dt_1 \\
&+ \epsilon_0 \iint_{t_1,t_2<t} \chi^{(2)}(t_1,t_2) E(t-t_1) E(t-t_2)\, dt_1\, dt_2 \\
&+ \epsilon_0 \iiint_{t_1,t_2,t_3<t} \chi^{(3)}(t_1,t_2,t_3) E(t-t_1) E(t-t_2) E(t-t_3)\, dt_1\, dt_2\, dt_3 \\
&+ \cdots
\end{aligned}
\tag{2.18}
$$

It is important to know that $\chi^{(2)}$, $\chi^{(3)}$ and higher-order nonlinearities like $\chi^{(1)}$ describe the properties of the material (sample). However, $\chi^{(3)}$ occurs in all media (no symmetry breaking is required) and can be measured by many nonlinear spectroscopic techniques.

To propagate waves, we consider a *driven* wave equation.
From Maxwell's equations, we obtain:

$$\nabla(\nabla \cdot \mathbf{E}) - \nabla^2 \mathbf{E} = -\frac{\partial}{\partial t}(\nabla \times \mathbf{B}) \tag{2.19}$$

By assuming that there are no free currents $\mathbf{J}(t) = 0$ and that the material is non-magnetic $\mathbf{B} = \mu_0 \mathbf{H}$, we can write:

$$\nabla \times \mathbf{B} = \mu_0 (\nabla \times \mathbf{H}) = \mu_0 \frac{\partial \mathbf{D}}{\partial t} \tag{2.20}$$

where we have applied Ampere's law in the last step.

Combining (2.19) and (2.20) gives:

$$\nabla(\nabla \cdot \mathbf{E}) - \nabla^2 \mathbf{E} = -\mu_0 \frac{\partial^2 \mathbf{D}}{\partial t^2} \tag{2.21}$$

Recall that the electric displacement field $\mathbf{D}$ is defined as:

$$\mathbf{D} = \epsilon_0 \mathbf{E} + \mathbf{P} \tag{2.22}$$

If we substitute (2.22) into (2.21), and remember that $c_0 = \frac{1}{\sqrt{\epsilon_0 \mu_0}}$, we will have:

$$\begin{aligned} \nabla(\nabla \cdot \mathbf{E}) - \nabla^2 \mathbf{E} &= -\epsilon_0 \mu_0 \frac{\partial^2 \mathbf{E}}{\partial t^2} - \mu_0 \frac{\partial^2 \mathbf{P}}{\partial t^2} \\ &= -\frac{1}{c_0^2} \frac{\partial^2 \mathbf{E}}{\partial t^2} - \mu_0 \frac{\partial^2 \mathbf{P}}{\partial t^2} \end{aligned} \tag{2.23}$$

In many cases of interest, the term $\nabla(\nabla \cdot \mathbf{E})$ is negligible. For example, if $\mathbf{E}(t)$ is a transverse infinite-plane wave, we will have $\nabla \cdot \mathbf{E} = 0$. Moreover, in a slow-varying amplitude approximation, $\nabla(\nabla \cdot \mathbf{E})$ is small and can be neglected. The slowly varying amplitude (SVA) method enables the separation of the rapid oscillations of a wave from the gradual changes in its envelope. This approach assumes that the envelope of the wave varies slowly compared to the scale of the oscillations. By making this assumption, the mathematical description of the wave can be simplified, leading to approximate equations that are more easily solvable [7].

By setting $\nabla(\nabla \cdot \mathbf{E}) = 0$, we obtain the wave equation in the time domain:

$$\Delta \mathbf{E} = \frac{1}{c_0^2} \frac{\partial^2 \mathbf{E}}{\partial t^2} + \mu_0 \frac{\partial^2 \mathbf{P}}{\partial t^2} \tag{2.24}$$

The Fourier transform with respect to time is given by:

$$\widetilde{\mathbf{E}}(\omega) = \int \mathbf{E}(t) e^{i\omega t}\, dt \tag{2.25}$$

If we perform the Fourier transform on (2.25), we obtain the driven wave equation in the frequency domain:

$$\Delta\widetilde{\mathbf{E}} = \frac{1}{c_0^2}\,(i\omega)^2\,\widetilde{\mathbf{E}} + \mu_0 (i\omega)^2 \widetilde{\mathbf{P}} \tag{2.26}$$

Now we make the ansatz:

$$\widetilde{\mathbf{E}} = \widetilde{\mathbf{U}} e^{-ikz} \tag{2.27}$$

$$\widetilde{\mathbf{P}} = \widetilde{\mathbf{P}}_{cmc} e^{-ikz} \tag{2.28}$$

where "cmc" stands for co-moving coordinates for $k(\omega) = n(\omega)\frac{\omega}{c_0}$.

We leave out the tilde for simplicity and plug the ansatz into (2.26), the left-hand side becomes:

$$\begin{aligned}
\Delta\mathbf{E} = \Delta_\perp \mathbf{E} + \partial_z^2 \mathbf{E} &= (\Delta_\perp \mathbf{U})\, e^{-ikz} + \partial_z^2 \left(\mathbf{U} e^{-ikz}\right) \\
&= (\Delta_\perp \mathbf{U})\, e^{-ikz} + \partial_z \left[\partial_z \mathbf{U} \cdot e^{-ikz} + (-ik)\mathbf{U} e^{-ikz}\right] \\
&= \left[\Delta_\perp \mathbf{U} + \partial_z^2 \mathbf{U} + \partial_z \mathbf{U}\,(-ik) + (-ik)\,\partial_z \mathbf{U} + (-ik)^2\,\mathbf{U}\right] e^{-ikz} \\
&= \left(\Delta_\perp \mathbf{U} + \partial_z^2 \mathbf{U} - 2ik\partial_z \mathbf{U} - k^2 \mathbf{U}\right) e^{-ikz}
\end{aligned} \tag{2.29}$$

and the right-hand side becomes:

$$\begin{aligned}
\frac{1}{c_0^2}\,(i\omega)^2\,\mathbf{E} + \mu_0 (i\omega)^2 \mathbf{P} &= -\frac{\omega^2}{c_0^2}\mathbf{E} - \mu_0 \omega^2 \mathbf{P} \\
&= \left(-\frac{\omega^2}{c_0^2}\mathbf{U} - \mu_0 \omega^2 \mathbf{P}_{cmc}\right) e^{-ikz}
\end{aligned} \tag{2.30}$$

Combining the results from (2.29) and (2.30) gives:

$$\Delta_\perp \mathbf{U} + \partial_z^2 \mathbf{U} - 2ik\partial_z \mathbf{U} - k^2 \mathbf{U} = -\frac{\omega^2}{c_0^2}\mathbf{U} - \mu_0 \omega^2 \mathbf{P}_{cmc} \tag{2.31}$$

In one dimension, the first term on the left $\Delta_\perp \mathbf{U}$ is zero, and under the slowly evolving wave approximation, the second term on the left $\partial_z^2 \mathbf{U}$ is negligible as well. Therefore, we can rewrite (2.31) as:

$$\frac{\partial \mathbf{U}(\omega)}{\partial z} = \frac{\frac{\omega^2}{c_0^2} - k^2}{2ik}\mathbf{U}(\omega) + \frac{\mu_0 \omega^2}{2ik}\mathbf{P}_{cmc}(\omega) \tag{2.32}$$

The "slowly evolving wave approximation" (SEWA) is a mathematical technique used to simplify the analysis of wave propagation in systems where the wave frequency or phase

varies slowly compared to other temporal or spatial variations. The assumption is made that the wave's envelope changes slowly over a given scale compared to the rapid oscillations of the carrier wave. [17].
Equation (2.32) is the first-order one-dimensional propagation equation (FOP) in the frequency domain, which is a valuable tool for analyzing wave propagation and understanding dispersion effects. It provides a simplified mathematical framework for studying wave propagation compared to more complex full-wave equations because it allows for approximations and analytical solutions in situations where the slowly varying amplitude approximation or slowly evolving wave approximation is applicable.
For example, in the framework work of this thesis and to build a theoretical understanding of the nonlinear processes that occur in crystals, we modeled these effects numerically employing the nonlinear wave equation in the slowly-evolving wave approximation [72].
In the following section, we will focus on the nonlinear processes which have been exploited in the framework of the experiments. We will briefly describe those processes, in particular, the ones that can occur in a lossless medium; we will show how they can be described in terms of the nonlinear contribution to the polarization given by (2.17) [141].

2.4 Description of prominent nonlinear optical processes

There are two types of nonlinear optical processes, parametric processes, and nonparametric processes. In the parametric ones, the susceptibility is real, and the photon energy is conserved. However, in the nonparametric processes, this is not the case, where it involves the transfer of population from one *real* energy level to another, the susceptibility is complex, and the photon energy is not conserved due to energy transfer to or from the material. While perturbative nonlinear processes (those, for which the Volterra series converges) can be phenomenologically described by the higher-order susceptibilities, adding quantum-mechanical considerations provides a deeper understanding of the interaction of light with matter.

2.4.1 Second-harmonic generation

Let us consider the second harmonic generation process of a monochromatic wave, which is illustrated schematically in Fig. (2.2). Here, a laser beam whose electric field strength is given as

$$\widetilde{E}(t) = Ee^{-i\omega t} + c.c. \tag{2.33}$$

impinges on a nonlinear crystal with second-order susceptibility $\chi^{(2)} \neq 0$. This will result in creating a nonlinear polarization which can be expressed as:

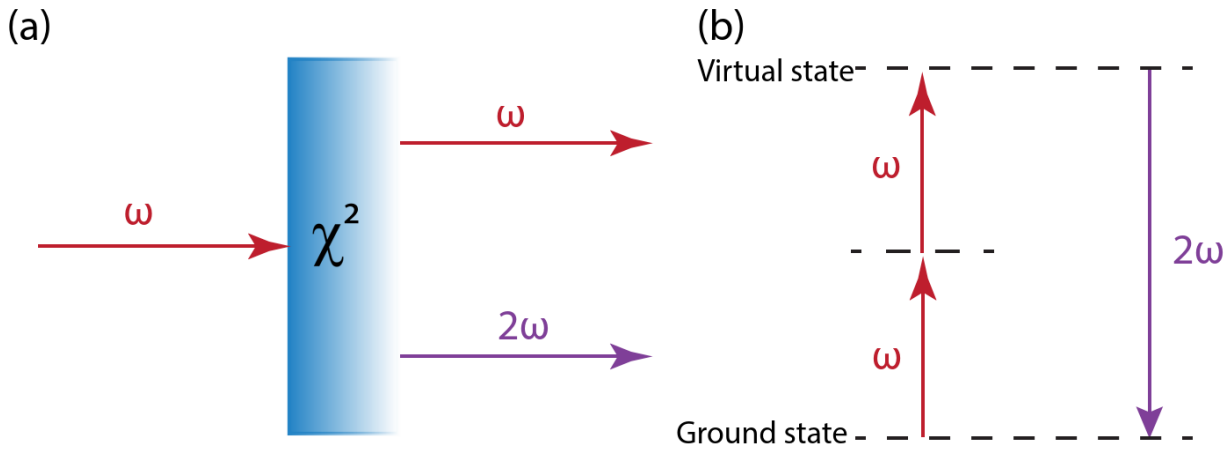

Figure 2.2: (a) Second-harmonic generation geometry. The figure depicts the process of converting a monochromatic wave into its second harmonic frequency using a nonlinear crystal with a non-zero second-order susceptibility $\chi^{(2)}$ (b) A diagram of energy levels that illustrates second-harmonic generation.

$$\widetilde{P}^{(2)}(t) = \epsilon_0 \chi^{(2)} \widetilde{E}(t)^2 = 2\epsilon_0 \chi^{(2)} E E^* + (\epsilon_0 \chi^{(2)} E^2 e^{-i2\omega t} + c.c.). \tag{2.34}$$

The second-order polarization consists of a contribution at zero frequency (the first term) and a contribution at frequency 2ω (the second term). According to the wave equation in the time domain (2.24), the latter contribution can lead to the generation of radiation at the second harmonic frequency. Whereas the first contribution in equation (2.34) does not lead to the generation of electromagnetic radiation, because its second-time derivative vanishes. However, it leads to a process known as optical rectification, in which a static electric field is created across the nonlinear crystal [141].
One common use of second-harmonic generation is in frequency-resolved optical gating (FROG) to measure the spectral phase of ultrashort laser pulses. Second-harmonic generation can be understood by considering the interaction in terms of the exchange of photons between the different frequency components of the field. This is illustrated in part (b) of (2.2), where two photons of frequency ω are destroyed, and at the same time a photon of frequency 2ω is created. The dashed line at the bottom in (2.2) represents the atomic ground state, and the other two dashed lines are the "virtual levels", and they represent the combined energy of one of the energy eigenstates of the atom and one or more photons of the radiation field [141].
Under the right experimental conditions, the second-harmonic generation process can be highly efficient. These conditions are called *phase matching conditions* and are satisfied when **the conservation laws** are met.

1. Conservation of energy ($\hbar\omega$):

$$\omega_1 + \omega_1 = \omega_{signal} = 2\omega_1 \tag{2.35}$$

2. Conservation of momentum:

$$\mathbf{k}_1 + \mathbf{k}_1 = \mathbf{k}_{signal} \tag{2.36}$$

If both conditions are met, the process is called **phase-matched**. Recall the relation $\omega = ck = \frac{c_0}{n}k$, we can rewrite (2.35) in terms of the magnitudes of the wave vectors:

$$2\frac{\omega_1}{c_0}n(\omega_1) = \frac{\omega_{signal}}{c_0}n(\omega_{signal}) \tag{2.37}$$

$$= \frac{2\omega_1}{c_0}n(\omega_{signal}) \tag{2.38}$$

This suggests that:

$$n(\omega_1) = n(\omega_{signal}) = n(2\omega_1) \tag{2.39}$$

As a result, phase-matching second harmonic generation requires $n(\omega_1) = n(2\omega_1)$. However, due to dispersion, this can only be fulfilled upon propagation by using the birefringence of the crystal.

2.4.2 Sum- and difference-frequency generation

We now assume that the optical field incident upon a second-order nonlinear optical crystal consists of two different frequency components, which we write as:

$$\widetilde{E}(t) = E_1 e^{-i\omega_1 t} + E_2 e^{-i\omega_2 t} + c.c. \tag{2.40}$$

From equation (2.17), we see that the second-order contribution to the nonlinear polarization takes the form:

$$\widetilde{P}^{(2)}(t) = \epsilon_0 \chi^{(2)} \widetilde{E}(t)^2, \tag{2.41}$$

which leads to:

$$\begin{aligned}\widetilde{P}^{(2)}(t) = \epsilon_0\chi^{(2)}[&E_1^2 e^{-2i\omega_1 t} + E_2^2 e^{-2i\omega_2 t} + 2E_1E_2e^{-i(\omega_1+\omega_2)t} \\ &+2E_1E_2^* e^{-i(\omega_1-\omega_2)t} + c.c.] + 2\epsilon_0\chi^{(2)}[E_1E_1^* + E_2E_2^*].\end{aligned} \tag{2.42}$$

Where the complex amplitudes of the various frequency components of the nonlinear polarization are given by

$$\begin{aligned} P(2\omega_1) &= \epsilon_0\chi^{(2)}E_1^2 \qquad (SHG), \\ P(2\omega_2) &= \epsilon_0\chi^{(2)}E_2^2 \qquad (SHG), \\ P(\omega_1+\omega_2) &= 2\epsilon_0\chi^{(2)}E_1E_2 \qquad (SFG), \\ P(\omega_1-\omega_2) &= 2\epsilon_0\chi^{(2)}E_1E_2^* \qquad (DFG), \\ P(0) &= 2\epsilon_0\chi^{(2)}[E_1E_1^* + E_2E_2^*] \qquad (OR). \end{aligned} \tag{2.43}$$

Each expression has been named by the physical process that it describes, such as second-harmonic generation (SHG), sum-frequency generation (SFG), difference-frequency generation (DFG), and optical rectification (OR). Equation (2.43) shows that four different nonzero frequency components are present in the nonlinear polarization. However, only one of these frequency components will be dominant at a sufficient intensity level in the radiation generated by the nonlinear process. This is because the nonlinear polarization can efficiently generate an output signal only if a specific phase-matching condition is satisfied, and usually, this condition cannot be satisfied for more than one frequency component. Experimentally, one often chooses which frequency component will be emitted by accurately selecting the polarization of the input radiation and the orientation of the nonlinear crystal. Phase matching is achieved when the conservation laws are fulfilled according to the following:

The conservation laws

1. Conservation of energy ($\hbar\omega$):

$$\omega_1 + \omega_2 + \cdots + \omega_n = \omega_{signal} \tag{2.44}$$

2. Conservation of momentum:

$$\mathbf{p} = \frac{E}{c}\mathbf{u} = \frac{\hbar\omega}{c}\mathbf{u} = \hbar\mathbf{k} \tag{2.45}$$

   where $\mathbf{u}$ is the propagation direction of the photon

$$\mathbf{k}_1 + \mathbf{k}_2 + \cdots + \mathbf{k}_n = \mathbf{k}_{signal} \tag{2.46}$$

If both conditions are met, the process is called **phase-matched**.

Sum-frequency generation

If we assume to have the process of sum-frequency generation, which is illustrated in (2.3), based on equation (2.43), the complex amplitude of the nonlinear polarization, which describes the process takes the form:

$$P(\omega_1 + \omega_2) = 2\epsilon_0\chi^{(2)}E_1E_2 \tag{2.47}$$

Sum-frequency generation is similar to second-harmonic generation, except that in sum-frequency generation the two input waves have different frequencies. Sum-frequency generation in our lab is commonly used in the electro-optic sampling setup, particularly in the one used to detect mid-infrared radiation. More details on that will be given in Chapter 5.

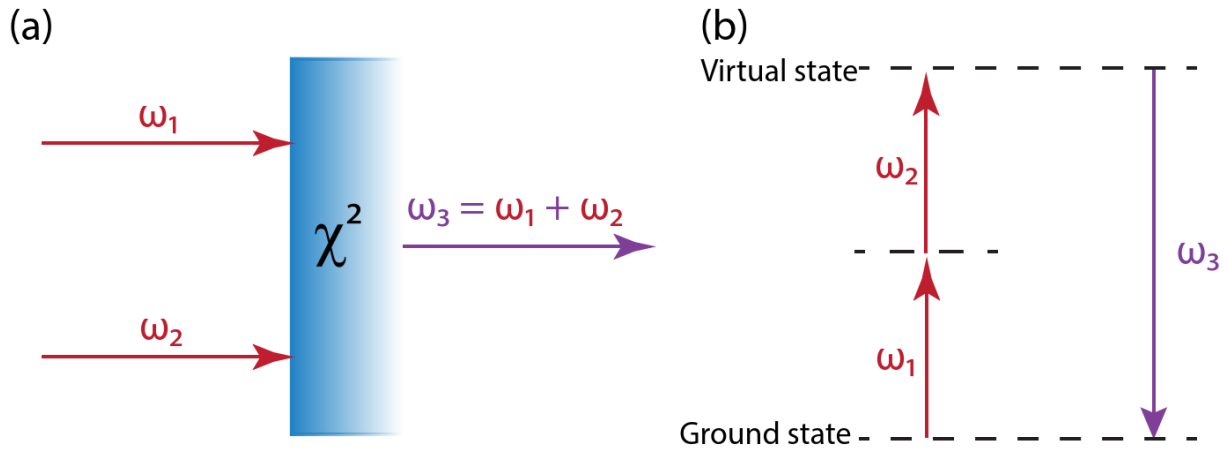

Figure 2.3: Sum-frequency generation. (a) The interaction geometry. (b) A diagram of energy levels that illustrates second-harmonic generation.

difference-frequency generation

The difference-frequency generation process is described by a nonlinear polarization as follows

$$P(\omega_1 - \omega_2) = 2\epsilon_0 \chi^{(2)} E_1 E_2^* \tag{2.48}$$

and is illustrated in Fig. (2.4). In this process, the frequency of the generated radiation is the difference between those of the input waves. Difference-frequency generation and, in particular, the intra-pulse one is commonly used to produce phase-stable infrared radiation by mixing the two sides of the spectrum of the input pulse. More details on this process will be given in Chapter 4.

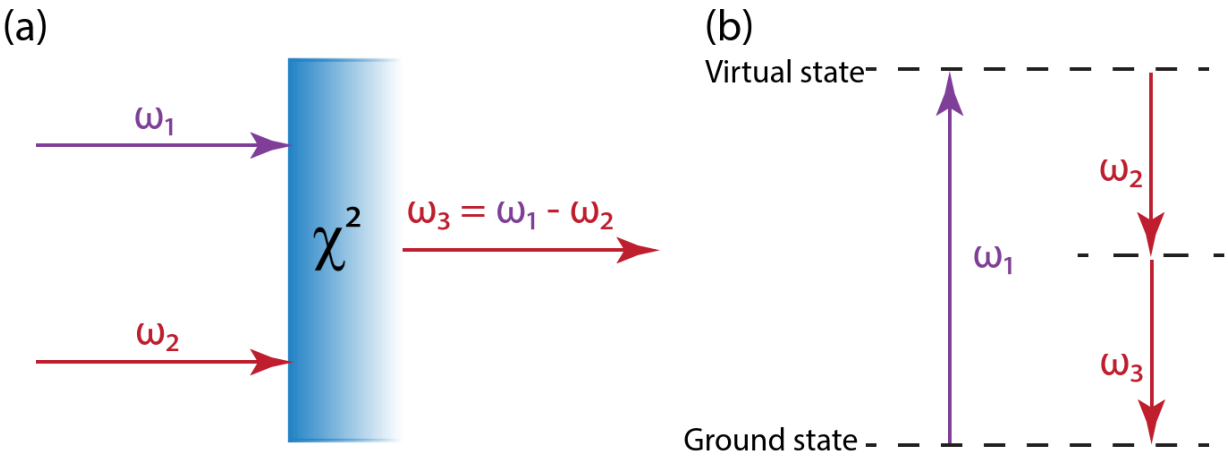

Figure 2.4: Difference-frequency generation. (a) The interaction geometry. (b) A diagram of energy levels that illustrates second-harmonic generation.

From the photon energy level diagram (part (b) of Fig. 2.4), one sees that the

conservation of energy requires that for every photon created at the difference frequency $\omega_3 = \omega_1 - \omega_2$, a photon at the higher input frequency ω_1 must be destroyed, and a photon at the lower input frequency ω_2 must be created. This implies that the lower-frequency input field is amplified by the process of difference-frequency generation. For this reason, the process of difference-frequency generation is sometimes also called **optical parametric amplification**. Based on the photon energy-level description the atom first absorbs a photon of frequency ω_1 and goes up to a higher virtual level. This level decays by a two-photon emission process, which is stimulated by the presence of the ω_2 field, which is already there.

2.4.3 Self-induced Nonlinear effects

When waves superimpose, in the absence of nonlinearities, one strong input wave is indistinguishable from two input waves each with half amplitude and identical phase. However, in the presence of a nonlinear response, a strong wave can affect its propagation. An example of this is *degenerte four-wave mixing*. To drive the latter process, the field needs to be intense. Moreover, no "parasitic" second harmonic generation or optical rectification should be present, because second-order processes convert power and generate new frequencies. The total polarization is:

$$P(t) = P_L(t) + P_{NL}(t) \tag{2.49}$$

By focusing on $\chi^{(3)}$ induced processes and assuming instantaneous response, the third-order nonlinear polarization is then given:

$$P_{NL}^{(3)}(t) = \epsilon_0 \chi^{(3)} \cdot E^3(t) \tag{2.50}$$

The real electric field $E(t)$ can be expressed as:

$$E(t) = \frac{1}{2}\left[\widetilde{E}(t) + \widetilde{E}^*(t)\right] \tag{2.51}$$

where

$$\widetilde{E}(t) = \widetilde{A}(t)e^{i\omega_c t} \tag{2.52}$$

$$\widetilde{A}(t) = a(t)e^{-i\varphi(t)} \tag{2.53}$$

and

$$\widetilde{E}^*(t) = \widetilde{A}^*(t)e^{-i\omega_c t} \tag{2.54}$$

$$\widetilde{A}^*(t) = a(t)e^{i\varphi(t)} \tag{2.55}$$

Here, $\widetilde{A}(t)$ is the slowly varying complex amplitude, and the term $e^{i\omega_c t}$ oscillates at frequency ω_c, and φ is the phase.
If we combine (2.52) and (2.53), we could write $\widetilde{E}(t)$ as:

$$\widetilde{E}(t) = a(t)e^{i[\omega_c t - \varphi(t)]} \tag{2.56}$$

With the above expressions, the third-order nonlinear polarization becomes:

$$\begin{aligned} P_{NL}^{(3)}(t) &= \epsilon_0 \chi^{(3)} \cdot E^3(t) \\ &= \epsilon_0 \chi^{(3)} \cdot \frac{1}{8}\left[\widetilde{E}(t) + \widetilde{E}^*(t)\right]^3 \\ &= \epsilon_0 \chi^{(3)} \cdot \frac{1}{8}\left[\widetilde{E}^3(t) + \widetilde{E}^{*2}(t) + 3\widetilde{E}(t)\widetilde{E}^{*2}(t) + 3\widetilde{E}^2(t)\widetilde{E}^*(t)\right] \end{aligned} \tag{2.57}$$

The terms $\left[\widetilde{E}^3(t) + \widetilde{E}^{*2}(t)\right]$ oscillate at $3\omega_c$ and $-3\omega_c$, this is called a third harmonic generation (THG).
On the other hand, the terms $\left[3\widetilde{E}(t)\widetilde{E}^{*2}(t) + 3\widetilde{E}^2(t)\widetilde{E}^*(t)\right]$ produce signals oscillating at combination of the frequencies $\omega_c + \omega_c - \omega_c$ or $\omega_c - \omega_c - \omega_c$, this is called *the optical Kerr effect*.

Kerr Effect

By rearranging the Kerr effect part of equation (2.57), we obtain:

$$\begin{aligned} \frac{8P_{Kerr}}{3\epsilon_0\chi^{(3)}} &= \widetilde{E}(t)\widetilde{E}^{*2}(t) + \widetilde{E}^2(t)\widetilde{E}^*(t) \\ &= \left|\widetilde{E}(t)\right|^2\left[\widetilde{E}^*(t) + \widetilde{E}(t)\right] \\ &= 2\left|\widetilde{E}(t)\right|^2 E(t) \end{aligned} \tag{2.58}$$

Where $E(t)$ in the final result is the *real* field.
From equations (2.52) and (2.53), we can see that:

$$\left|\widetilde{E}(t)\right|^2 = a^2(t) = I(t) \tag{2.59}$$

$I(t)$ is the temporal intensity evolution of the envelope function, or the *cycle-averaged* intensity. For the degenerate four-wave mixing, the conservation laws are fulfilled accordingly.
Energy conservation:

$$\omega + \omega - \omega = \omega \tag{2.60}$$

Momentum conservation:

$$\vec{k} + \vec{k} - \vec{k} = \vec{k} \tag{2.61}$$

this implies that the Kerr effect process is automatically phase-matched. In other words, a laser beam that is intense enough to considerably drive third-order nonlinearities will always experience the Kerr effect because it will be automatically phasematched. It is worth mentioning that the Kerr effect does not produce harmonics but modifies the phase of the light; thus, it modifies the propagation velocity of the light inside the material.

Therefore, the light modulates the phase velocity property of the material, namely the refractive index property of the material. The total nonlinear polarization becomes:

$$\begin{aligned} P_{NL}(t) &= \epsilon_0 \chi^{(3)} E^3(t) \\ &= \epsilon_0 \chi^{(3)} E^2(t) \cdot E(t) \\ &= \epsilon_0 \chi^{(3)} |E(t)|^2 \cdot E(t) \end{aligned} \tag{2.62}$$

Whereas the nonlinear polarization due to the Kerr effect only is:

$$P_{Kerr}(t) = \frac{3}{4} \epsilon_0 \chi^{(3)} |\widetilde{E}(t)|^2 \cdot E(t) \tag{2.63}$$

We can immediately see that $|E(t)|^2$ is the instantaneous intensity, and $|\widetilde{E}(t)|^2$ is the cycle-averaged intensity, $I(t)$.

Consequences of the Kerr Effect (in Time)

In time, a pulse of light will see a time-dependent refractive index $n(t)$, where $n(t)$ determines the phase velocity of light inside the medium [23].

$$n(t) = n_0 + n_2 I(t) \tag{2.64}$$

From the previous equation, it can be seen that the physical implication of the nonlinear refractive index n_2 is that it is the rate at which the refractive index increases with increasing optical intensity. Let's consider two cycles of the field before and after the strongest cycle, with the propagation direction pointing to the left as illustrated in Fig. 2.5 and Fig. 2.6:

1. Rising edge:

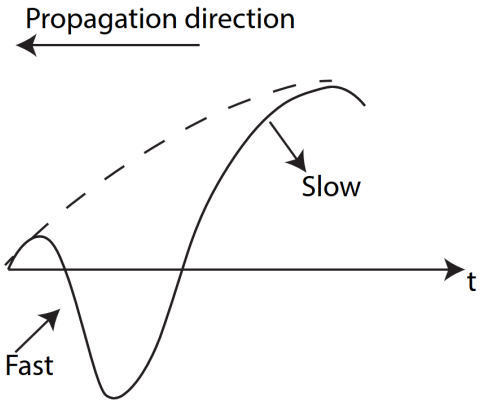

Figure 2.5: Red shift. Dashed line is the intensity envelope and the solid one is the oscillating field.

In this case, we see that as the intensity I increases, the refractive index n increases with time, and light propagates slower. As a result, the cycle is stretched in time so that the wavelength becomes longer; this is called the red shift.

2. Falling edge:

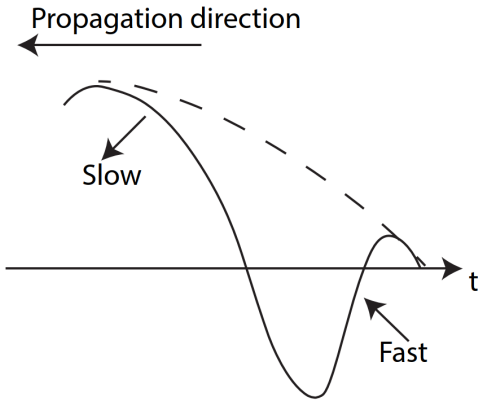

Figure 2.6: Blue shift. Dashed line is the intensity envelope and the solid one is the oscillating field.

In this case, we see that as the intensity I decreases, the refractive index n decreases with time, and light propagates faster. As a result, the cycle is compressed in time such that the wavelength becomes smaller; this is called the blue shift.

In both cases, the intensity envelope remains the same, but the phase of the oscillation is modulated beneath the intensity envelope; this is called *self-phase modulation* (SPM) and will be discussed next.

Self-phase modulation

In a thin medium with a thickness of l, when ignoring dispersion and transverse effects, a pulse will experience a phase shift of:

$$\Delta\phi(t) = 2\pi\frac{n(t)\cdot l}{\lambda} = 2\pi\frac{[n_0 + n_2 I(t)]\cdot l}{\lambda} \tag{2.65}$$

This imprints a time-dependent nonlinear phase of:

$$\Delta\phi_{NL}(t) = \frac{2\pi n_2 I(t)\cdot l}{\lambda} \tag{2.66}$$

If we have an electric field given by:

$$\begin{aligned} E(t) &= a(t)e^{i[\omega_c t - \varphi(t)]} + c.c. \\ &= a(t)e^{i\phi(t)} + c.c. \end{aligned} \tag{2.67}$$

where we have defined:

$$\phi(t) = \omega_c t - \varphi(t) \tag{2.68}$$

and the instantaneous frequency is defined by:

$$\omega_{inst} = \frac{\partial}{\partial t}\phi(t) \tag{2.69}$$

substituting (2.68) in (2.69) gives:

$$\omega_{inst} = \frac{\partial}{\partial t}\phi(t) = \omega_c - \frac{\partial\varphi(t)}{\partial t} \tag{2.70}$$

Hence, the time-dependent nonlinear phase will result in a shift of the instantaneous frequency of:

$$\Delta\omega = -\frac{\partial}{\partial t}\Delta\varphi_{NL}(t) \tag{2.71}$$

If there is no phase modulation (no $\varphi(t)$), then we have one frequency that is modulated by the envelope function $a(t)$ (green line in Fig. 2.7). Thus, at all times, the instantaneous frequency is fixed ω_c. However, when the Kerr effect is present, at the trailing edge of the pulse, causes a longer wavelength, and then the wavelength becomes shorter as it propagates (lime line in Fig. 2.7). In this case, the instantaneous frequency ω_{inst} defines at which frequency the light oscillates.

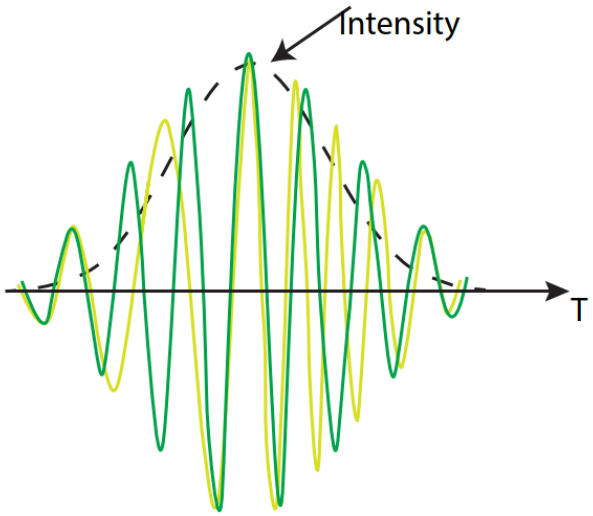

Figure 2.7: Influence of self-phase modulation on an unchirped pulse. The figure shows the electric field oscillations of the original pulse before and after it undergoes SPM. Due to the SPM, the pulse becomes strongly up-chirped where the instantaneous frequency grows with time.

A plot of the shift of the instantaneous frequency $\Delta\omega$ versus time t, of an initially unchirped pulse that has experienced self-phase modulation, shown in 2.8:

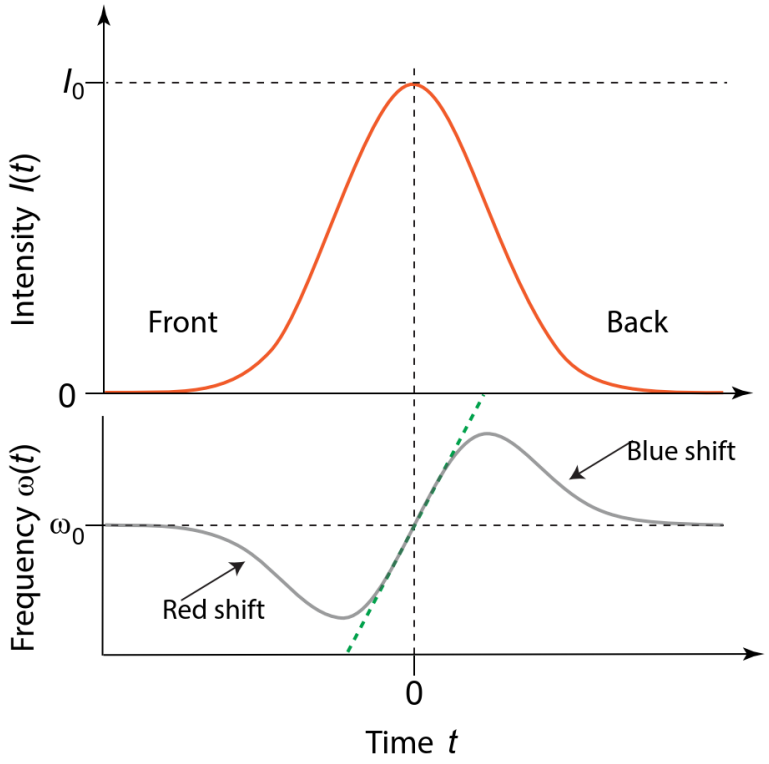

Figure 2.8: Temporally varying instantaneous frequency due to SPM.

The time-dependent phase shift induced by SPM results in changes in the optical spectrum. In the case of an unchirped or up-chirped pulse, the SPM causes the spectrum to broaden, increasing its optical bandwidth. Compensation of the spectral phase leads to temporal compression of the light pulse, ideally to its Fourier-transform limit. Furthermore, if we consider the spectrum of the pulse, as illustrated in Fig. 2.9, we observe new secondary maxima (peaks) indicating new frequency components, while the dips indicate the interference of blue and red ones, which is the main characteristic of SPM.

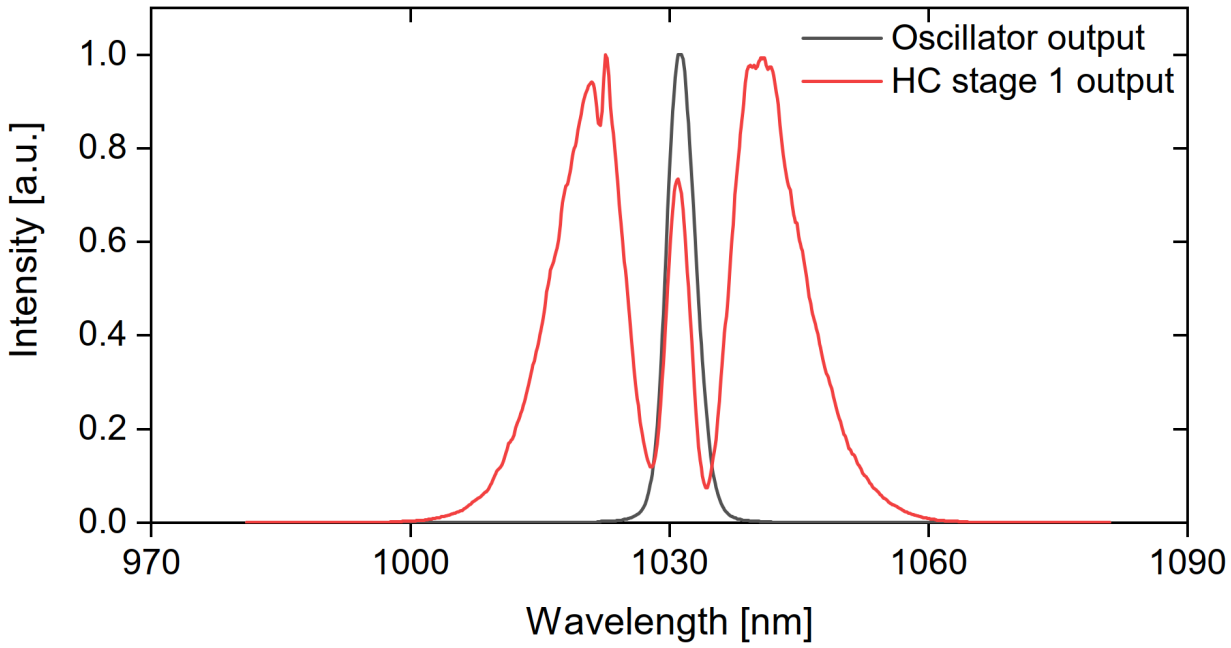

Figure 2.9: SPM based spectral broadening. Power spectral density of the oscillator output (black line) along with the power spectral density of the output of the Herriot cell spectral broadening stage utilizing SPM (red line).

SPM can also be induced by other effects, not only by the Kerr effect. For example, when an intense beam passes through a gas and starts to ionize the atoms/molecules, free electrons are generated, which also modulate the refractive index. However, this is not an instantaneous effect as all of the electrons generated stay in the continuum on the time scale of the pulse. The steady refractive index decreases with an increasing number of electrons, which induces a blue shift. In contrast, in Kerr-effect-driven SPM, we observe both a blueshift and a redshift.

Chapter 3

Few cycle NIR laser pulses

3.1 Introduction

Ultrafast, intense light pulses are used in various fields, from fundamental science to spectroscopy and medical applications [92]. However, many ultrafast optics applications and processes require further advances in laser technologies to fully exploit the potential of their underlying physical mechanisms. One of the main challenges is improving the peak power and average power of the utilized femtosecond sources simultaneously [42, 28]. Increasing the peak power is crucial for achieving intense light pulses that can interact with matter in a highly nonlinear regime, enabling nonlinear spectroscopy and high-field physics experiments. On the other hand, enhancing the average power is important for applications that require a high repetition rate and sustained power delivery, such as laser-based machining or material processing.

However, to this date, NIR laser oscillators that deliver both the high peak- and average power required for the above-mentioned ultrafast applications are not readily available. Overcoming these challenges often involves advancements in laser technologies, including novel laser cavity designs, the development of new gain materials, pulse compression techniques, and more efficient cooling mechanisms. A common solution to boost the peak power is post-oscillator temporal compression of the laser pulses via spectral broadening and dispersion management [25], while the average power is conventionally boosted in single- or multi-stage power amplifiers.

While extremely broadband titanium-sapphire (Ti:Sa) lasers have been the main option for generating tens of femtoseconds long pulses for high-intensity applications in the past three decades [21, 81], more recent laser systems like ytterbium ion-doped lasers (Yb:YAG), which have less emission bandwidth but better average power scalability [42, 68, 117], have replaced the (Ti:Sa) lasers.

Despite the advancements made, achieving pulse durations below the Fourier limit of the gain bandwidth, which is supported by the output spectra of high-power lasers, remains a significant challenge. This is especially true for lasers that encompass a wide range of pulse durations, ranging from a few hundred femtoseconds to several picoseconds, such as

cryogenically cooled lasers[112]. Nevertheless, these lasers require extra-cavity pulse compression to generate pulses with durations down to tens of femtoseconds due to the limited gain bandwidth of the active medium.
Two main approaches exist for reaching few-cycle pulses: amplifying a supercontinuum by pumping it with narrowband but powerful laser pulses (known as optical parametric chirped-pulse amplification) or direct broadening of the spectral width of high-average-power pulses employing the optical Kerr effect in nonlinear media, such as noble gases or fused silica. Although the first approach produces few-cycle pulses with excellent compressibility, that is, excellent temporal contrast [38], the second one can achieve a much higher power efficiency of over 90%, which makes it a highly attractive approach for power-scaling applications due to minimal power losses [53, 121, 144].
The goal of this work was to develop a mid-infrared radiation source that covers the entire molecular fingerprint region while also possessing the desired properties for coherent spectroscopy, which include broad bandwidth, high temporal and spatial coherence, high repetition rate, and high average power. Due to the lack of suitable gain media, no laser-based source can directly provide such radiation with the previously mentioned specifications. Therefore, most coherent broadband mid-IR sources rely on the parametric down-conversion of ultrashort laser pulses produced by established visible/near-IR laser technologies [15, 48, 119].
Parametric downconversion driven by modern high-power sources of 10-fs-scale near-infrared pulses, in particular intrapulse difference-frequency generation (IPDFG), affords combinations of desirable properties for molecular vibrational spectroscopy in the mid-infrared range [12, 20, 26, 27, 41, 44, 48, 59, 110, 116, 128, 131, 138, 150]. However, the significant trade-off between bandwidth and efficiency during the nonlinear conversion process has been the primary limitation of IPDFG-based MIR sources thus far [26]. This is, in particular, true for the IPDFG driven by NIR laser sources at around 1 µm.
To overcome those limitations, the driving laser source needs to (i) have a high field strength, thus high peak power, to be able to observe a second-order nonlinear effect, and (ii) the generation of short-wavelength mid-infrared (MIR) by the IPDFG process requires ultrashort NIR laser pulses because the upper-frequency cut-off of the IPDFG process scales linearly with the bandwidth of the incident NIR pulse spectrum.
Figure(3.1) shows the concept of intrapulse difference-frequency generation, in which a MIR idler signal is generated by phase-matched mixing of spectral components (signal, from the lower frequency side of the spectrum and pump, from the higher frequency side) within a broadband driving pulse [26]. The mixing process occurs in a suitable medium that fulfills the phase-matching condition, i.e., a nonlinear crystal.
This chapter focuses on the frontend, represented by a Kerr-lens mode-locked femtosecond oscillator, in which the (Yb)-doped gain material is in a thin-disk geometry [107], and which is complemented with extra-cavity pulse compression based on nonlinear spectral broadening and temporal recompression. The latter includes a dual-stage all-bulk Heriot-cell type spectral broadening followed by a distributed quasi-waveguide [55] which compresses the output pulses of the preceding thin-disk oscillator [107], by nearly 26 times.

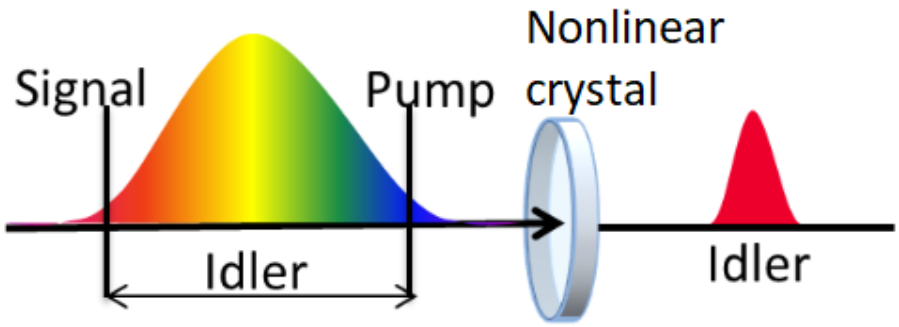

Figure 3.1: Concept of intrapulse difference-frequency generation (see text).

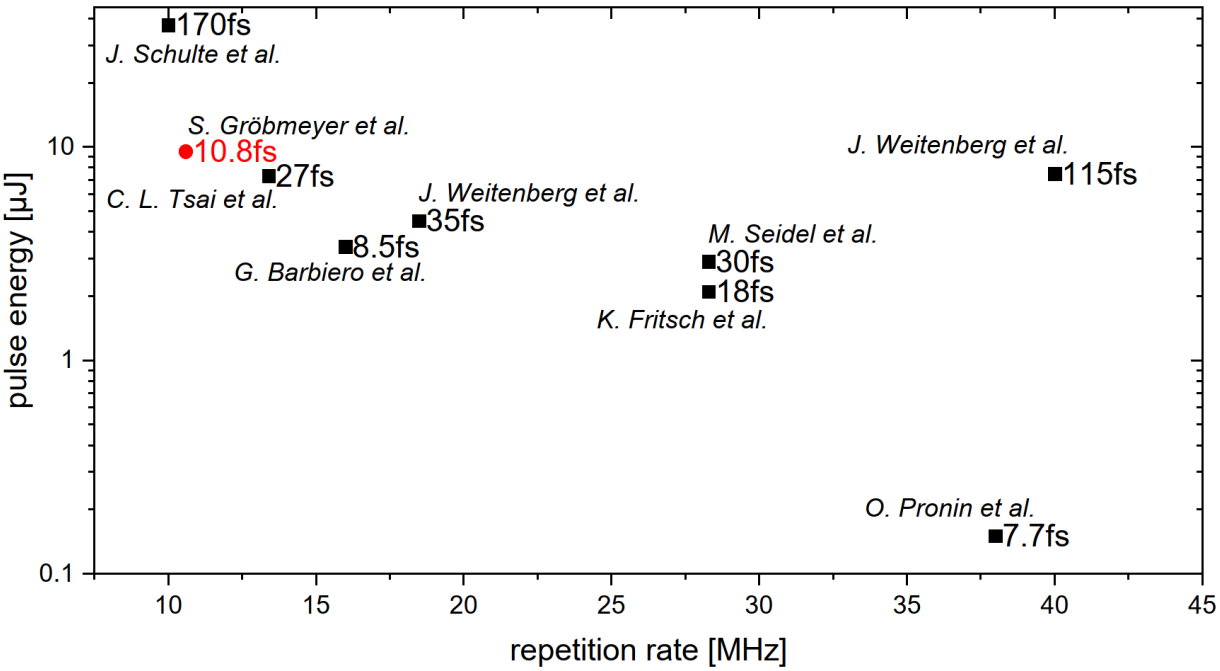

Figure 3.2: Overview of 1 µm femtosecond laser systems with external nonlinear pulse compression in bulk.

Figure (3.2) provides an overview of 1 µm femtosecond laser systems that utilize external nonlinear pulse compression in bulk. The graph displays the results of various 1 µm femtosecond laser systems, including the data from S. Gröbmeyer et al. highlighted in red. The figure compares the pulse duration, pulse energies, and repetition rates of these different laser systems. Additionally, table (3.1) presents the compression factor, references, and conversion efficiencies (output power/input power) for each system.

Author	Factor	Efficiency	Reference
O. Pronin et al.	>32	42.5%	[108]
J. Schulte et al.	5	>90%	[121]
K. Fritsch et al.	∼14	>60%	[46]
C. L. Tsai et al.	∼20	80%	[133]
G. Barbiero et al.	25	65%	[12]
J. Weitenberg et al.	∼7.5	>90%	[144]
M. Seidel et al.	∼6.3	75%	[123]
J. Weitenberg et al.	∼6.6	88%	[143]
S. Gröbmeyer et al.	∼26	>83%	in preparation

Table 3.1: Overview of 1 µm femtosecond laser systems with external nonlinear pulse compression in bulk. Comparison between compression factor and power transmission efficiency.

3.2 Kerr-lens mode-lock thin-disk oscillator

The initial pulse train in our setup is produced by a Kerr-lens mode-locked Yb:YAG thin-disk oscillator with a repetition frequency of 10.6 MHz, previously described in [107]. At an average output power of 140 W, this frontend operates in air and delivers pulses with a duration of 288 fs, spectrally centered at 1030 nm. The oscillator employs an active multipass cell approach [97], allowing up to four reflections on the thin disk (16 passes through the gain medium per round trip), as illustrated in Fig. (3.3).

The number of additional passes could be adjusted between zero and three via the horizontal displacement of mirror X. This feature is advantageous, allowing for systematic variation of the number of passes through the disk without affecting the main cavity mode. The output pulses exhibit an energy of 13.2 µJ and a pulse duration of 288 fs, resulting in a peak power of 40 MW. The 140 W of average power is produced with an optical-to-optical efficiency of 27%. Fig. (3.4) adapted from [107], depicts the measured spectrum and the intensity autocorrelation of the output pulses.

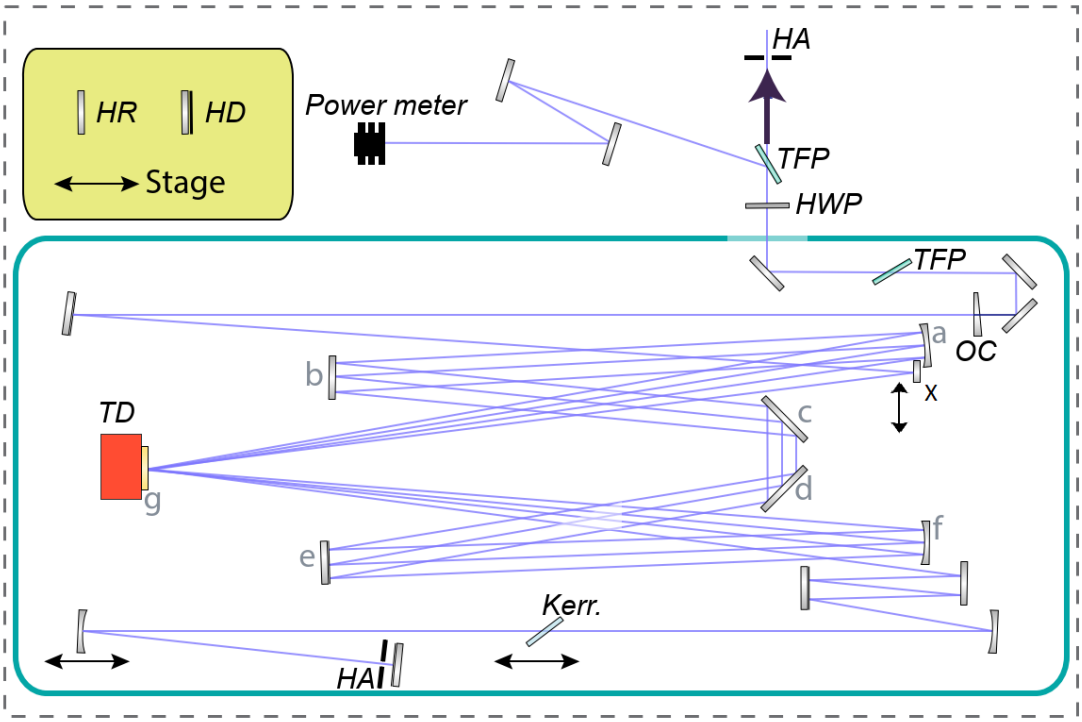

Figure 3.3: Schematic of the KLM thin-disk oscillator with an active multipass cell (AMC). The AMC is formed by: the distance g-a, concave mirror F_{IM} at a distance a-b-c-d-e-f, concave mirror F_{IM} at f, distance f-g, and one reflection on the thin disk. Horizontal displacement of the pick-off mirror X adjusts the number of passes through the AMC. OC, output coupler; HD, high-dispersion mirror; TD, thin disk; F, a concave mirror of the Kerr telescope; H, hard aperture; K, Kerr medium. Nonlabeled components are highly reflective mirrors.

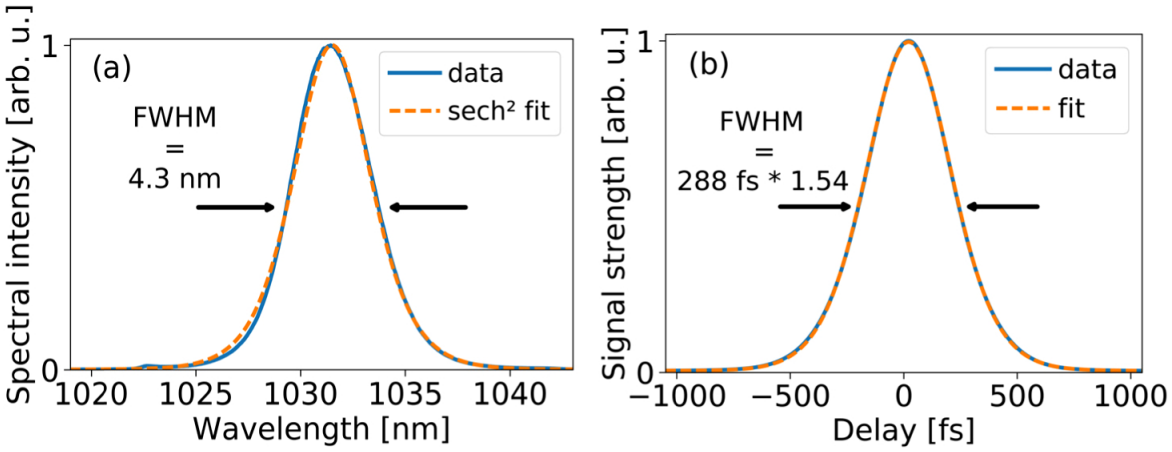

Figure 3.4: Spectral and temporal characterization of oscillator output (a) Emitted spectrum fitted with a $sech^2$ function. (b) Intensity autocorrelation of the output pulse and a corresponding model is fitted. Figure adapted from [107].

3.3 Dual-Herriott-cell spectral broadening stage

The narrow gain bandwidth of the Yb-based oscillator limits the spectrum of the output pulses to only a few nanometers. However, to enhance the peak power of the emitted pulses to a level that meets the IPDFG requirements, we employed extra-cavity pulse compression based on multiple passes through thin Kerr media [10, 96, 121, 133, 143]. Owing to the high required compression factor and the stringent requirements of a clean temporal pulse shape, a dual-stage multipass-cell spectral broadening approach has been chosen over spectral broadening in a single Herriott-cell to achieve the desired high-power few-cycle pulses presented here [55], which are required to drive the frequency down-conversion process. Specifically, 120 W from the oscillator output was sent to a dual-stage Herriott-cell-type spectral broadening along with intermediate temporal re-compression [12, 46, 86, 133, 139]. The pulse durations after the two compression stages were 68 fs and 16 fs, respectively.

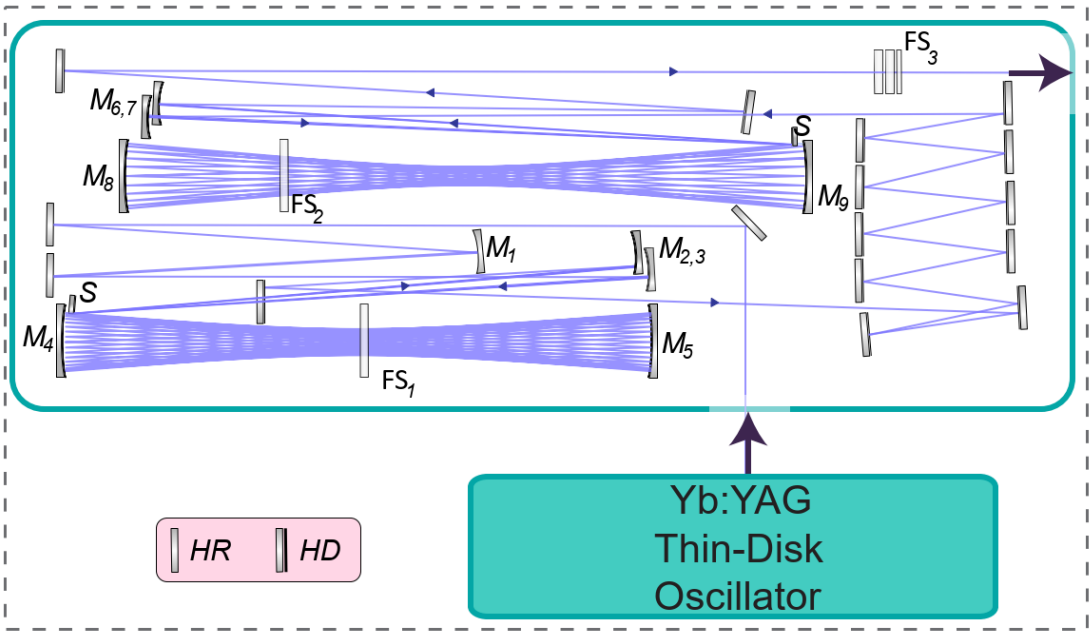

Figure 3.5: Dual-stage multipass-cell spectral broadening setup. M_1, collimating mirror with a radius of curvature of 6000 mm, $M_{2,3}$: first-stage focusing-and collimation mirrors with a radius of curvature of 1500 mm, S: scraper mirror, M_4 and M_5: first-stage multi-pass-cell mirrors, FS_1: fused silica plate of 6.35 mm thick, $M_{6,7}$: second-stage focusing-and collimation mirrors with a radius of curvature of 1500 mm, M_8 and M_9: second-stage multi-pass-cell mirrors, FS_2: fused silica plate of 6.42 mm thick, FS_3: adjustable amount of additional fused silica plates for fine dispersion control, HR and HD: high reflectance and high dispersive mirrors, respectively.

The dual-stage Herriott-type multipass-cells setup operating in the net-positive dispersion regime has been developed by Gröbmeyer et al. and is shown in Fig. 3.5. The

setup is compact despite using tens of passes since the beam is repeatedly focused with the same set of mirrors through a single nonlinear medium. The first multipass-cell (MPC) consists of a pair of concave mirrors separated by a distance of 480 mm, each with a radius of curvature of 300 mm. As a result, the beam travels through the 6.35-mm thick fused silica nonlinear medium 34 times before it is coupled out of the multipass cell with the help of a small scraper mirror.
To achieve a nonlinear phase shift of 0.2 rad in the first pass, the position of the nonlinear medium was chosen to be at a distance of 174 mm from one of the mirrors of the multipass cell, namely 24 mm away from the focus, which is located in the central symmetry plane of the MPC. After collimating the oscillator output using a spherical mirror (M1) with 6000 mm ROC and a high reflecting coating centered around 1030 nm, provided by LAYERTEC, the beam has been focused by mirror M2 with a 1500 mm ROC to match the eigenmode of the Herriott cell; see Fig. 3.5. Due to the large angular advance of the Herriott cell, a vertically offset concave mirror with the same ROC has been used to collimate the output of the multipass cell.
Afterward, the spectrally broadened pulses have been compressed utilizing a chirped mirror compressor with a total group delay dispersion (GDD) of -4000 fs^2 added through 15 reflections of in-house-made dispersive mirrors with design number PC162. The plano-concave mirrors forming the first multipass cell feature a dispersive coating custom-made in our group by Pervak et al. with the design number PC1611 which reflects the wavelengths between 940 nm and 1100 nm. An anti-reflection (AR) coating has been applied to all fused silica plates, which were used as a nonlinear broadening medium. As mentioned above, both broadening stages were fully developed and built during the doctorate work of Sebastian Gröbmeyer; however, due to multiple damage to optical elements, mirrors, and fused silica broadening media in the first and second stages, the system had to undergo some maintenance and thus replaced damaged optics with new ones.
Due to slight deviation and inaccuracy of both the new coating versions (compared to the original coating) and the thickness of the fused silica plates (nonlinear media), the setup required additional modifications to maintain its original pulse compression quality. Namely, since the broadening medium which was used by Gröbmeyer et al. in the first MPC has a standard thickness of 1/3" (6.35 mm), a minimal change in the distance between MPC pairs of mirrors was needed to compensate for the slight change in the total optical path length. Moreover, since the pulse peak power is not that critical in the first broadening stage, the influence of the deviation in the newly coated optics compared with the one previously used by Gröbmeyer et al. was negligible.
Figure 3.6 provides a detailed characterization of the output of the first Herriott-cell, utilizing SHG-FROG. Part (a) shows the retrieved power spectral density and spectral phase obtained through FROG analysis. An optical spectrum analyzer (OSA) was used to measure the power spectral density. Part (b) displays the temporal phase and intensity envelope of the retrieved pulse, along with its calculated Fourier-transform limit. (c) Shows the measured SHG-FROG trace. Part (d) presents the reconstructed FROG trace. The compressed pulses exhibit a pulse duration of 69 fs at full width at half maximum

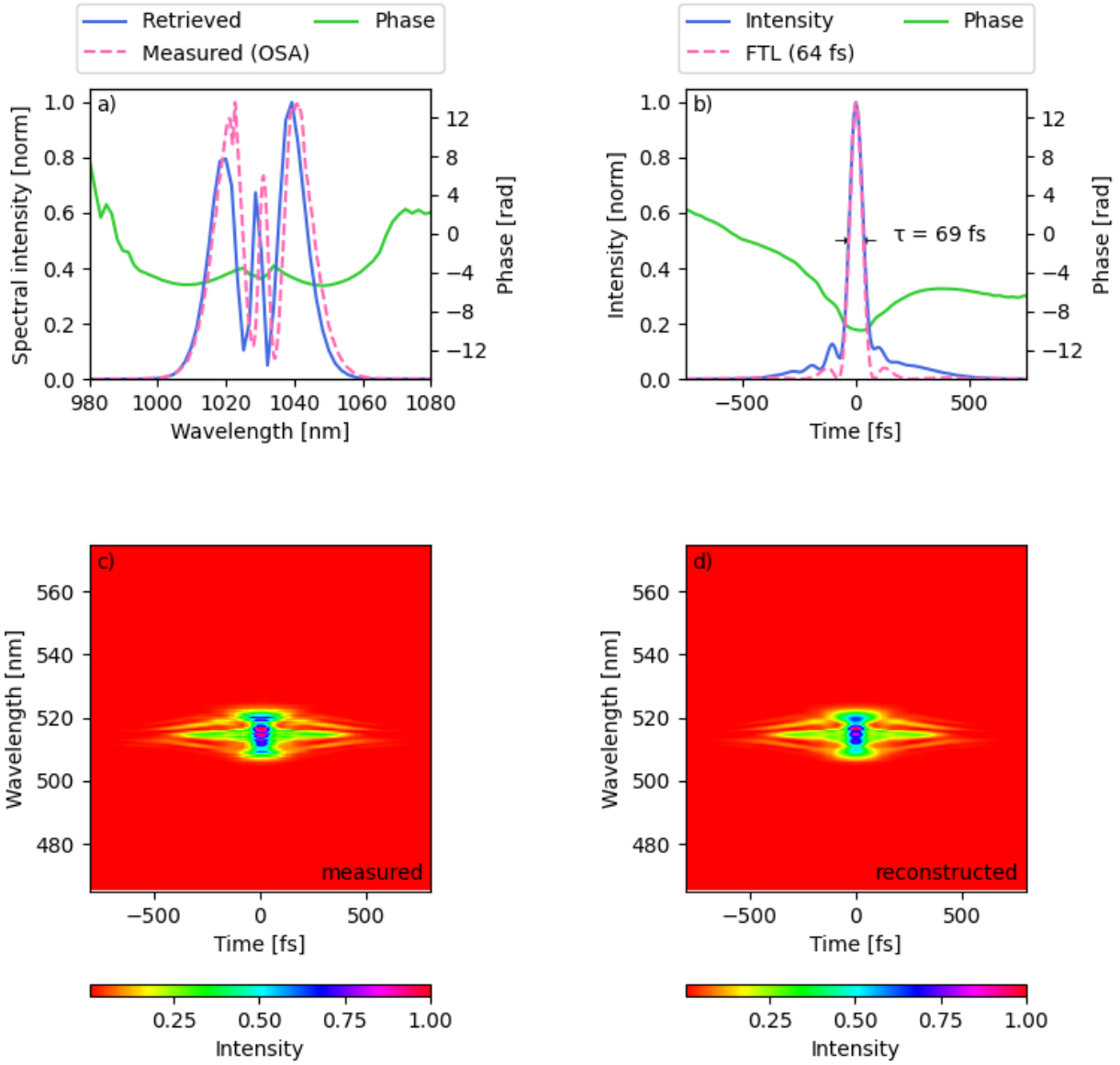

Figure 3.6: Herriott-cell stage-one output characterization. (a) Measured and recovered power spectral density and spectral phase. (b)The retrieved pulse's temporal phase and intensity envelope, together with its Fourier limit. (c) Measured SHG-FROG trace. (d) Reconstructed FROG trace.

(FWHM), resulting in a peak power of 121 MW. This represents a compression factor of 4.17 and an increase in peak power by a factor of 3.

Similar to the first MPC, the second MPC employs two concave mirrors, but with a different Herriott-cell configuration. Because the input pulse duration in the second broadening stage is significantly shorter than in the first stage, the impact of accumulated dispersion on the propagated pulses is amplified, resulting in higher temporal broadening,

which is expected to reduce the spectral broadening rate. To avoid this, the number of passes through the nonlinear medium was reduced to 22 with a per-pass nonlinear phase shift of 0.35 rad. The aforementioned parameters were achieved by increasing the mirror separation to 553 mm, for a pair of mirrors with a radius of curvature of 300 mm, and by placing the nonlinear medium further from the focus by a few millimeters.
By using a concave mirror with a 1500-mm radius of curvature placed at a distance of approximately 750 mm to the center plane of the second Herriott cell, the collimated output of the chirped-mirror compressor from the previous compression stage is matched to the eigenmode of the multipass cell.
Multiple fused silica plates with slightly different thicknesses were tested as nonlinear media by S. Gröbmeyer et al. [55], to decrease the effect of dispersion on pulse propagation. It was found that a 6.23-mm-thick (with coating) fused silica plate was the most effective in maximizing spectral broadening while maintaining a net-positive dispersion regime. Moreover, to compensate for the reduced number of passes compared to the first broadening stage, the initial nonlinear phase shift needed to be increased significantly to achieve a similar total accumulated phase $\Sigma\phi_{NL}$. As a result, the fused silica plate was placed 137 mm from one of the multipass-cell mirrors, and the initial nonlinear phase shift was adjusted to $\phi^i_{NL} = 0.35$ rad. This provided a balance between high nonlinearity and only slightly degraded beam quality [55].
Unfortunately, the fused silica medium with the thickness mentioned previously for which the system has been optimized was damaged and had to be replaced. Replacement with the very same thickness was not possible since the thickness was not standardized. The closest available thickness was 6.42 mm (with coating). The position of the nonlinear medium had to be adjusted from 140 mm to 126 mm to one of the Herriott-cell mirrors in order to maintain the original nonlinear phase shift while providing a balance between high nonlinearity (broadening) and slightly degraded beam quality. However, reaching the same spectral shape of output as before was not feasible.
Fig. (3.7) shows the impact of the broadening medium thickness on the total nonlinear phase shift. It shows the accumulated nonlinear phase shift as a function of the number of passes through the broadening medium. The upper and lower panels depict a previously optimized system's accumulated nonlinear phase shift in blue and two new cases in orange. In the upper panel, the 6.42-mm-thick fused silica medium (the new one) is placed in the same position as the 6.23-mm-thick plate (previously used one), resulting in a lower total nonlinear phase $\Sigma\phi_{NL}$ despite starting with a higher value at the first pass ϕ^i_{NL}= 0.4 rad. Moreover, this position caused beam profile degradation and was therefore not chosen as the final configuration. In the lower panel, the peak intensity was reduced to achieve the same initial nonlinear phase shift as the thinner medium case, ϕ^i_{NL}= 0.35 rad, resulting in equivalent beam quality but with a slightly reduced total phase shift $\Sigma\phi_{NL}$ of 8 rad compared to approximately 9 rad in the thinner medium case, which in turn resulted in a negligibly narrower spectrum.
GDD variations of the optical coating: The mirrors used for the second multipass-cell (design number PC1711) are distinct from those employed for the first and are equipped with a dispersive coating, designed to attain a target mean GDD and TOD

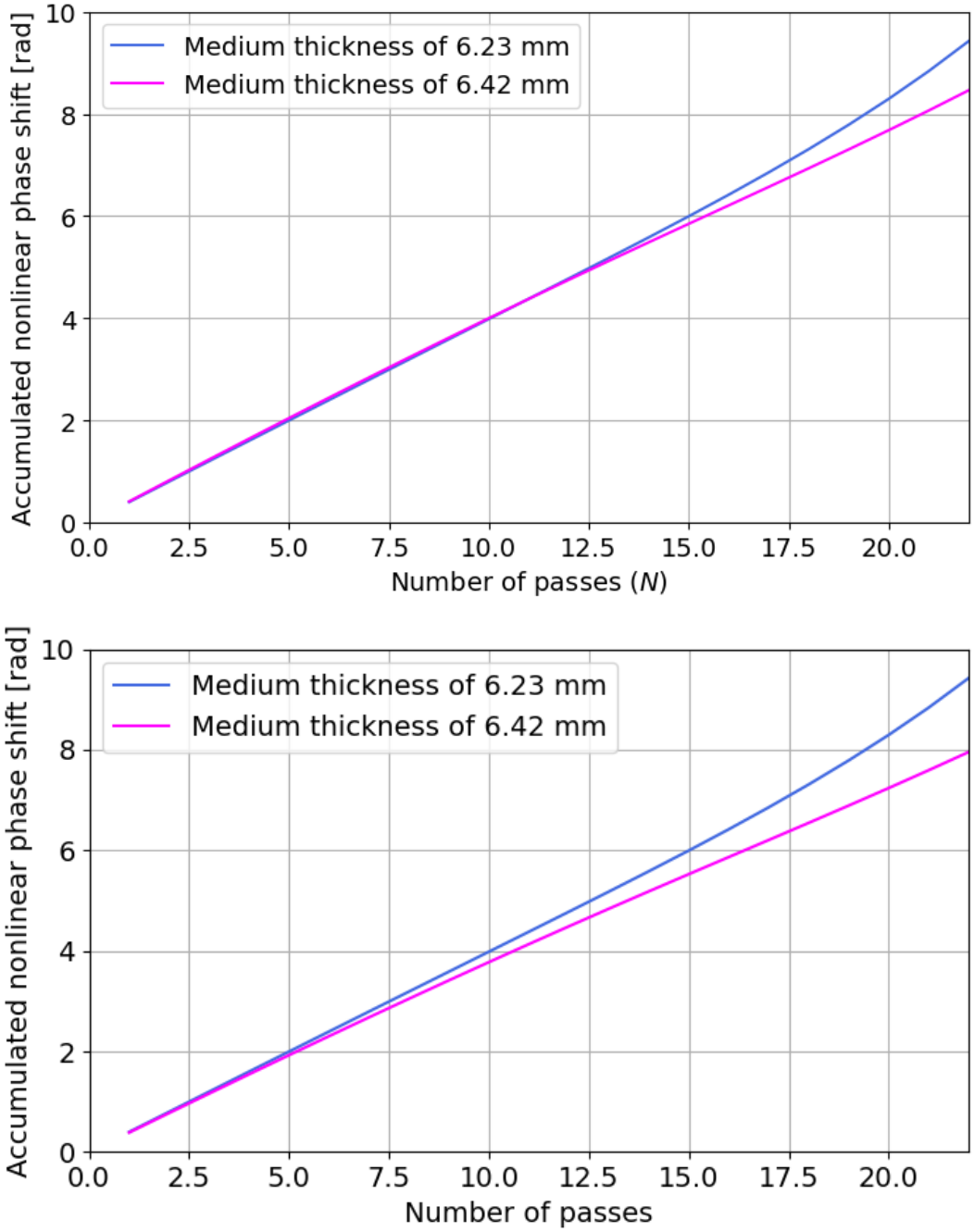

Figure 3.7: The figure illustrates the accumulated nonlinear phase shift as a function of the number of passes through a broadening medium, comparing two thicknesses of fused silica plates, previously used one of 4.23 mm (blue line) and currently available of 4.42 mm (magenta line). The upper panel shows that starting with a higher value of the nonlinear phase shift ($\phi^i_{NL} = 0.4$ rad), when placing the thicker plate in the same position, 137 mm from one of the HC mirrors, as the thinner one results in a lower total accumulated phase shift. However, it caused a degradation in beam quality. The lower panel shows that reducing the peak intensity to achieve an equivalent initial nonlinear phase shift, when the thicker plate is used, as with the thinner medium, results in a slightly reduced total nonlinear phase shift $\Sigma\phi_{NL}$ of 8 rad compared to 9 rad, respectively. In the experiment, this configuration was found to maintain equivalent beam quality compared to the original case, but with a negligibly narrower spectrum after spectral broadening.

of -119 fs^2 and -240 fs^2, respectively, at a central wavelength of 1030 nm. Given the high demands on the mirror bandwidth, which ranges from 850 nm to 1200 nm, the coating is implemented as a complementary dispersive pair, which helps minimize residual GDD oscillations. However, the experimental dispersion measurements differ from those of the theoretically aimed target.
Fig. 3.8 provides insight into the effect of deviations in the GDD curves among different coating runs on the output spectrum of the SPM-driven nonlinear broadening. Part (a) of the figure shows the measured GDD curves for three different coating runs of the PC1711 design (versions 3, 4, and 5). This provides information on the variation of GDD in various coating runs. Part (b) of the figure shows the output spectrum before and after replacing the HC mirrors PC1711 with newly coated mirrors of the same design. The three curves represent the net GDD values of the complementary pair of mirrors for each coating version. From the upper panel in Fig. 3.8 we see a drastic amplitude mismatch, particularly around 1020 nm and 1050 nm, between the last two coating versions (versions 4 and 5) that were used in the system previously and the fifth version that has been done lately.
However, after the newly coated mirrors were used, a drastic change in the output spectrum of the second-stage Herriot cell was noticed. The latter change is illustrated in the lower panel of Fig. 3.8. An extremely unforgiving variance, we see, specifically around the wavelength range of 1020 nm and 1050 nm, which we have attributed to the aforementioned difference between the coating of the new mirrors compared to the previously used ones.
Fig. 3.9 provides a detailed characterization of the output of stage two Herriott cell, utilizing SHG-FROG. Part (a) shows the retrieved power spectral density and spectral phase obtained through FROG analysis. An optical spectrum analyzer (OSA) was used to measure the power spectral density. Part (b) displays the temporal phase and intensity envelope of the retrieved pulse, along with its calculated Fourier-transform limit. (c) Shows the measured SHG-FROG trace. Part (d) presents the reconstructed FROG trace. The compressed pulses exhibit a pulse duration of 16 fs at full width at half maximum (FWHM) and a peak power of 445.6 MW. This represents a compression factor of 4.3 and an increase in peak power of a factor of 3.7 in the first stage.
Measurement of beam quality performed at the output of the second Herriott-cell broadening stage is shown in Fig. 3.10. The retrieved M^2 values are 1.13 and 1.06 in the tangential and sagittal planes, respectively.
Figure 3.17 depicts the beam profile after the second stage.

3.4 Distributed quasi waveguide

To achieve pulse durations even closer to the few-cycle regime, the dual-stage MPC setup was followed by spectral broadening in a distributed quasi-waveguide (DQWG) which circumvents the limited flexibility of fine-tuning the per-pass dispersion and nonlinearity within MPCs and the accompanying spectral saturation. The last stage consisted of four

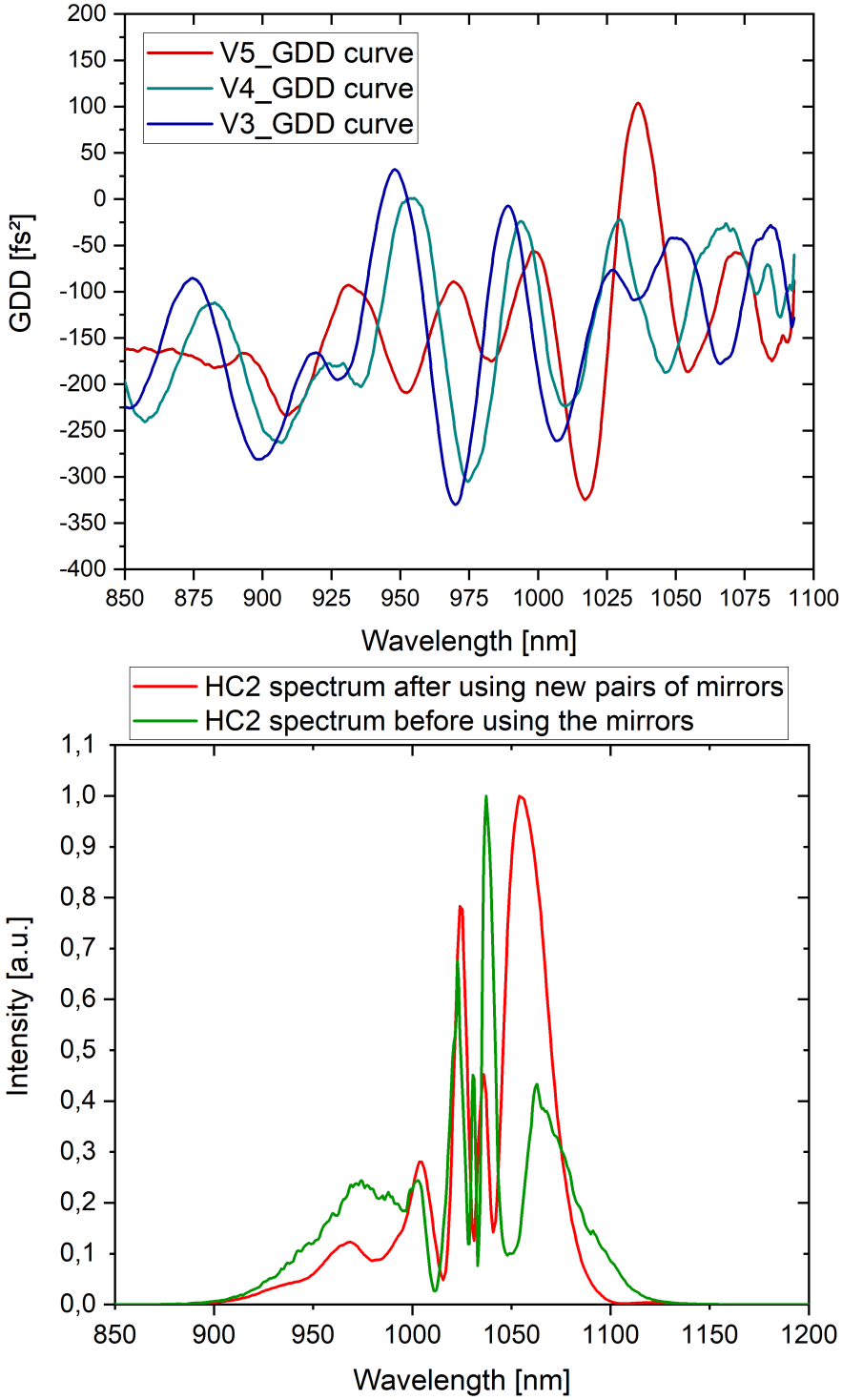

Figure 3.8: Influence of the variations within the dispersive coating on the output spectrum measured after the second Herriott-cell. The upper panel shows measured GDD curves for different coating runs for design PC1711. The lower pane illustrates the output after the second Herriott-cell: output spectrum before and after replacing the HC mirrors PC1711 with the newly coated ones of the same design.

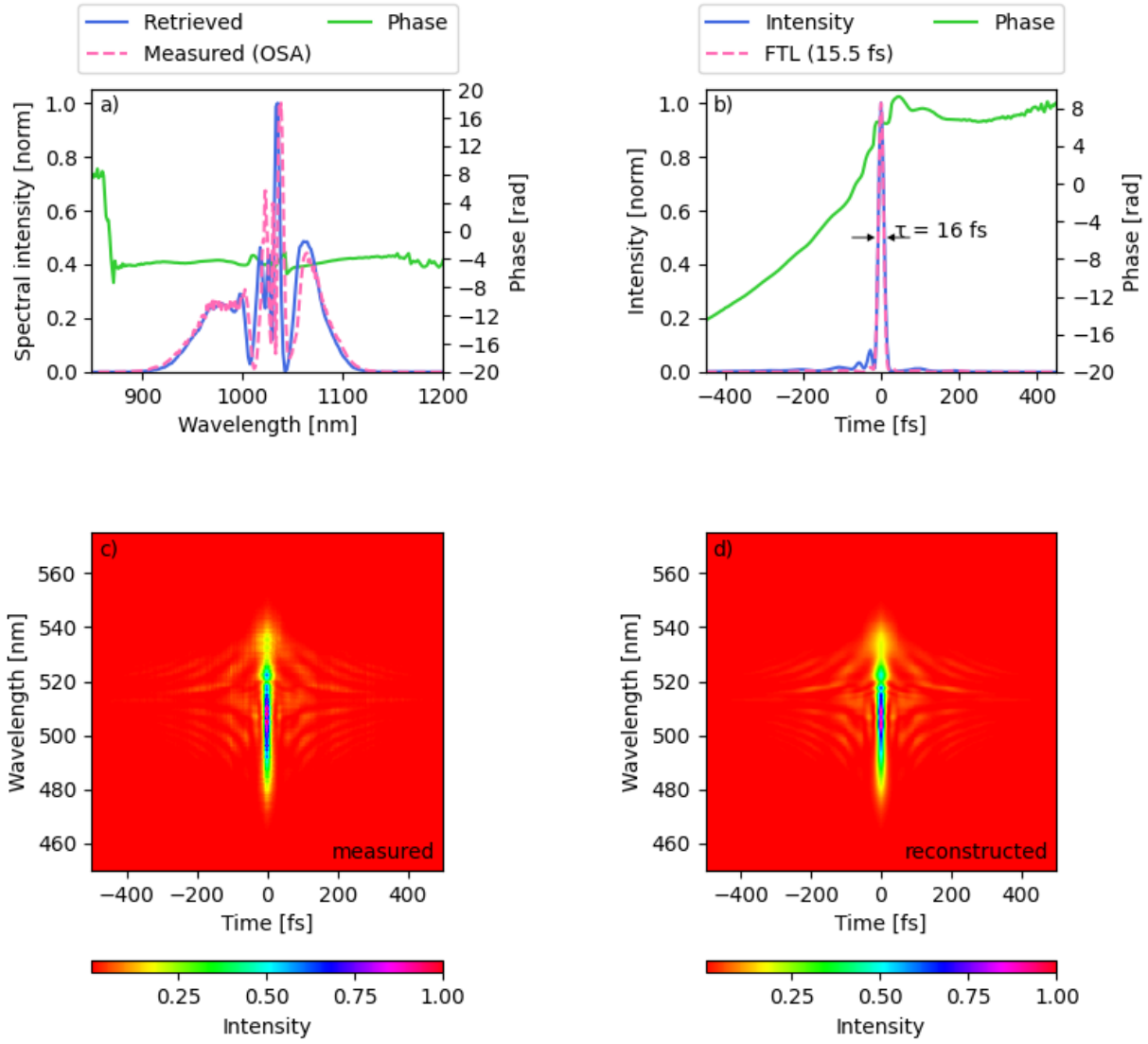

Figure 3.9: Herriott-cell stage-two output characterization. (a) Measured and recovered power spectral density and spectral phase. (b) The temporal phase and intensity envelope of the retrieved pulse, together with its Fourier limit. (c) Measured SHG-FROG trace. (d) Reconstructed FROG trace.

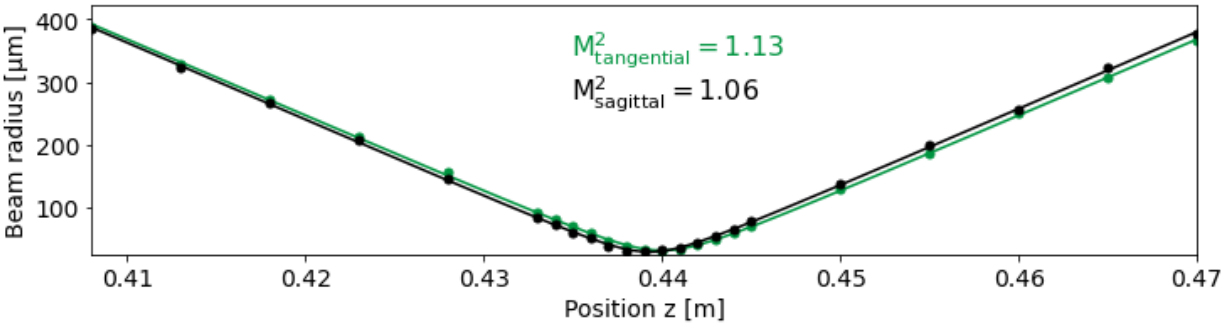

Figure 3.10: Beam quality measurement of the second-stage Herriot-cell output (using Cinogy CinCam CMOS-1203 beam profiler). M^2-measurement according to ISO norm [47]

individual plates and chirped mirrors for temporal re-compression after the 3rd one and was designed to provide fine control over nonlinearity and dispersion. At the output, 10.6 fs linearly polarized pulses with a Fourier transform-limited duration of 9.8 fs, an average power of 100 W, and an M2 value of 1.2 were measured.

Figure 3.11 presents a schematic of the DQWG spectral broadening which is complemented by a photograph of the experimental setup in Fig. 3.12.

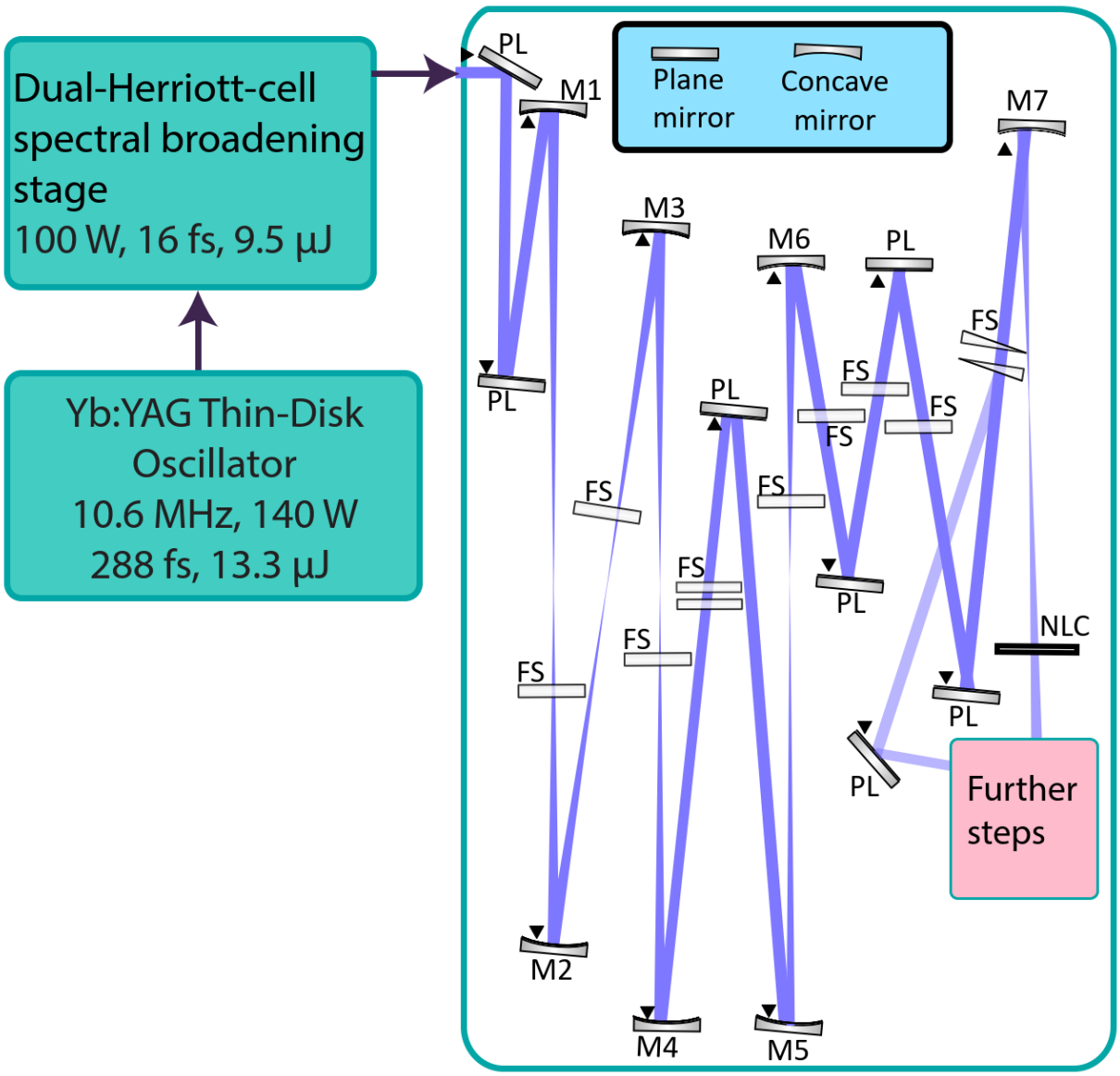

Figure 3.11: Schematic of the distributed quasi wave-guide spectral broadening. M1 concave mirror with 1000 mm ROC focus the compressed collimated output from HC2 to the first broadening medium in the first path of the DGWG, FS: stands for Fused silica while all the broadening plates share the same thickness of 6.35 mm, M2 with 300 mm ROC focuses the beam towards the second FS plate, M3 with 300 mm ROC focuses as well the beam further toward the 3rd broadening plate. M4 with 1000 mm ROC collimates the beam. Afterward, the pulse is compressed utilizing 2x 6.35 mm fused silica plates and one dispersive plate mirror of coating type PC1611, M5 with 1000 mm ROC focuses the beam further to the 4th broadening plate, M6 with 750 mm collimate the beam to a diameter of 3 mm, compression of the pulse after the 4th path is achieved utilizing 2x 6mm and 1x 3mm fused silica plates in addition to three plane dispersive mirrors of coating design PC1611. The pulse splits off right after with the help of pairs of wedges followed by a silver plane mirror that directs the beam for characterizations and further experimental steps. M7 with 900 mm ROC is used also to focus the beam towards the nonlinear crystal for the frequency down conversions processes. M1-M7 all have the coating design PC1711.

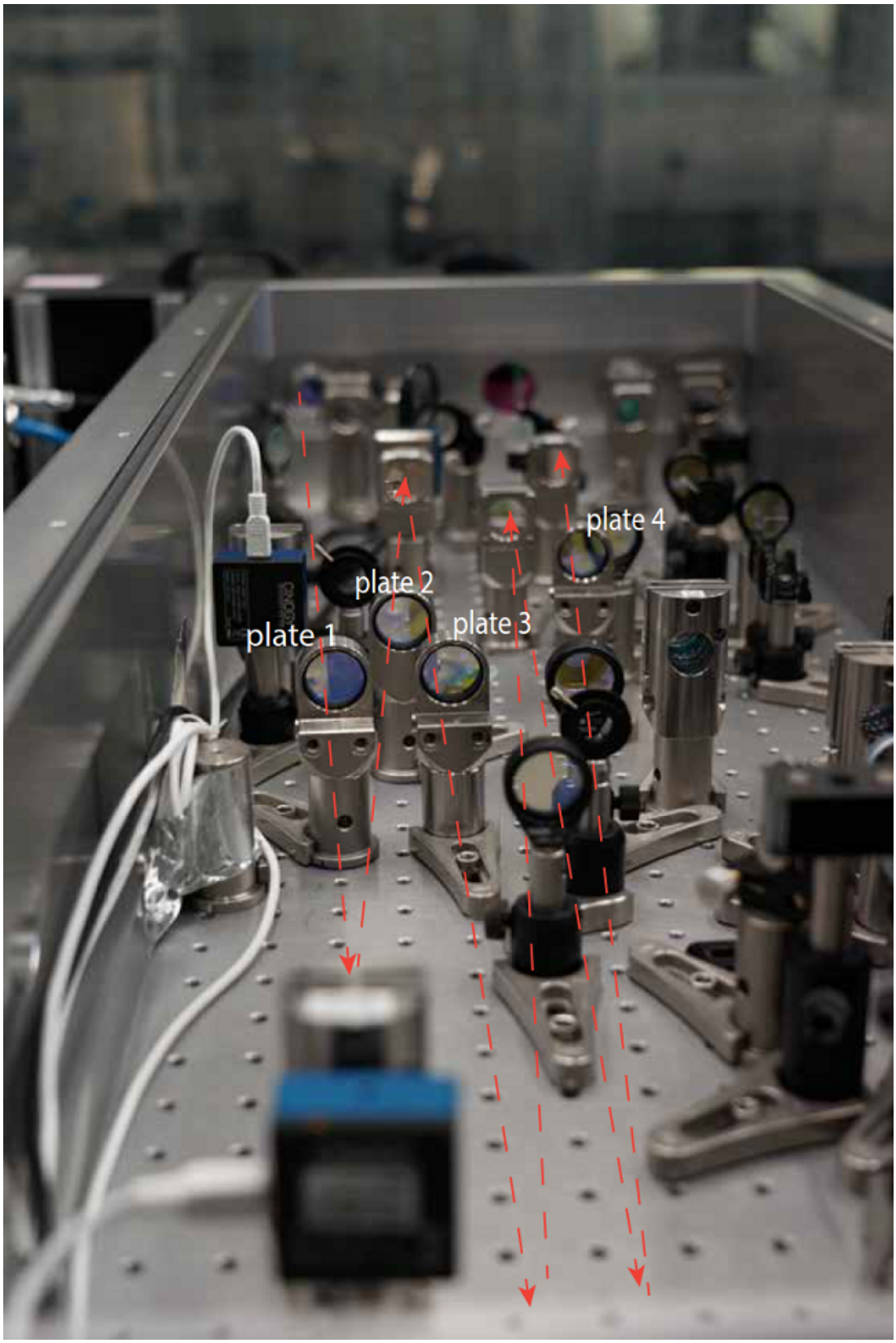

Figure 3.12: Photograph of the distributed quasi wave-guide spectral broadening.

Fig. 3.11 displays the DQWG configuration. A concave mirror (M1) having a ROC of 1000 mm is used to focus the collimated beam coming from the second broadening stage to a beam with roughly a 128 µm radius. To construct a quasi-waveguide setup, subsequent focusing mirrors are located at particular distances based on [126]. As a result, the second mirror (M2) is 291 mm away from the initial focus, while the subsequent mirror (M3) is positioned at a distance of 583 mm from M2. Both M2 and M3 mirrors have a 300 mm ROC and together with M1 and the following mirrors (M4-M7), they have the same wide-band dispersive coating as the second MPC.
Mirror (M4) with a ROC of 1000 mm, which is placed at roughly 790 mm from M3, is employed to collimate the beam after the third broadening FS plate. In each pass of the DQWG, AR-coated FS plates were utilized as nonlinear media. These plates were positioned in the divergent beam after the beam waist to counteract the residual effect of Kerr lensing with natural beam diffraction, thus lowering the likelihood of beam collapse from critical self-focusing.
The middle pulse compression is pursued after the third plate, leading to the equivalent broadening and beam quality compared to [55], without the need to place the fourth plate into a tighter focus, thus avoiding the higher intensity and eventually instability due to frequent optical damage. Doing so significantly improved the day-to-day reproducibility and resulted in a stable few-cycle NIR laser source. For this compression, 2x 6.35mm FS plates were employed in addition to a dispersive mirror with PC1611 coating, which has an average GDD of -150 fs^2.

The individual plates were placed at distances 600 mm, 350 mm, and 340 mm from mirrors M1, M2, and M3, respectively. Optical-spectrum analyzer measurements were performed, and the Fourier transform limit of the pulses after each of the plates is 14.6 fs, 13.2 fs, and 11.9 fs, respectively, after each path. The position of the fused silica plate in each pass has been chosen to obtain a 10% reduction in the Fourier-transform limit in each pass. The latter was controlled by gradually decreasing the plate's distance to the beam waist while measuring the spectrum using an optical-spectrum analyzer.
Figure 3.13 provides a detailed characterization of the output of the third plate of the DQWG, utilizing SHG-FROG. Part (a) shows the retrieved power spectral density and spectral phase obtained through FROG analysis. An optical spectrum analyzer (OSA) was used to measure the power spectral density. Part (b) displays the temporal phase and intensity envelope of the retrieved pulse, along with its Fourier limit. (c) Shows the measured SHG-FROG trace. Part (d) presents the reconstructed FROG trace. The compressed pulses exhibit a pulse duration of 11.3 fs at full width at half maximum (FWHM).
A beam quality measurement of the third plate of the DQWG output is shown in Fig. 3.14, in which the retrieved M^2 measurement was 1.12 and 1.11 tangential and sagittal, respectively.
Mirror M5 with 1000 mm ROC is utilized to focus the collimated compressed pulse to the fourth fused silica plate that has been placed at a distance of 610 mm from it. On the other hand, a mirror M6 with 750 mm ROC was used to collimate the output.

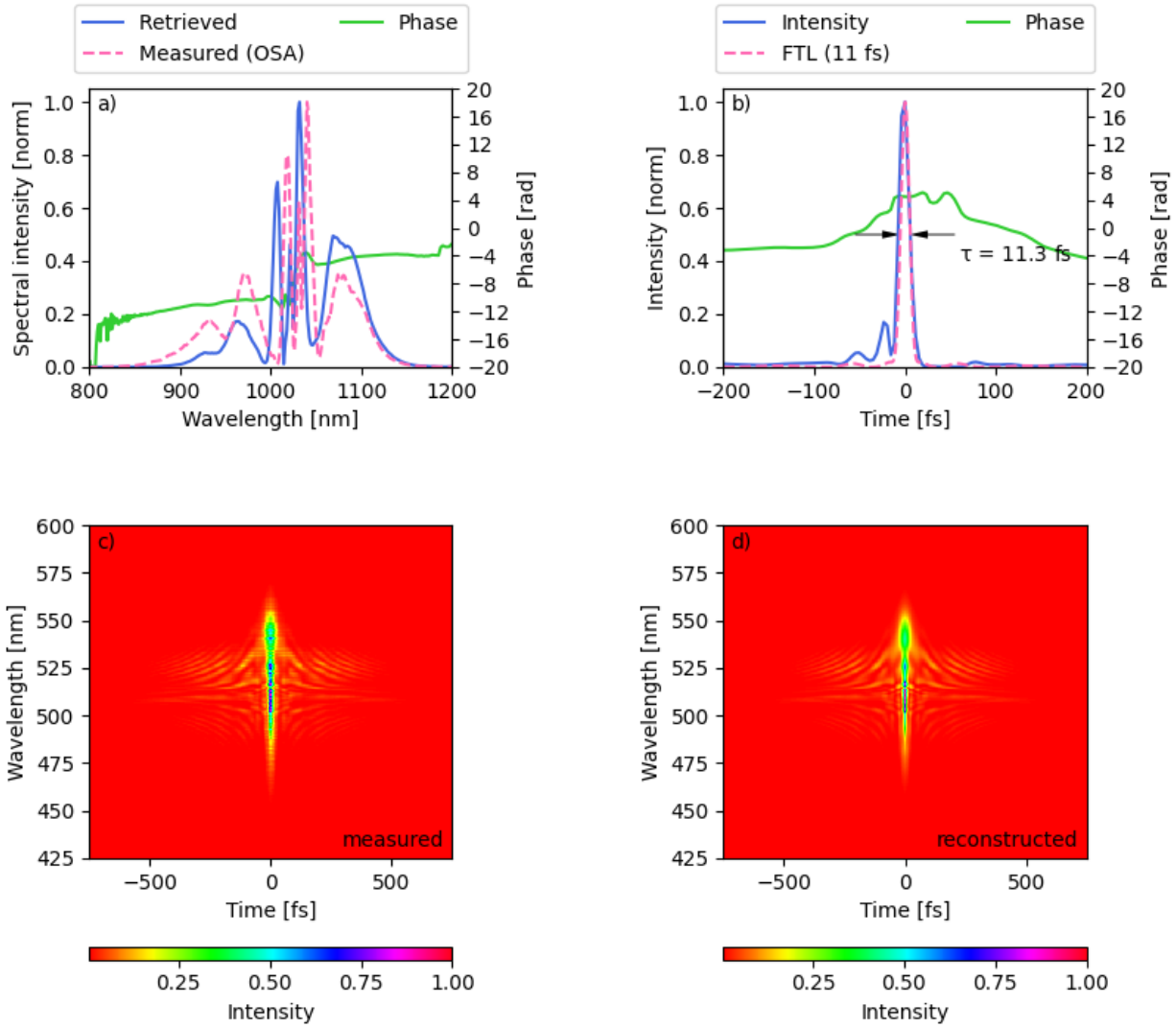

Figure 3.13: Output pulse characterization after 3rd plate of the DQWG. (a) Measured and retrieved power spectral density and spectral phase. (b) The retrieved pulse's temporal phase and intensity envelope, together with its Fourier limit. (c) Measured SHG-FROG trace. (d) Reconstructed FROG trace.

Optical-spectrum analyzer measurements show a spectral width that supports Fourier transform-limited pulses of 9.8 fs long.
Subsequently, dispersion compensation was carried out using three plane chirped mirrors of coating type PC1611 with a total GDD of -450 fs^2 in addition to two fused silica plates each with a thickness of 6 mm plus one with a thickness of 3 mm, resulting in a pulse duration of 10.6 fs (corresponding to $\approx$ 3.1 optical cycles at a center wavelength of 1030 nm), as shown in Fig. 3.15. At the full input power of 100 W, the output power at the DQWG's output is 99 W, representing an optical efficiency of 99 percent.
Fig. 3.15 provides a detailed characterization of the output of the fourth plate of the

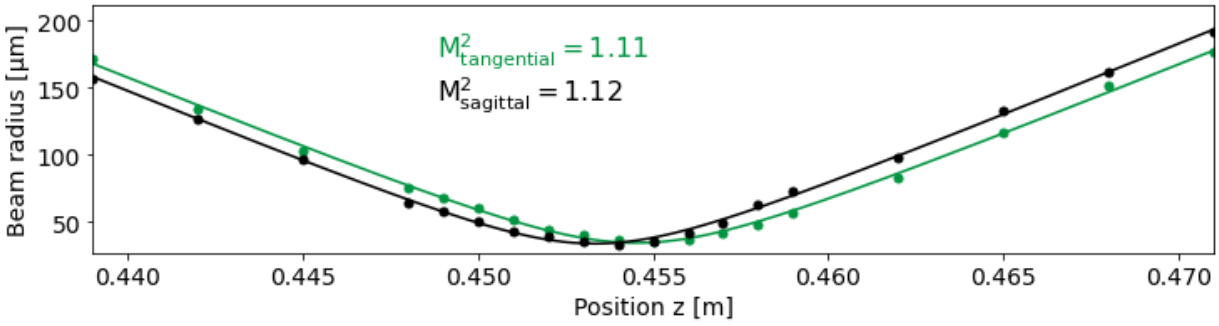

Figure 3.14: Beam quality measurement of the 3rd plate (in the DQWG) output (using Cinogy CinCam CMOS-1203 beam profiler). M^2-measurement according to ISO norm [47] is 1.12 and 1.11 in tangential and sagittal respectively.

DQWG, utilizing SHG-FROG. Part (a) shows the retrieved power spectral density and spectral phase obtained through FROG analysis. An optical spectrum analyzer (OSA) was used to measure the power spectral density. Part (b) displays the temporal phase and intensity envelope of the retrieved pulse, along with its Fourier limit. (c) Shows the measured SHG-FROG trace. Part (d) presents the reconstructed FROG trace. The compressed pulses exhibit a pulse duration of 10.6 fs at full width at half maximum (FWHM).
The beam quality measurement of the fourth plate of the DQWG output is shown in Fig. 3.16, in which the M^2 values in the tangential and sagittal planes are 1.19 and 1.13, respectively.
The beam profiles after the second stage Herriott cell and after the fourth path of the DQWG are given in Fig. 3.17 in the normal and saturated view taken utilizing the Cinogy CinCam CMOS-1203 beam profiler. (a) The beam profile after HC2 shows a beam size of approximately 4.5 mm. (b) A saturated view, captured with a 10x exposure, demonstrates the absence of a ring around the beam. (c) After passing through the fourth plate, the collimated beam exhibits a beam size of approximately 2.8x3 mm in X and Y directions. (d) A saturated view, taken with a 10x exposure, confirms that there is no ring present around the beam.
The absence of a ring in the beam profile indicates that there are no significant diffraction effects. This is crucial as it ensures a higher level of spatio-spectral homogeneity, which is essential for maintaining the desired characteristics of the beam. When a ring is present, it signifies an uneven distribution of energy across the beam profile, leading to variations in intensity and spectral properties. This lack of homogeneity can negatively impact the performance and efficiency of the system, hindering its optimization for the intended application. The fact that the beam profile does not exhibit a ring is particularly significant for systems with high compression rates. These systems often encounter challenges in achieving spatio-spectral uniformity due to the nonlinear optical effects, such as self-focusing, and the inherent aberrations introduced by the Kerr lens.
Fig. 3.18 shows beam profiles taken from a beam leakage of six different mirrors located

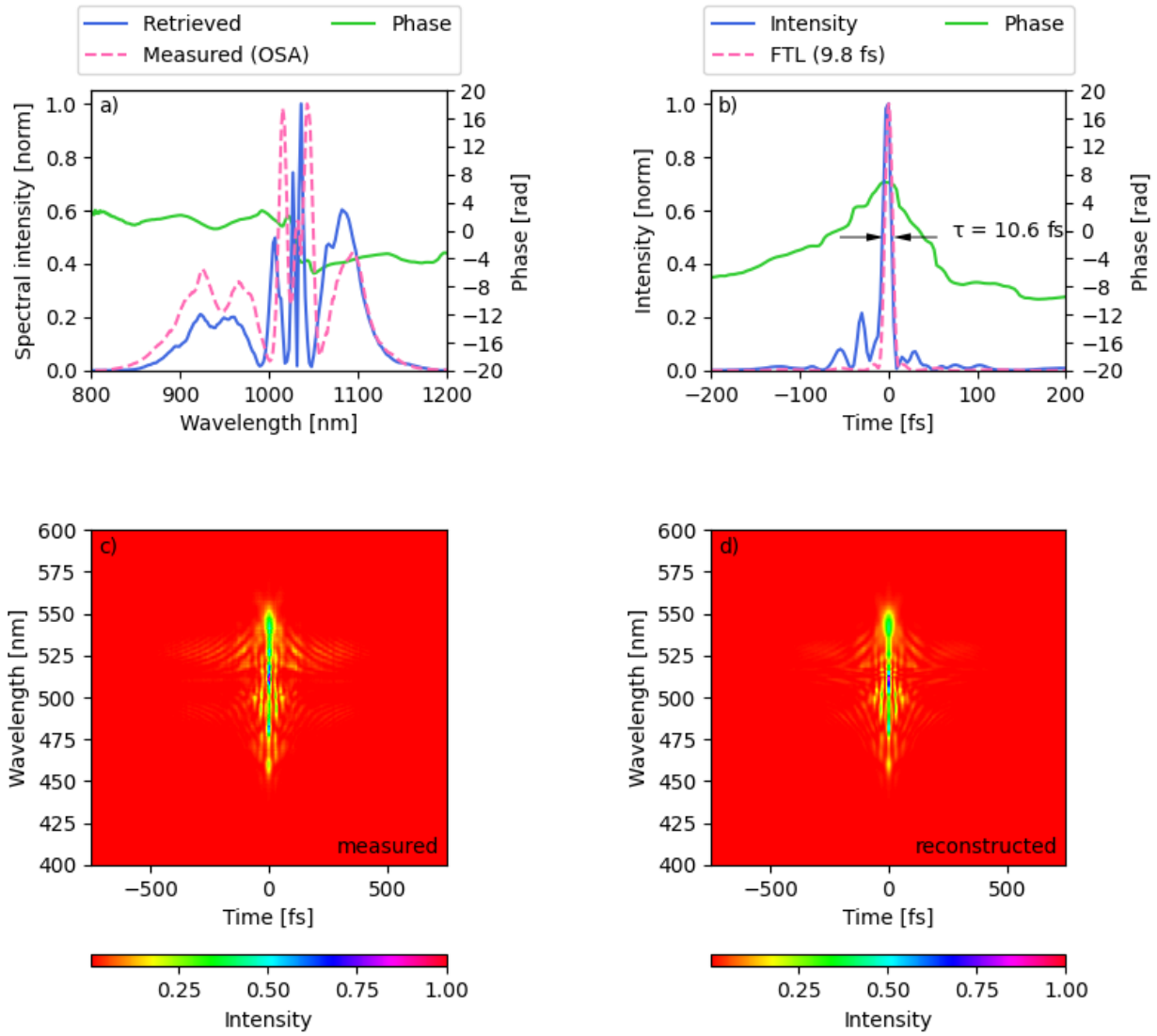

Figure 3.15: Output pulse characterization after 4th plate of the DQWG. (a)Measured and retrieved power spectral density and spectral phase. (b)The retrieved pulse's temporal phase and intensity envelope, together with its Fourier limit. (c) Measured SHG-FROG trace. (d) Reconstructed FROG trace.

after each of the Herriott-cell broadening stages, as well as after each path of the DQWG. The beam profiles were captured using cameras placed behind each mirror. Subfigure (a) depicts the beam profile after HC1, (b) the beam profile after the second stage HC, (c) the beam profile after the first path of DQWG, (d) the beam profile after the second path of DQWG, (e) the beam profile after the third path of DQWG, (f) the beam profile after the fourth path of DQWG. This figure provides important information about the quality and stability of the beam as it passes through the different stages of the experimental

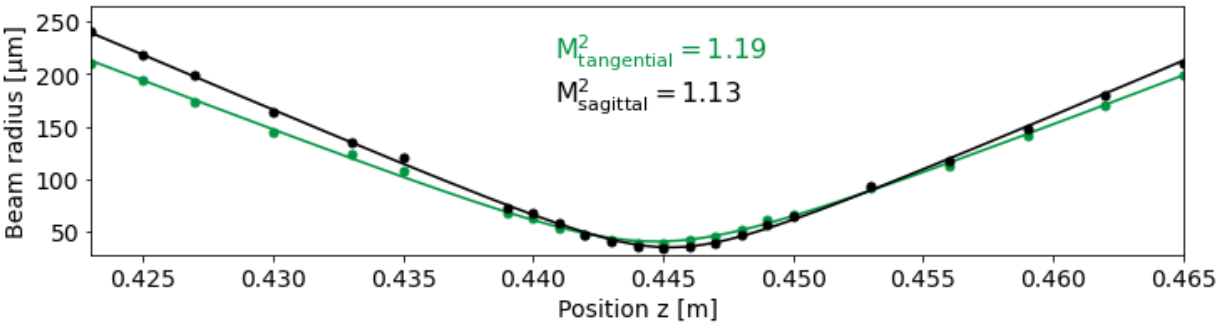

Figure 3.16: Beam quality measurement of the 4th plate (in the DQWG) output (using Cinogy CinCam CMOS-1203 beam profiler). M^2-measurement according to ISO norm [47] is 1.19 and 1.13 in tangential and sagittal respectively.

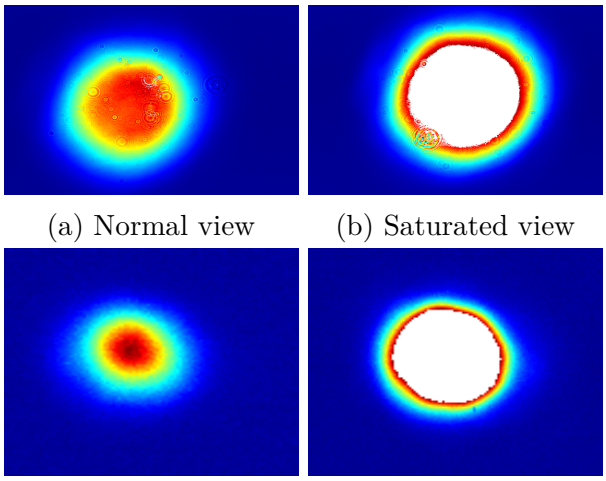

(a) Normal view (b) Saturated view

(c) Normal view (d) Saturated view

Figure 3.17: Beam profiles of a collimated beam at different stages of the setup. (a) Beam profile after the second Herriott cell broadening stage (HC2) with a size of approximately 4.5 mm. (b) Saturated view with 10x exposure showing no ring around the beam. (c) Beam profile of the collimated beam after the fourth plate with a size of roughly 2.8/3 mm in both X and Y directions. (d) Saturated view with 10x exposure showing no ring around the beam.

setup. Monitoring beam profiles is crucial to identify potential issues in the system and to ensure that the beam remains intact throughout the process.

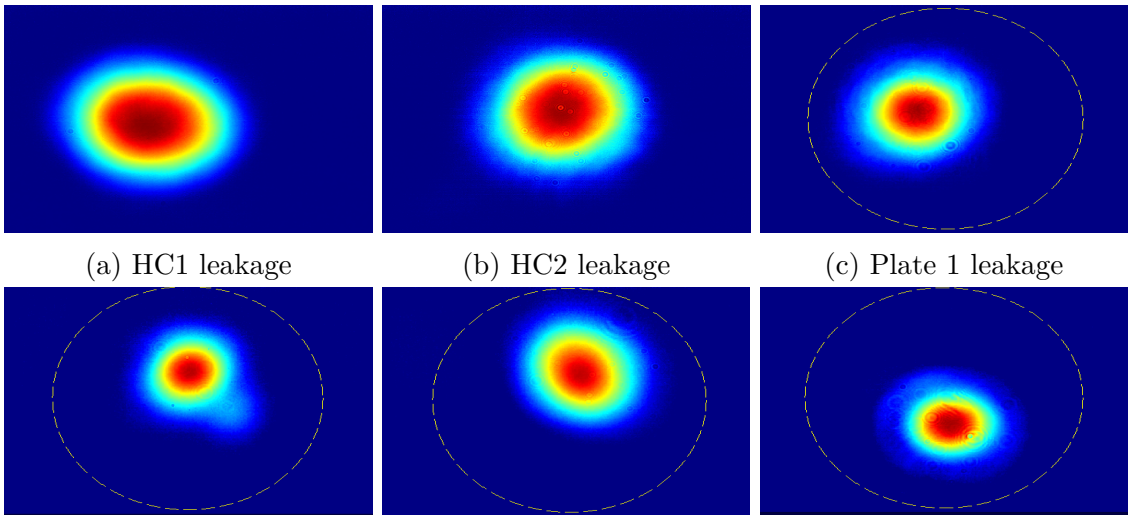

(a) HC1 leakage (b) HC2 leakage (c) Plate 1 leakage

(d) plate 2 leakage (e) plate 3 leakage (f) plate 4 leakage

Figure 3.18: Live monitoring of beam evaluation after each plate. Beam profiles captured from beam leakage of mirrors located after each Herriott cell broadening stage and path of the DQWG. Sub-figures (a) to (f) show the beam profiles after HC1, HC2, and paths 1 to 4 of the DQWG, respectively. The beam profiles were captured using cameras placed behind each mirror, providing important information about beam quality and stability within the experimental setup.

Chapter 4

Multi-Octave waveform-stable mid-infrared light source

Building on the results of the previous chapter, which focused on the development of few-cycle near-IR pulses, this chapter delves into the generation of waveform-stable mid-infrared (MIR) light. While the previous chapter established the foundation for producing ultrashort pulses in the near-IR region, this chapter extends the research to address the challenge of generating stable and precise MIR waveforms. The goal of this chapter is to explore techniques and methodologies for achieving waveform stability in the MIR spectral range. By attaining waveform stability, we aim to produce MIR light with well-defined and reproducible temporal profiles, enabling accurate and reliable spectroscopic measurements in this important wavelength range.

4.1 Introduction

Asymmetric charge distributions in molecules are responsible for the efficient coupling of infrared (IR) radiation to fundamental rotational-vibrational modes of the constituent (groups of) atoms via electric dipole moments [35]. The eigenfrequencies, strengths, and decay times of these molecular-scale oscillations are determined by the atomic constituents, their conformation, and dynamics. This results in a spectroscopic 'fingerprint' unique to the molecular sample, and is experimentally accessible by probing with broadband IR light. Consequently, IR spectroscopy serves a wide range of applications [36], from fundamental science [35, 36, 87] to chemical analysis [57] to biology and medicine [9].
Two highly desirable properties of IR sources for molecular fingerprinting are (i) broad bandwidth, which ideally covers the entire molecular fingerprint region (usually defined to start at 2.8 µm – or 3700 cm^{-1} – corresponding to the eigenfrequency of the O-H stretching vibration), and (ii) high brilliance, translating to sample-specific IR fingerprints strong enough to be detectable [100]. In addition, (iii) spatial coherence and (iv) temporal coherence enable advanced spectroscopy schemes.

For many spectroscopic techniques, (i) and (ii) are sufficient; however, more advanced spectroscopic techniques require (iii). Most prominently, spatial coherence allows for long interaction lengths or multiple passes through gaseous samples, enhancing sensitivity, and the frequency-comb nature of phase-controlled broadband light enables high-resolution spectroscopy with accurate absolute-frequency calibration
[29, 30, 77, 85, 90, 103, 109, 119, 120, 132, 135, 138].
Equally importantly, temporal coherence affords outstanding control over (and reproducibility of) broadband optical waveforms. In time-domain spectroscopy techniques, the confinement of broadband optical spectra to merely a few highly controlled oscillations of the optical wave can be used, for instance, to probe the non-linear response of matter to an intensive excitation at the level of the electric field of light [90, 120]. The temporal confinement of a broadband excitation has been shown to possess advantages of sensitivity even in linear spectroscopy, stemming from the temporal separation of the sample-specific response from the, often orders of magnitude, stronger and shorter excitation [109].
Due to the lack of suitable gain media, there is currently no laser-based source that can cover the entire molecular fingerprint region while also possessing the aforementioned desired properties for coherent spectroscopy. For that, most coherent broadband mid-IR sources rely on the parametric down-conversion of ultrashort laser pulses produced by established visible/near-IR laser technologies [15, 48, 119]. Although synchrotron facilities provide high brightness ultra-broadband coherent radiation, they come with significant drawbacks such as high cost, limited availability, and the need for building-scale instrumentation [8, 33, 37].
Compact sources such as quantum cascade [3, 22, 76, 113, 122, 140] and CO2 lasers [104], can provide direct mid-IR generation, but have narrow spectra. To overcome this limitation, supercontinuum generation in nonlinear fibers [80, 95, 101], waveguides [147], and crystals [104] has been studied to achieve broader mid-IR spectra, but they are limited to average powers between 10 µW and 50 mW.
Another technique for high-power mid-IR emission is optical parametric oscillators (OPO) [2], and amplifiers (OPA) [40, 124], which can provide a high average output power of up to 5 µm using oxide nonlinear crystals. For longer wavelength emissions, non-oxide nonlinear crystals are used for transparency properties, with narrow-linewidth OPA achieving average powers between 1 and 100 mW and tunability between 4.5 and 20 µm [52, 118, 127].
In recent years, coherent IR sources based on femtosecond lasers have demonstrated the feasibility of different combinations of the properties (i)-(iv); see, e.g.,
[12, 18, 20, 26, 27, 41, 44, 48, 59, 64, 70, 71, 110, 128, 131, 134, 150] and references therein. However, simultaneously achieving these properties in a robust and compact source remains a challenge. The upcoming sections will discuss this challenge and propose promising and viable solutions.
Building upon the results obtained in the previous chapter, the following section describes the development of a multi-octave waveform-stable mid-Infrared (MIR) source within the framework of this thesis.

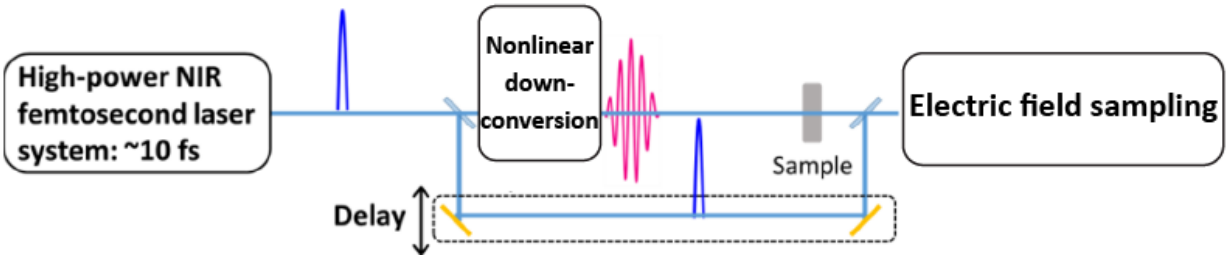

Figure 4.1: Field-resolved infrared spectroscopy technique, in which short near-infrared pulses of about 10 femtoseconds are used to generate broadband, phase-stable infrared light through intrapulse difference-frequency generation-process. This light in turn triggers specific vibrations in a molecule, which make up the coherent response of the sample and are detected utilizing the electro-optic sampling technique.

4.2 Experimental work

The simultaneous achievement of the aforementioned FRS properties in a robust and compact source has remained a challenge. In this section, we address this obstacle by employing intrapulse difference-frequency generation (IPDFG) in a multicrystal in-line geometry, driven by femtosecond pulses generated by a Yb:YAG thin-disk oscillator.
As presented in detail in the previous chapter, the initial pulse train in our setup is produced by a Kerr-lens mode-locked Yb:YAG thin-disk oscillator with a repetition frequency of 10.6 MHz [107]. At an average output power of 140 W, this frontend operates in air and delivers pulses with a duration of 300 fs, spectrally centered at 1030 nm. To achieve the 10-fs-scale pulse durations necessary for ultra-broadband IPDFG, with high throughput efficiency, we employed extra-cavity pulse compression based on multiple passes through thin Kerr media [10, 96, 121, 133, 143]. Specifically, 120 W from the oscillator output was sent to a dual-stage Herriott cell-type spectral broadening along with a subsequent chirped mirror compressor [56], followed by a distributed quasi-waveguide [55].
A train of 10.6-fs linearly polarized pulses with a Fourier-transform-limited duration of 9.8 fs and an average power of 100 W, has been used to drive intrapulse difference-frequency generation (IPDFG), as illustrated in Fig. 4.2, in a dual-crystal in-line geometry. First, a fraction of the pulses, which have been used for gating the newly generated MIR frequencies via EOS, are split off using an uncoated pair of fused-silica wedges. The split pulses are then focused by a 900 mm ROC concave mirror M7 in Fig. 3.11 (for simplicity, here it is illustrated as a lens), and MIR light is generated. The latter has been separated from the driving NIR pluses utilizing a ZnSe material-based beam splitter (to be introduced later in subsection 4.2.2) and afterward sent for phase and field measurements via EOS.
Custom-made multilayer band-pass filters coated on fused-silica substrates have been implemented to mitigate the peak power intensity by blocking the central part of the NIR spectrum, thus preventing the damage threshold of the nonlinear crystals from being

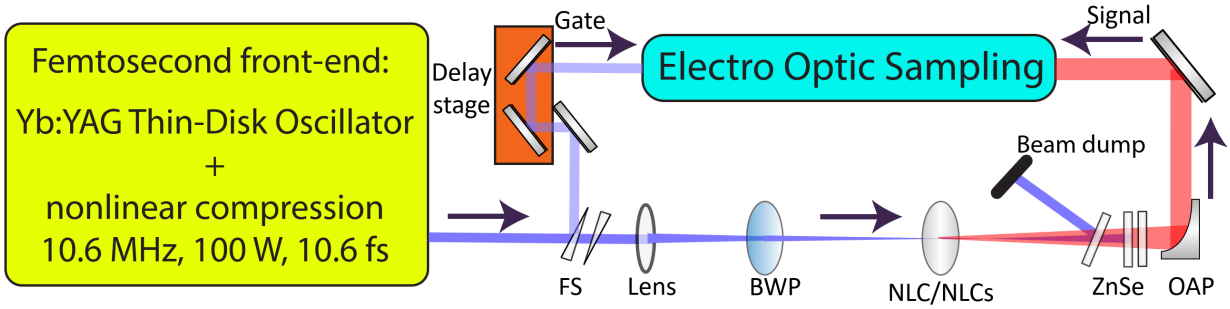

Figure 4.2: Schematic of IPDFG setup in which the high-power 10-fs-scale pulses of a 10.6-MHz-repetition-rate are used to drive IPDFG in a multi-crystal in-line geometry. A fraction of the pulses, which will be used later as a gate to probe the newly generated frequencies via the EOS process, is split off using an uncoated pair of fused-silica wedges before they are focused by a 900 mm ROC concave mirror (simplified as a lens here), afterward mid-infrared light is generated. The latter will be separated from the driving near-infrared pulses using a ZnSe material-based beam splitter and afterward sent to EOS

exceeded. Since the targeted IPDFG process would be phase-matched primarily in the outer parts of the driving spectrum, the cutoff frequency would be increased, and thus the broadest possible MIR spectral output would come to reach.
The filter [1] purpose was to operate optimally when placed at a 45 ° angle of incident (AOI). It demonstrates outstanding performance, transmitting over 97% of incident light within the spectral range between 1025 and 1055 nm, while effectively reflecting the majority of the input spectrum outside of this range.
Figure 4.3 shows three different transmission curves of the filter, for three different AOI values, of 44°, 45°, and 46° in blue, red, and black lines, respectively. From the illustrated curves, since the larger the AOI the further blue-shifted the curves are, one can conclude that 46° AOI is more suitable in the case of our input spectrum of the near-infrared driving pulses, which is centered around 1030 nm.
The filter has been implemented and tested in our setup under 46° AOI. In this test, two sequential filters have been used to suppress a sufficient amount of the near-infrared input power. In each filter, approximately 15%, namely 15 W, have been transmitted through the filter and eventually blocked. The near-infrared pulses that have been reflected from the filter were measured utilizing FROG and the results are illustrated in Fig. 4.4.
Figure 4.4 presents the spectral characterization of the near-infrared driving input pulse with and without employing the central-wavelength bandpass filter given in red and cyan lines, respectively.
Temporal characterization utilizing FROG measurements of the input NIR pulses has shown that the pulse has been elongated after being reflected twice from the bandpass filter to 11.5 fs compared to 10 fs without using the filter. We attribute this to the suppression of the blue components part of the input spectrum of the driving pulse,

[1] was numerically designed and coated by Dr. Vladimir Pervak et al. within our research group

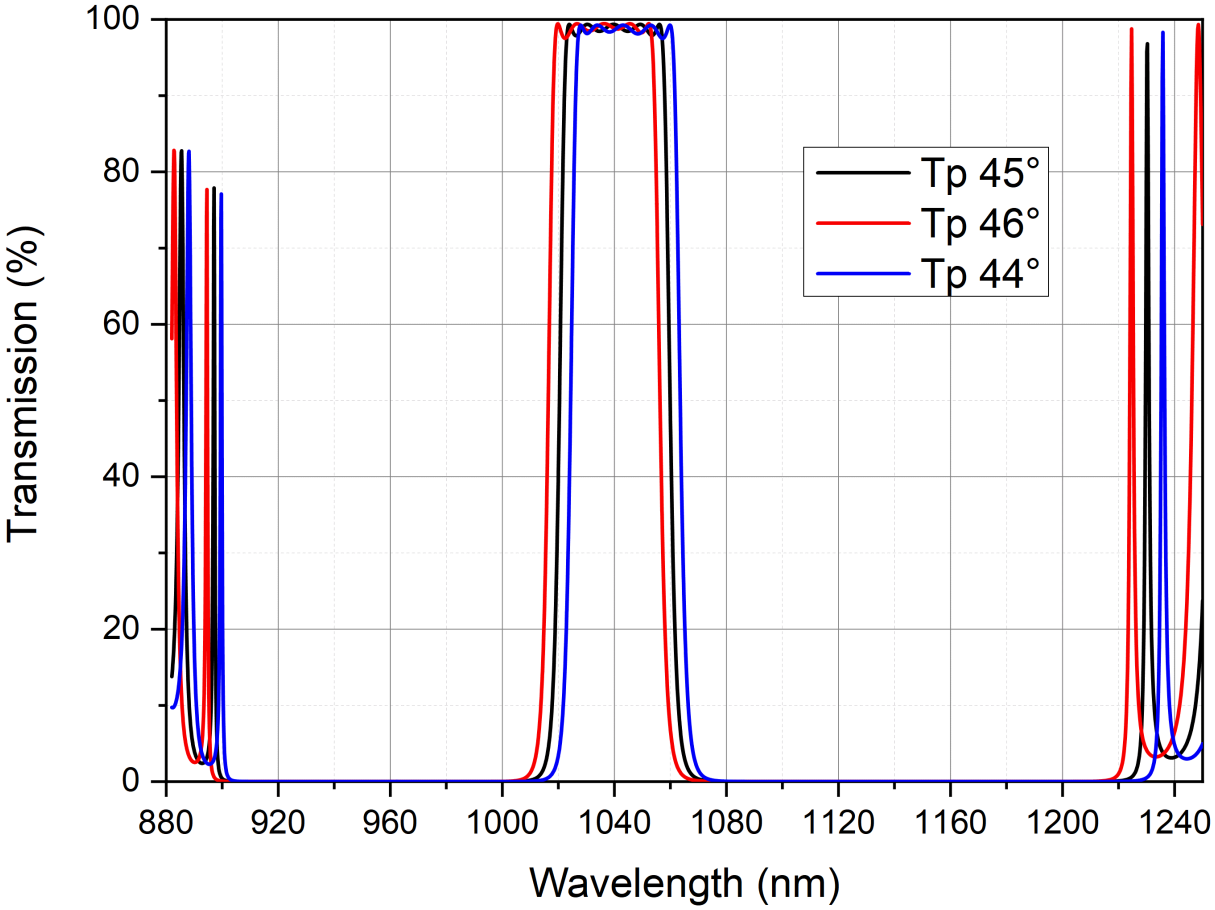

Figure 4.3: Custom-made band-pass filters have been implemented to mitigate the peak power intensity by blocking the central part of the NIR spectrum, thus preventing the damage threshold of the nonlinear crystals from being exceeded. Transmission curves of the band-pass filter: R(45°p) > 99.9% in the ranges 910-1010 nm and 1070-1200 nm, while T(45°p) > 97% in the range 1025-1055 nm.

which one sees in Fig. 4.4.
Ultimately, we proceeded with the subsequent experimental procedures without incorporating the band-pass filter due to the observed pulse elongation mentioned earlier. However, it is worth noting that enhancing the coating bandwidth holds the potential to allow for positioning the NLC in closer proximity to the focal point without inducing optical damage. This, in turn, could lead to an eventual amplification in the conversion efficiency of the IPDFG process.

4.2.1 Power scaling using bichromatic wave plate

Among other frequency down-conversion processes, in particular, in the IPDFG the pump and the signal are within the single pulse; for that, the spectrum of the latter has

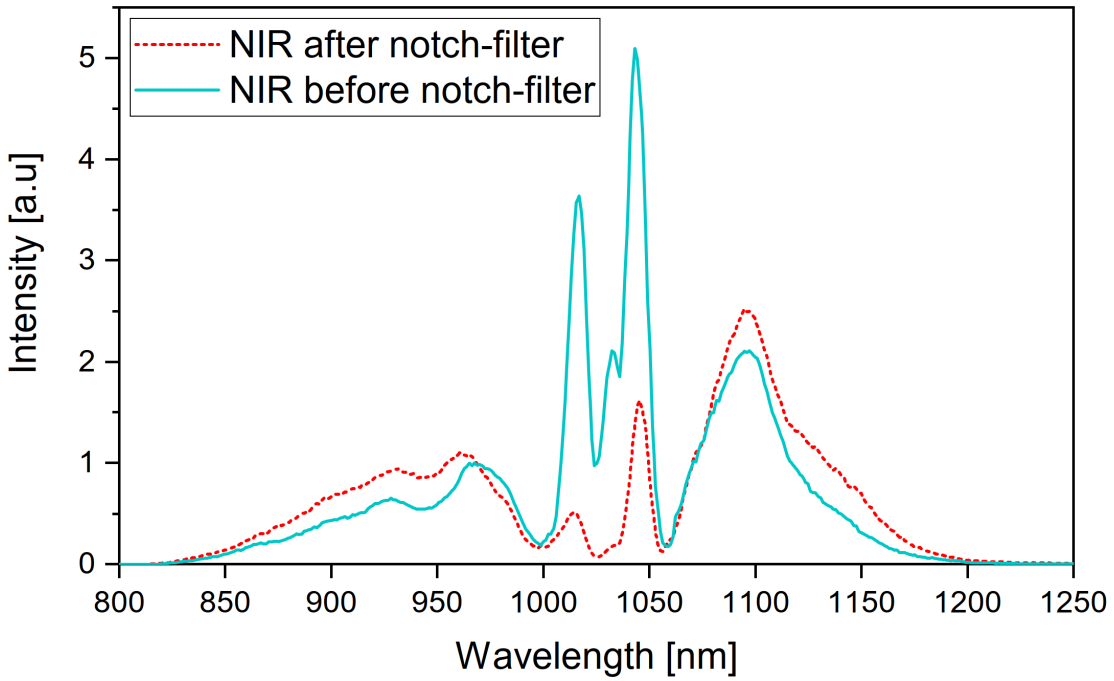

Figure 4.4: Power spectral density of the near-infrared driving input pulse with and without employing central-wavelength band-pass filter given in cyan and orange lines respectively.

to provide both ordinary and extraordinary polarized components to satisfy the phase-matching conditions. In the conventional scheme and during the last two decades [18, 64, 70, 71], a half-wave plate is used to turn the polarization of light by roughly 45°.

In our case, and to maximize the conversion efficiency while simultaneously reaching a broad spectral coverage, (i) IPDFG type I phase matching was chosen [148], and (ii) a polarization converter known also as a bichromatic waveplate (BWP) (manufactured by B. Halle) is employed.

To achieve type-I phase matching, polarization rotation of the lower-frequency part of the driving spectrum (signal) with respect to the high-frequency part (pump) was achieved utilizing the bichromatic waveplate (BWP). Fig. 4.7, provides a convenient way to optimize the polarization distribution of the driving field for the type I phase matching [20, 67, 43].

The BWP is a combination of three crystal plates (quartz) stacked as shown in Fig. 4.5, in which the construction, axis orientation, as well as thickness of each crystal plate (quartz) in the bichromatic waveplate are given. The plates are mounted with air gaps, each with an anti-reflection coating on both sides. The double arrow in Fig. 4.5 indicates the orientation of the slow axis of each crystal (quartz), also given on the right side in degree. On the other hand, the left-hand-side number indicates each crystal (quartz) thickness.

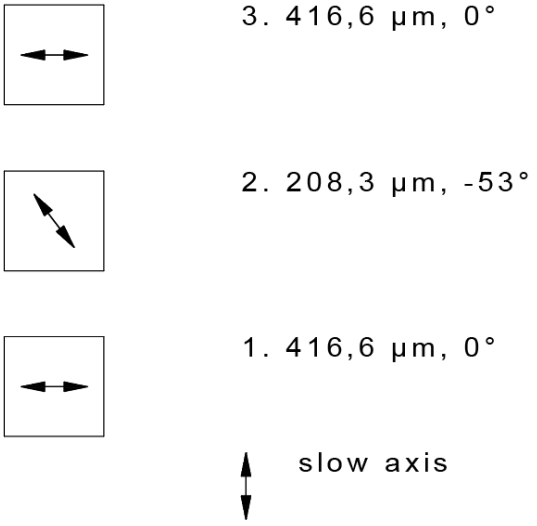

Figure 4.5: Construction and axis orientation of the BWP. The slow axis orientation of each crystal is given in degrees, while the numbers give each crystal thickness.

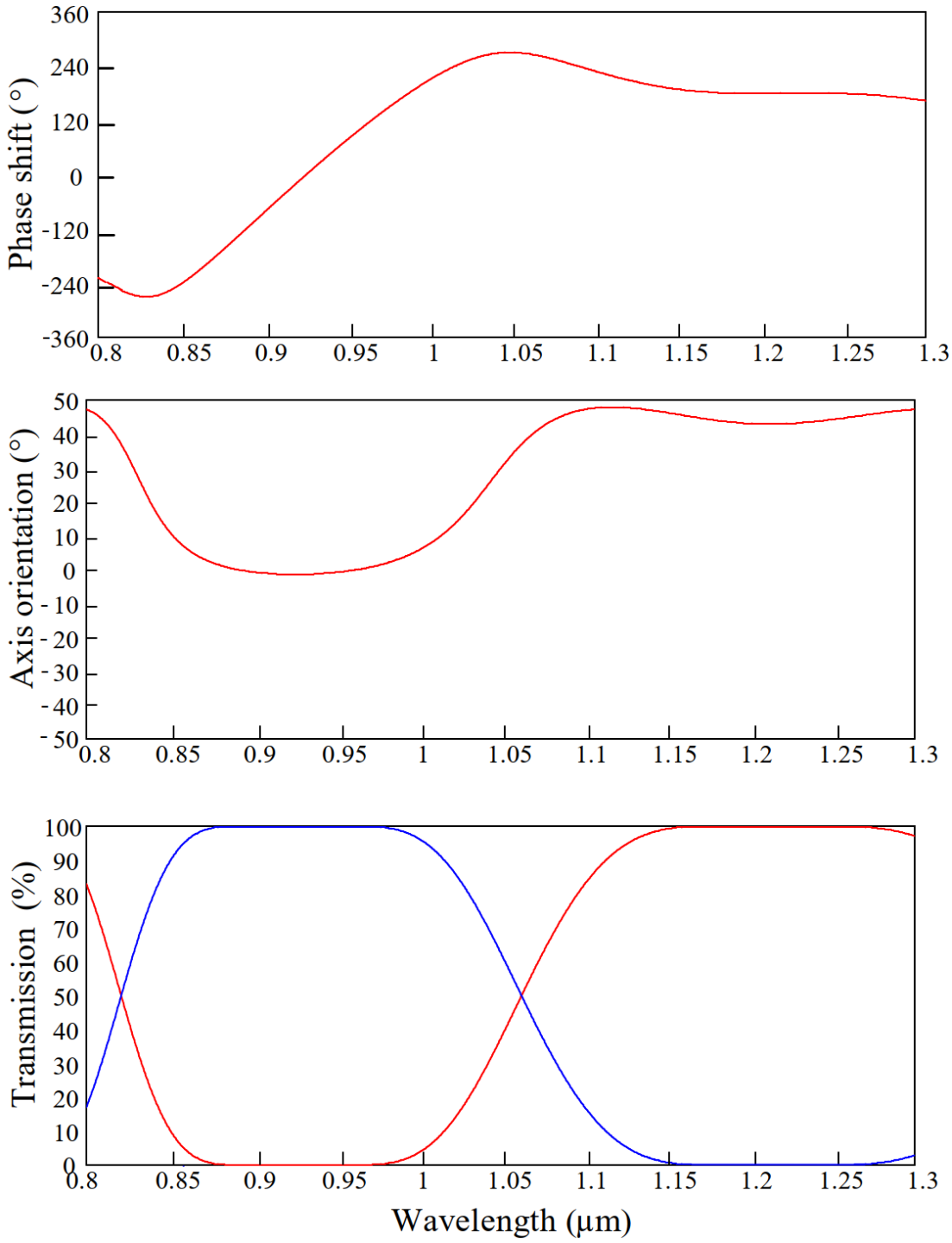

Figure 4.6: Spectral characteristics of the transmission through the BWP. The upper panel illustrates the phase shift between the slow and fast axis in degrees. The middle one shows the effective fast and slow axes orientation of the three crystals combined, which is not constant but shows a variation over the spectrum. The lower one shows the transmission with an analyzer at 90° and 0° to the input, in red and blue lines, respectively.

The spectral characteristics of the combination are shown in Fig. 4.6. The upper panel illustrates the phase shift between the slow and fast axes in degrees over the whole spectral range of interest. The middle panel shows the effective fast- and slow-axes orientation of the three combined crystals. Since the center plate is mounted at an oblique angle, the orientation of the effective fast and slow axes of the combination is not constant but shows a variation over the spectrum. This offers an additional degree of freedom that helps to achieve the desired polarization effect. To understand the way the BWP is working, we divide its effect into three different spectral ranges:

(i) In the range of 1150-1250 nm, the combination acts as an achromatic half-wave plate (phase shift 180°) with an axis orientation at 45°; thus, it results in a polarization rotation of 90°.

(ii) In the range of 880-980 nm, the phase shift is not achromatic. However, the axis (the effective fast and slow axes orientation of the three combined crystals) is 0° in this range, which means that the input polarization is an eigenstate of the plate. Therefore, the polarization leaves the plate unchanged in this range.

(iii) In between the two design ranges, there is a steep variation in both the phase shift and the axis angle. This result is a rapid change in the polarization state.

The lower panel in 4.6 shows the transmission with an analyzer at 90° and 0° to the input, in red and blue lines respectively. In the range between 1150 and 1250 nm, we see high transmission with an analyzer at 90° to the input and low transmission with an analyzer parallel to the input (red line). The opposite is valid in the range of 880-980 nm, where we see high transmission with an analyzer parallel to the input and low transmission with an analyzer at 90° to the input (blue line).

Figure 4.7 illustrates the polarization tailoring in detail. In (a), we see the polarization distribution and evolution of the spectra upon propagation through the crystal, with respect to the ordinary (o) and extraordinary (e) optical axes of the crystal. The colors represent the spectral distributions on the axes (and not temporal information). In (b) we see the near-IR intensity spectra (colored) measured after the BWP on the two polarization axes, and the input spectrum (dashed line).

Using these multi-order wave plates allowed us to push the efficiency of the IPDFG process by a factor close to four, which is the highest factor, to the best of our knowledge, that has been reported when such an optic is used [20, 67]. This optic allowed us to reach both target goals: (i)obtaining multi-octaves spanning the MIR spectrum and (ii) at the same time boosting the efficiency. Further details will be presented in the following sections.

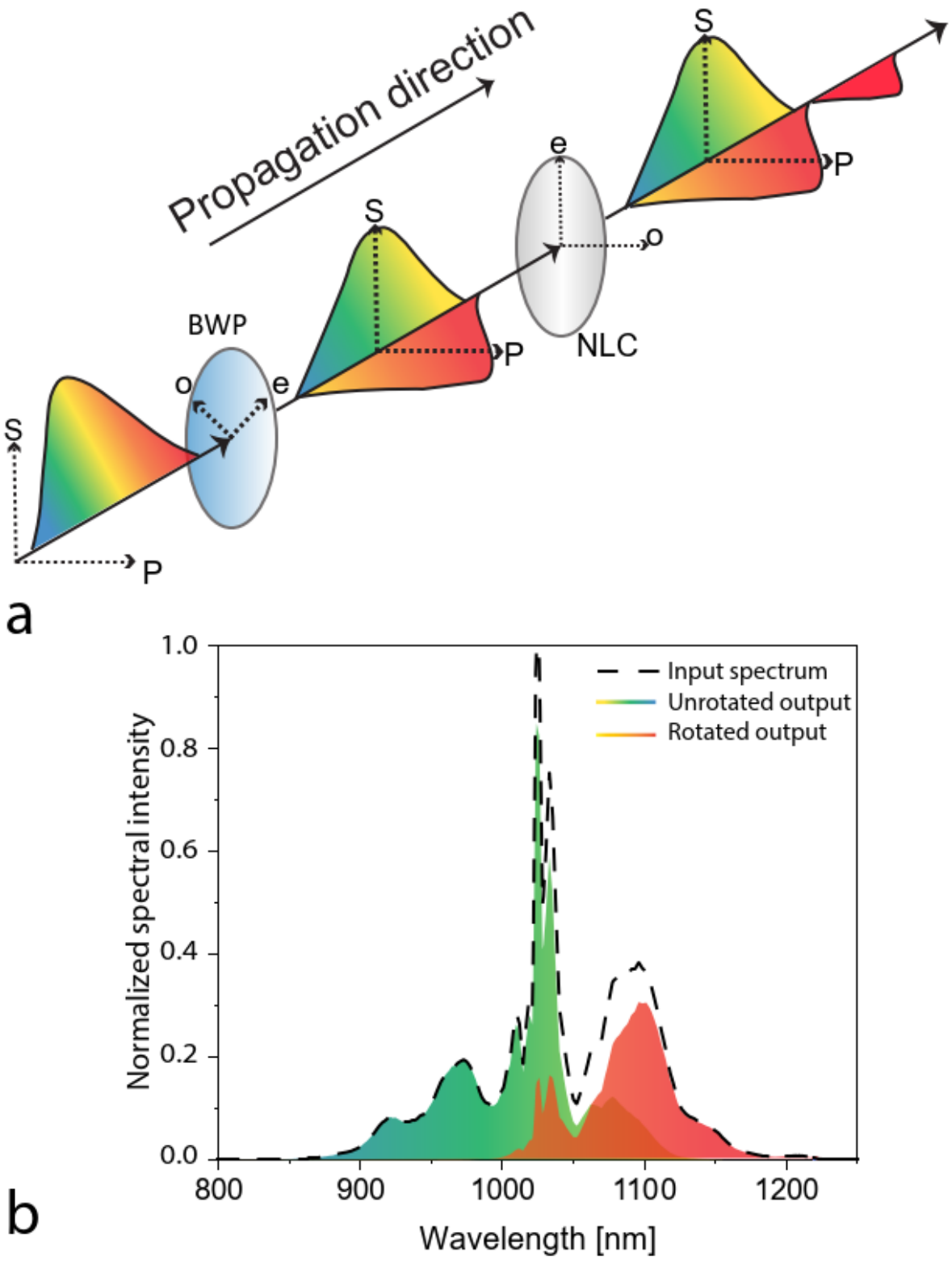

Figure 4.7: (a) Polarization distribution and evolution of the spectra upon propagation through the crystal, with respect to the ordinary (o) and extraordinary (e) optical axes of the crystal. The colors represent the spectral distributions on the axes (and not temporal information). (b) shows the intensity spectra (colored) measured after the BWP on the two polarization axes and the input spectrum (dashed line).

4.2.2 Ultra-broadband near-infrared/mid-infrared beamsplitter

In order to separate the generated mid-IR light from the driving pulses, an ultra-broadband beam splitter was designed and manufactured in-house [2] (see Fig. 4.2, ZnSe) [4]. The beam splitter deposited on a 2-mm thick ZnSe substrate consists of ZnS and YbF3 layers. The back side of the substrate was coated with a ZnS / YbF3 antireflection coating. Its front side, while transmissive in the mid-IR range (see transmission curve in blue shown in Fig. 4.8, left), is highly reflective (spectral average of 90%) for the near-IR spectrum (see the red curve in Fig. 4.8, right). The turquoise and black curves show the targeted mid-infrared transmission and near-infrared reflectance of the beamsplitter, respectively.

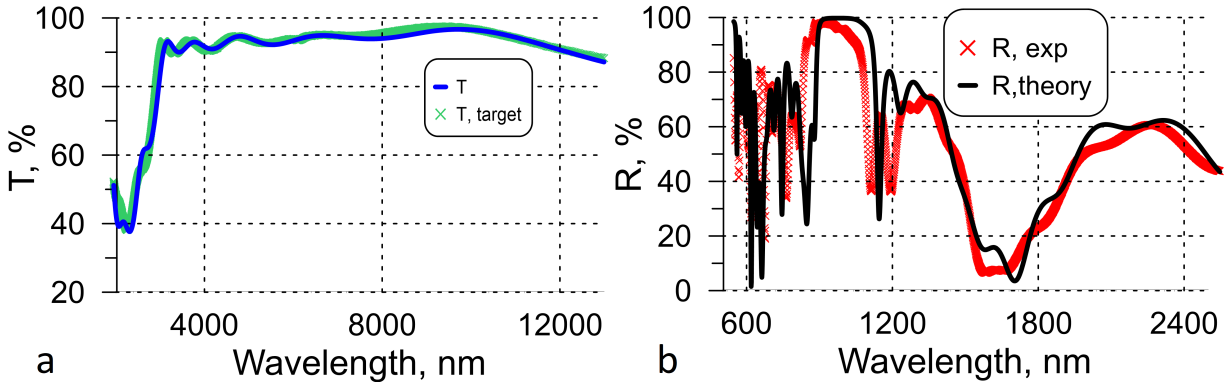

Figure 4.8: Comparison of theoretical and experimental transmittance in the MIR range (left) and theoretical and measured reflectance in the NIR range (right) of NIR/MIR beam splitter.

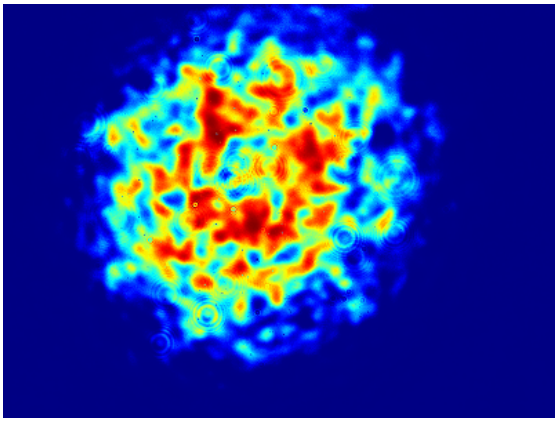

Figure 4.9: NIR beam reflected from BS, shows a strongly spatially-distorted profile.

Despite the high reflectance that the beam splitter provides, it is not possible to reuse the

[2] NIR/MIR beam splitter, produced in-house by Tatiana Amotchkina et al..

near-infrared pulses, after the frequency down-conversion process (IPDfG) due to the strongly spatially distorted beam after its reflection from the beam splitter (see Fig. 4.9).

4.2.3 Single-crystal IPDFG: LGS

Among commercially available crystals, we identified lithium gallium sulfide/$LiGaS_2$ (LGS) as the most suitable for power-scalable difference frequency generation (DFG) driven by the NIR source discussed in the previous chapter, because LGS has a very high damage threshold that could reach a peak intensity of one terawatt per square centimeter. Moreover, it offers a wide transparency range of up to 12 µm [110], making it a good candidate for the generation of broadband MIR radiation.
LGS is a noncentrosymmetric biaxial crystal available in two different cuts, xy-cut with a higher nonlinear coefficient ($d_eff \approx 6$ Pm/V) compared to xz-cut LGS crystals, which have a lower value ($d_eff \approx$ -4.6 Pm/V). In our experiments, different thicknesses of LGS crystals cut with xz ($\theta = 48°$, $\phi = 0°$), have been chosen for the type-I phase-matching IPDFG process. The crystals were commercially provided by Ascut UG and Co.KG.
The NIR beam was focused using a spherical mirror with a 900 mm ROC (M7 in Fig. 3.11) to 40 µm ($1/e^2$-intensity radius). The crystal was placed at a near-IR beam radius of 0.87 mm, which corresponds to a peak intensity of 100 GW/cm^2, which is almost an order of magnitude below the intensity damage threshold reported in [110]. This provides long-term stability of the MIR power.
The crystal is oriented with its e-axis along the polarization direction of the higher-frequency components of the near-IR light, whereas the o-axis of the crystal was parallel to the polarization direction of the lower-frequency components of the near-IR light and was turned by 90° with the help of the BWP (placed between the focusing mirror M7 and the LGS) for type I (e-oo) phase matching [3].
The LGS crystal was tilted to extend the high-frequency cut-off as much as possible. In addition to the phase-matching-angle tuning of the crystal, the dispersion of the NIR beam was also tuned to achieve the broadest MIR spectrum.
LGS crystals with 200 µm and 400 µm thicknesses have been tested, and the generated spectra, measured with a Fourier transform infrared (FTIR) spectrometer, are shown in Fig. 4.10 in blue and black curves, respectively. The corresponding MIR net power given in the legend is the actual value measured by the power meter. By accounting for the transmission and reflection properties of all optics used between the LGS crystals and the position of the IR power measurement, we estimated an average output power directly after the crystals of 90 and 120 mW, respectively, for the 200 and 400 µm thick crystals. Figure 4.10 also illustrates in red line numerical simulation results for the IPDFG process for the LGS crystal thickness of 200µm. The simulation [4] shows great agreement between the experiment (blue line) and the simulation (red line).

[3] In Type I phase matching, the two fundamental beams in, for example, different frequency generation, exhibit distinct polarization directions. In contrast, Type II phase matching involves the two fundamental beams having identical polarization, which is perpendicular to that of the difference-frequency wave.

[4] is performed by Dr. Nick Karpowicz using his open-source simulation tool "Lightwave Explorer" [72]

We should mention that the dense oscillation lines around the wavelength range 5.5-7.5 µm are caused by water vapor absorption in the air. However, in the blue curve, one sees that the oscillations are covering the entire generated spectral range, which is attributed to the interference between the MIR-generated light and its back reflection from the crystal surface. The sharp peaks that appear around 12 and 12.5 µm in the black and blue curves are artifacts of the FTIR measurement device.

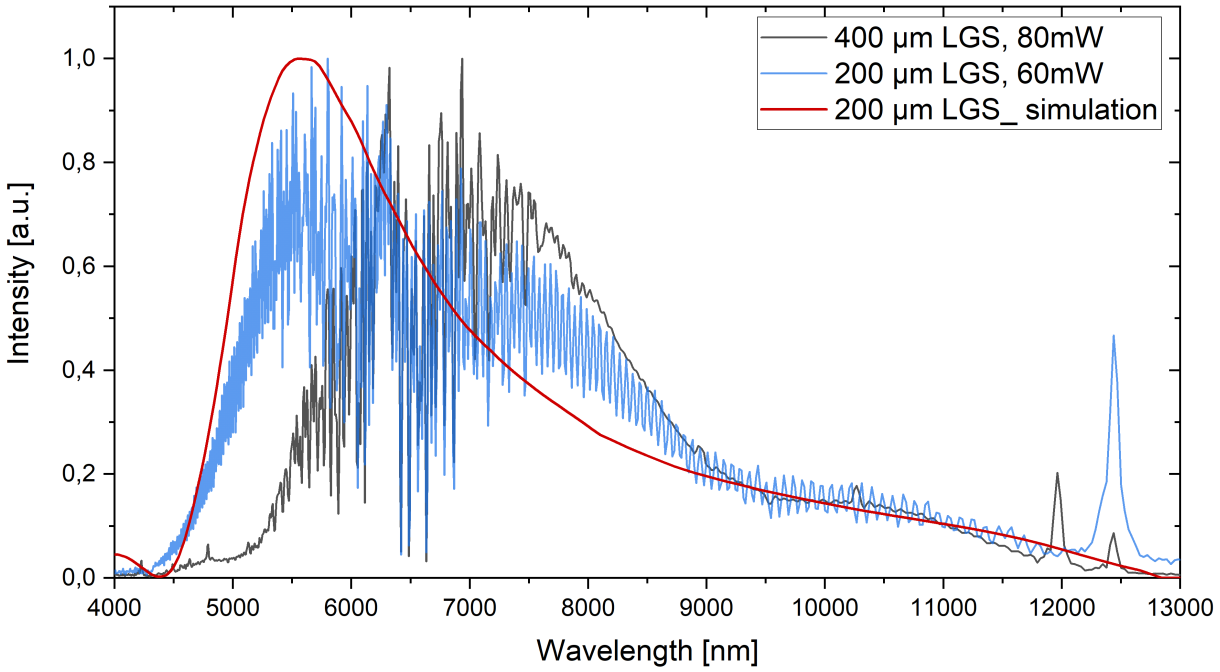

Figure 4.10: IPDFG in LGS for 400-µm (black) and 200-µm (blue) thickness, along with simulation results (red) for 200-µm thickness, "Lightwave Explorer" [72].

4.2.4 Single-crystal IPDFG: LiIO3

Although the main goal of the work was to increase the frequency cut-off and cover as much as possible of the molecular fingerprint region while having a bright light source, achieving those goals with a single LGS crystal seemed not possible given the available NIR spectrum. Therefore, we have tested the possibility of utilizing multiple (two) nonlinear crystals after each other.

We have chosen an LIO crystal to cover the high-frequency MIR range, with wavelengths below 5.5 µm. The protection-coated crystal was oriented with its e-axis along the polarization direction of the blue part of the near-IR light after the BWP and was tilted to extend the high-frequency cutoff as far as possible. The angles for type I (e-o-o) phase-matched IPDFG were ϕ= 0° and θ= 20°. The crystal was placed first at the same place where the LGS crystal was placed and has been systematically shifted toward the

focus; the damage threshold was experimentally determined to be at a peak intensity of > 76 GW/cm^2, and equivalent to a near-infrared beam radius of below 0.8 mm.
Two different thicknesses, 300 and 400 µm, have been tested and the generated spectrum, measured with a Fourier transform infrared spectrometer is shown in Fig. 4.11. The corresponding IR power measurement for each thickness is given in the legend, 12 mW and 20 mW, respectively. By accounting for the transmission and reflection properties of all optics used between the LIO crystal and the position of the IR power measurement, we estimated an average output power directly after the crystals of 18 and 30 mW, respectively.

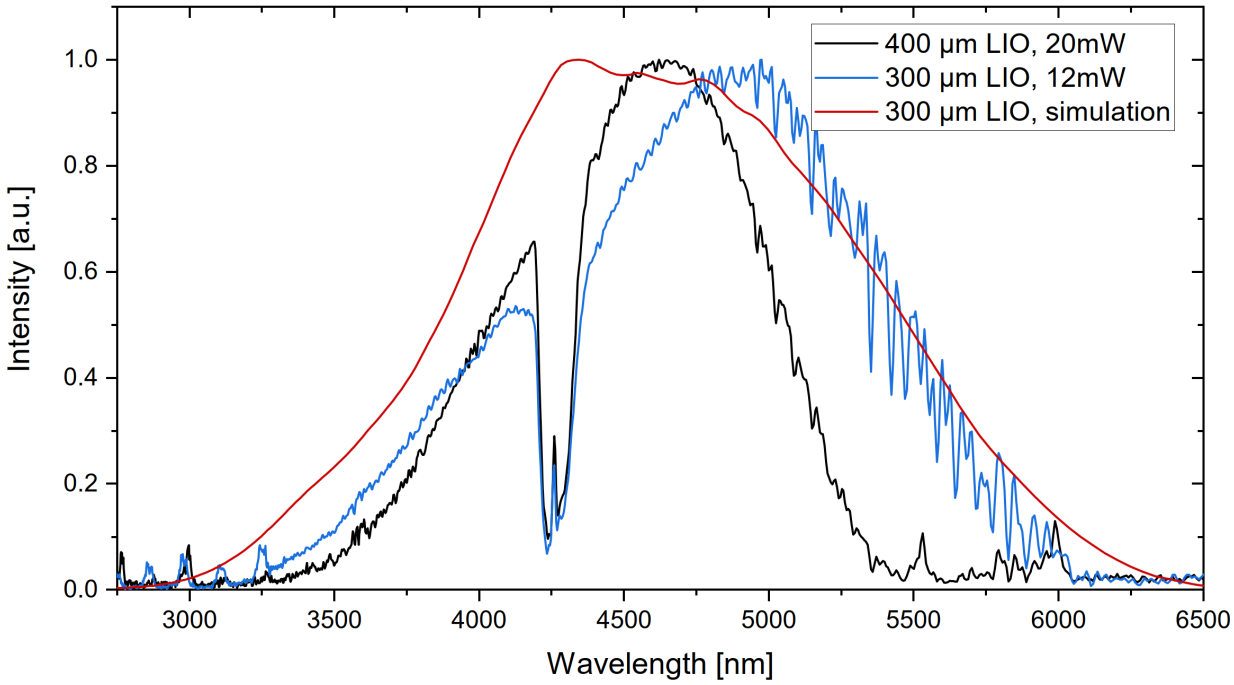

Figure 4.11: IPDFG in LiIO3 for 400-µm (black) and 300-µm (blue) thickness, along with simulation results (red) for 300-µm thickness, "Lightwave Explorer" [72].

4.2.5 Tandem-configuration IPDFG

When driven with 10-fs-scale near-IR pulses, the second-order parametric process of IPDFG [11, 64] (also known as 'optical rectification') can, in principle, result in coverage of the entire IR molecular fingerprint region. In addition, if higher-order (cascaded) nonlinearities are negligible, the waveforms obtained by IPDFG exhibit outstanding passive optical phase stability [66], because the nonlinear polarization responsible for the emitted IR electric field follows the cycle-averaged intensity envelope of the driving pulse [141]. Its conceptual simplicity, together with excellent temporal coherence, makes IPDFG-based IR sources highly promising candidates for unifying properties (i)-(iv)

listed in 4.1, in particular in the context of modern, high-power, compact near-IR femtosecond lasers [12, 20, 26, 30, 41, 48, 77, 109, 110, 128, 138, 150].
In the following, we demonstrate how using the train of nonlinearly compressed pulses described in the previous chapter in an in-line multicrystal arrangement fulfills this promise.
IPDFG was driven in two different crystals, LiIO3 (LIO) and $LiGaS_2$ (LGS). To maximize conversion efficiency while reaching broad spectral coverage, type I phase matching was used for both crystals. Rotating the polarization of the lower-frequency part of the driving spectrum (signal) with respect to the high-frequency part (pump) utilizing the bichromatic waveplate (BWP), which was introduced previously in section 4.2.1.

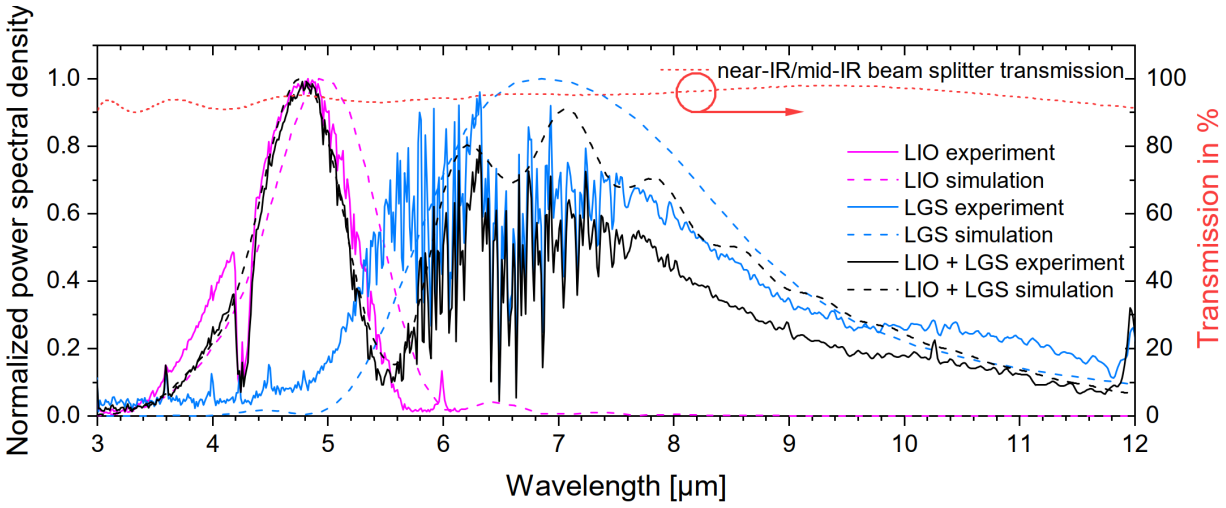

Figure 4.12: Transmission of the NIR/MIR beam splitter (red, dashed line, right y-axis), and experimental spectra (continuous lines, measured with an FTIR spectrometer and normalized to their respective maxima), for LIO and LGS individually, as well as for their in-line sequence. Dashed lines: results of numerical simulations for all configurations.

Following the BWP, a 400-µm-thick LIO crystal was used to cover the high-frequency mid-IR range, with wavenumbers greater than 1850 $cm^{-}1$, where LIO, being an oxide, becomes opaque. The protection-coated crystal was oriented with its e-axis along the polarization direction of the higher frequency components of the near-IR light after the BWP and was tilted to extend the high-frequency cut-off as far as possible. The angles for the phase-matched type I IPDFG (e-oo) were $\phi = 0°$ and $\theta = 20°$.
The experimental determination of the damage threshold involved a systematic adjustment of LIO crystals toward the focal point. The results showed that the peak intensity at which damage occurred was approximately 76 GW/cm^2, and this intensity was reached when using a near-infrared beam radius of 0.8 mm (excluding the BWP). For the IPDFG experiments, the crystal was placed behind the focus, with an estimated peak intensity of 10% lower than the damage threshold.
In order to separate the generated IR light from the driving pulses, an ultra-broadband beam splitter is used which was introduced in 4.2.2. We used a sequence of three such

optics to suppress the unconverted near-IR power, followed by an additional 3-mm Ge plate, anti-reflection coated for the range between 3 µm and 12 µm.
By accounting for the transmission and reflection properties of all optics used between the LIO crystal and the position of the IR power measurement, we estimated an average output power directly after the crystal of 30 mW. The generated spectrum, measured with a Fourier transform infrared spectrometer (FTIR), is shown in Fig. 4.12 (magenta, continuous line).
In analogy to IPDFG driven in LIO, in a second experiment, IPDFG was driven in an uncoated 300 µm LGS crystal, cut in the x-z plane, and set up for type I phase matching with $\phi = 0°$ and $\theta = 48°$. The crystal was placed at a near-IR beam radius of 0.87 mm, corresponding to a peak intensity of 56 GW/cm^2 (without the BWP), and was tilted to favor phase matching for lower mid-IR frequencies. The output power behind the LGS crystal was 102 mW. The power spectral density is shown in Fig. 4.12 (blue, continuous line).
Placing both crystals collinearly (first LIO, second LGS) resulted in continuous spectral coverage of more than 2 octaves (Fig. 4.12, black, continuous line). The total average power after the second crystal with the BWP in place was determined to be approximately 130 mW, compared to 35 mW without the BWP. The broadband IR beam was collimated by an unprotected gold-coated off-axis parabola (OAP) to a diameter of 6 mm, with the intensity profile of the beam shown in Fig. 4.14.

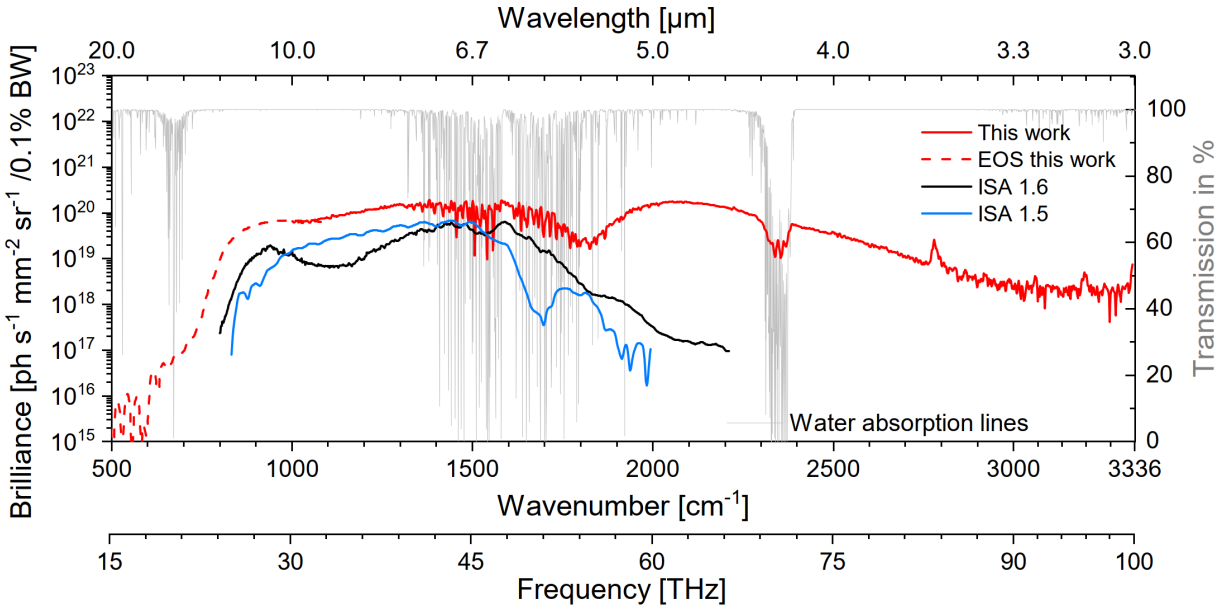

Figure 4.13: Brilliance comparison of our source (red) with other two 1-µm-driven IPDFG-based coherent mid-IR sources developed in our lab.

Figure 4.13 compares the brilliance of our IR source with the state-of-the-art 1-µm-driven IPDFG sources developed in our laboratories. Infra-sampler instrument generation 1.6 (ISA 1.6) was driven with the same NIR pulses of this work and 750 µm LGS crystal, on

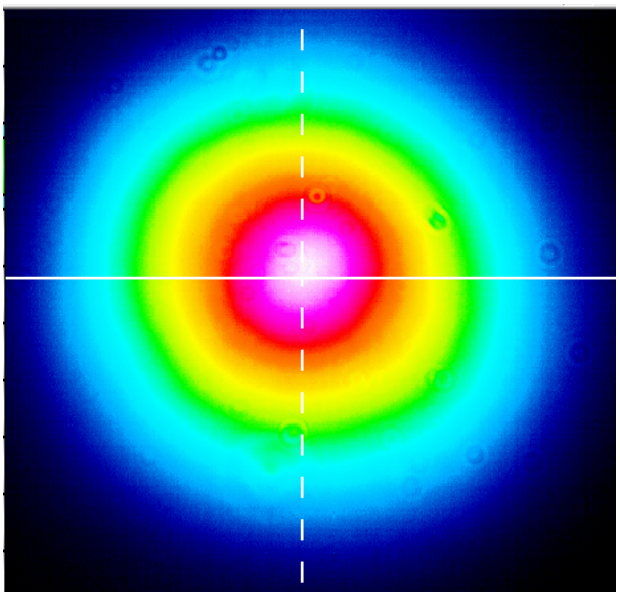

Figure 4.14: MIR beam profile with diameter of 6 mm.

the other hand, Infrasampler instrument generation 1.5 (ISA 1.5) is driven with slightly longer NIR pulse duration (16 fs) and IPDFG process is pursued utilizing 1 mm thick LGS crystal. Gray lines (and right y-axis): transmission through 1 m of laboratory air [1], approximating the mid-IR beam path in our setup from generation to detection.
Figure 4.15 compares the brilliance of our IR source with the state of the art of 1-µm-driven IPDFG sources, as well as with a third generation IR synchrotron beamline and widely used thermal sources [111]. The numbers [1 to 6] given in Fig. 4.15 correspond to the following references, respectively: [110, 20, 12, 150, 32, 19].
Table 4.1 summarizes the most important experimental parameters, in the context of state-of-the-art 1-µm-driven IPDFG sources which correspond to Fig. 4.15.
Figure 4.16 shows a photograph of the IPDFG-tandem setup, in which one sees the way the crystals have been placed in an inline geometry after each other. (a) Shows the direction from which the NIR beam comes, passing through the BWP and then the LIO and LGS crystals before it gets separated from the generated MIR radiation utilizing the MIR/NIR beam splitter. The NIR bean is reflected by the BS and then directed toward the beam dump with the help of turning mirrors, whereas the MIR beam is turned by 90° OAP. A zoomed-in view of the dual crystal assembly is shown in (b).

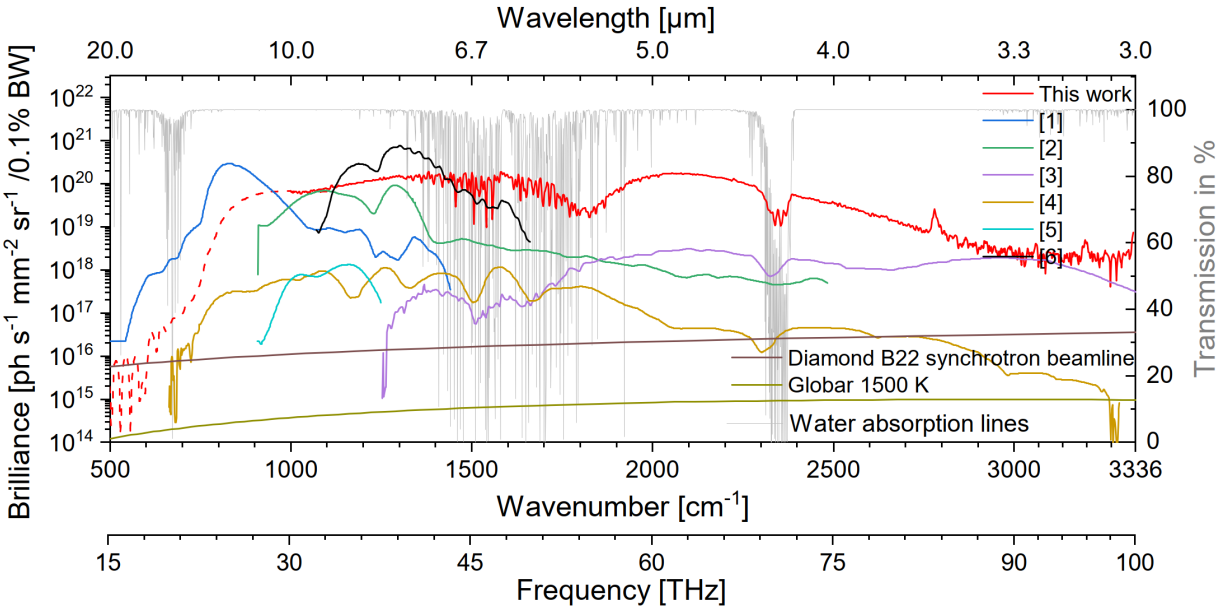

Figure 4.15: Brilliance comparison of our source (red) with a representative selection of 1-µm-driven IPDFG-based coherent mid-IR sources. Grey lines (and right y-axis): transmission through 1 m of laboratory air [1], approximating the mid-IR beam path in our setup from generation to detection. The brilliance curve for our experiment is stitched from two measurements: via FTIR spectrometer (continuous, red line) above 1000 cm^{-1} (limited by the detector at smaller wavenumbers) and via EOS (dashed, red line) below 1000 cm^{-1}. EOS provides a broader detectivity range toward smaller wavenumbers (see instrument response function in Fig. 5.6. The EOS curve was stitched to the FTIR curve in the 500-to-1000-cm^{-1} range, where the spectral shapes match.

NIR peak intensity	Nonlinear crystal	IPDFG spectral span [µm] (at -30 dB)	Mid-IR power [mW]	Power conversion efficiency [%]	Reference
76, 54	LIO and LGS	3.4-15	130	0.147	This thesis
350	LGS	6.7-18	103	0.2	[110]
150	LGS	5-11	31.8	0.16	[20]
130	LGS	8-11	0.37	0.04	[12]
250	LIO	2.5-8	1.1	0.003	[150]
90	ZnS	3-15	0.8	0.02	[32]
140,300	LGS and LGS	6-9	160	2	[19]

Table 4.1: Parameters of state-of-the-art 1-µm-driven IPDFG sources which correspond to Fig. 4.15.

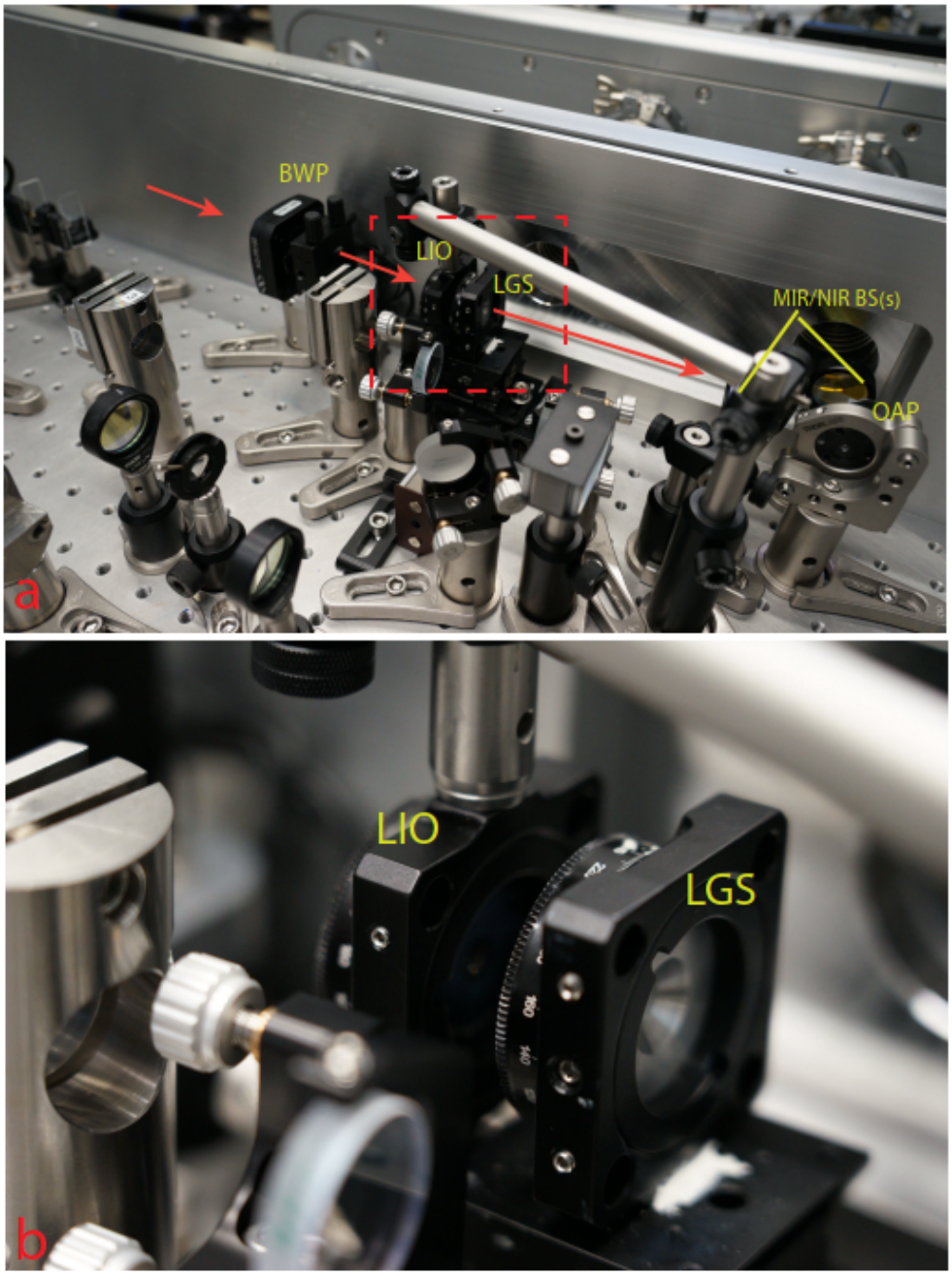

Figure 4.16: Photograph of the IPDFG-Tandem setup, showing the way the crystals have been placed in an inline geometry after each other. (a) Shows the direction from which the NIR beam comes, passing through the BWP and then the LIO and LGS crystals before it gets separated from the generated MIR radiation utilizing the MIR/NIR beam splitter. The NIR bean is reflected by the BS and then directed toward the beam dump with the help of turning mirrors, whereas the MIR beam is turned by 90° OAP. (b) Illustrates a zoomed-in view of the dual crystal assembly.

Chapter 5

Multi-octave electric-field sampling

5.1 Introduction

In the previous chapter, the generation of MIR pulses via intra-pulse difference frequency generation (IPDFG) was discussed and demonstrated. By employing IPDFG to create stable waveforms within the mid-infrared (MIR) spectral range and electro-optic sampling (EOS) [84, 125] for pulse characterization, we can explore a broad range of dynamics in both solids [65, 79, 120] and molecules [77, 109].

In addition to the simplicity and compactness of IPDFG, one highly attractive feature is its passive optical-phase stability [64]. However, for a free-running femtosecond frontend – that is, without stabilization of the optical phase of the pulse train that drives IPDFG, the resulting mid-IR radiation only exhibits passive phase stability if there is no additional process mixing the optical phase of the driving pulses into the mid-IR field. For example, this condition is not fulfilled when cascading nonlinear processes are involved [128, 149].

Due to the optical-phase stability of the waveform, the driving pulse envelope can serve as a temporal reference for precision measurements without the need for repetition rate stabilization. EOS utilizes ultra-short laser pulses and second-order perturbative nonlinear processes to sample sub-optical-cycle portions of the electric field of light. It can be best described as a two-step process [49]: (1) nonlinear up or down conversion represented by sum-frequency generation and or difference-frequency generation (or both) between the NIR pulse (gate) and the MIR pulse (signal), (2) heterodyne detection. The sum and difference frequency components are polarized perpendicular to the gate pulse, altering the polarization state in their spectral overlap region [130]. This change is detected using an ellipsometry setup, resulting in an EOS signal.

In the following, we discuss the numerical and experimental verification of the optical-phase stability of the polarization-tailored multi-crystal IPDFG source to get as close as possible to the real electric field of the mid-infrared (MIR) pulses.

5.2 Experimental results

To validate MIR waveform stability, we implemented an EOS setup [82, 84, 136, 145]. Figure 5.1 shows the schematic of the electro-optic sampling setup. We used a copy of the near-IR driving pulse as the gate pulse, reflectively attenuated to an average power of 94 mW at the EOS crystal, in order to avoid optical damage to the EOS crystal. The broadband MIR beam (signal) was collimated by an unprotected gold-coated off-axis parabola (OAP) to a diameter of 6 mm, with the intensity profile of the beam shown in Fig. 4.14. A second focus is implemented using two identical OAPs to place the chopper wheel, that modulates the MIR beam, or lock-in detection of the EOS signal, before recombination with the gate beam.
For recombination, a 3-mm-thick uncoated Ge plate was used. At an incidence angle of 80° for the incident p-polarized MIR beam and the s-polarized NIR beam, the Ge plate transmitted and reflected the majority of mid-IR and gate beams, respectively. The optical path of the gate was varied using a linear stage with a pathlength of 50 mm, which enables scanning a delay of 100 mm (∼333 ps) due to reflection with a retroreflector (RR in Fig. 5.2). The latter was represented for simplicity by two 45° plane mirrors in Fig. 5.1.
After spatial combination, the collinear beams were focused onto the EOS crystal by an unprotected gold-coated 90° OAP. At focus, beam diameters ($1/e^2$) were 85×120 µm^2 and 115×120 µm^2 for the NIR (gate) and MIR (signal) beams, respectively. Figure 5.3 shows the MIR and NIR beams in their collimated state, right before the OAP. MIR and NIR beams at the focus (where the EOS crystal will be placed) are illustrated in a and b, respectively. The utilized Nanoscan camera is a slit scanning device, which is a highly reflective metal-scanning disk. Therefore, part of the light is reflected to the OAP, where it clips before it gets focused on the camera again, causing the distortion present in c and d.
Capturing the entire bandwidth of the generated mid-IR field at once requires an ultra-broadband EOS setup. To this end, as well as to record an EOS signal closely resembling the optical electric field, we opted for a 3-µm-thin GaSe crystal optically contacted on a 500-µm-thick CVD (chemical vapor deposition) diamond plate [75]. This assembly combines the advantages of an ultra-broadband instrument response with the suppression of multiple reflections (echo effect) inside the EOS crystal.
Following the GaSe-crystal-on-diamond assembly, the EOS detection consisted of a Wollaston prism, a short-pass filter with a cut-off wavelength of 950 nm, and an electronically-balanced detector with two Si photodiodes. A lock-in amplifier was used to suppress background noise and amplify the signal at 6 kHz, which corresponds to the chopping frequency of the MIR beam.
A photograph of the electro-optic sampling setup is shown in Fig. 5.2, in which an additional optical element, a red-circle-marked 1" gold mirror, is placed behind the RR. The latter is not part of the EOS optical path, but it belongs to the stage delay tracking system. The latter additionally consists of the "Smaract PICOSCALE" device provided with a continuous-wave laser diode of wavelength 1550 nm. The laser light comes from a

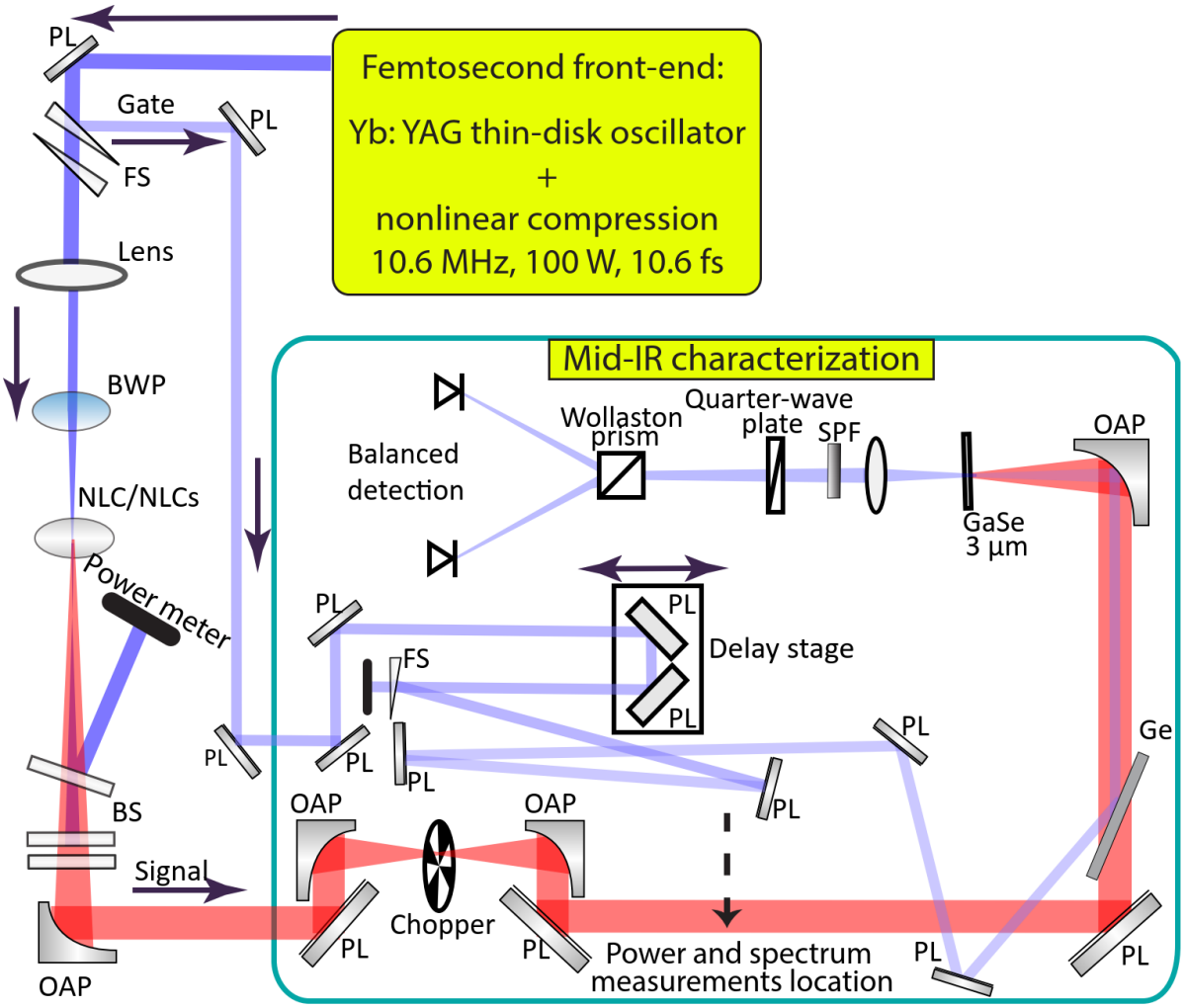

Figure 5.1: Schematic of the experimental setup. PL: plane mirror, OAP: off-axis parabola, FS: fused silica, NLC/NLCs: nonlinear crystal(s), BWP: bichromatic waveplate, Ge: germanium, SPF: short-pass filter. A 3-mm-thick Ge plate was used as a beam combiner for the mid-IR and the near-IR gate beam. At the angle of incidence of 80° for the incident p-polarized mid-IR beam and for the s-polarized near-IR beam. The Ge plate transmitted and reflected the majority of the mid-IR and gate beam power, respectively.

fiber feedthrough that can be easily attached to an optical fiber supplied with an interferometric head. The laser light illuminates the aforementioned mirror, which is aligned in such a way as to reflect the light straightly to the interferometer block, that is combined in the fiber head. The recorded information is then detected by the "Smaract PICOSCALE" and, based on the interference patterns, the latter can provide precise information about the exact location on the linear stage at a specific point in time.
The initial focus during the optimization of EOS detection was on spectral bandwidth and dynamic range, which entails the reduction of detection noise. Figure 5.4 compares

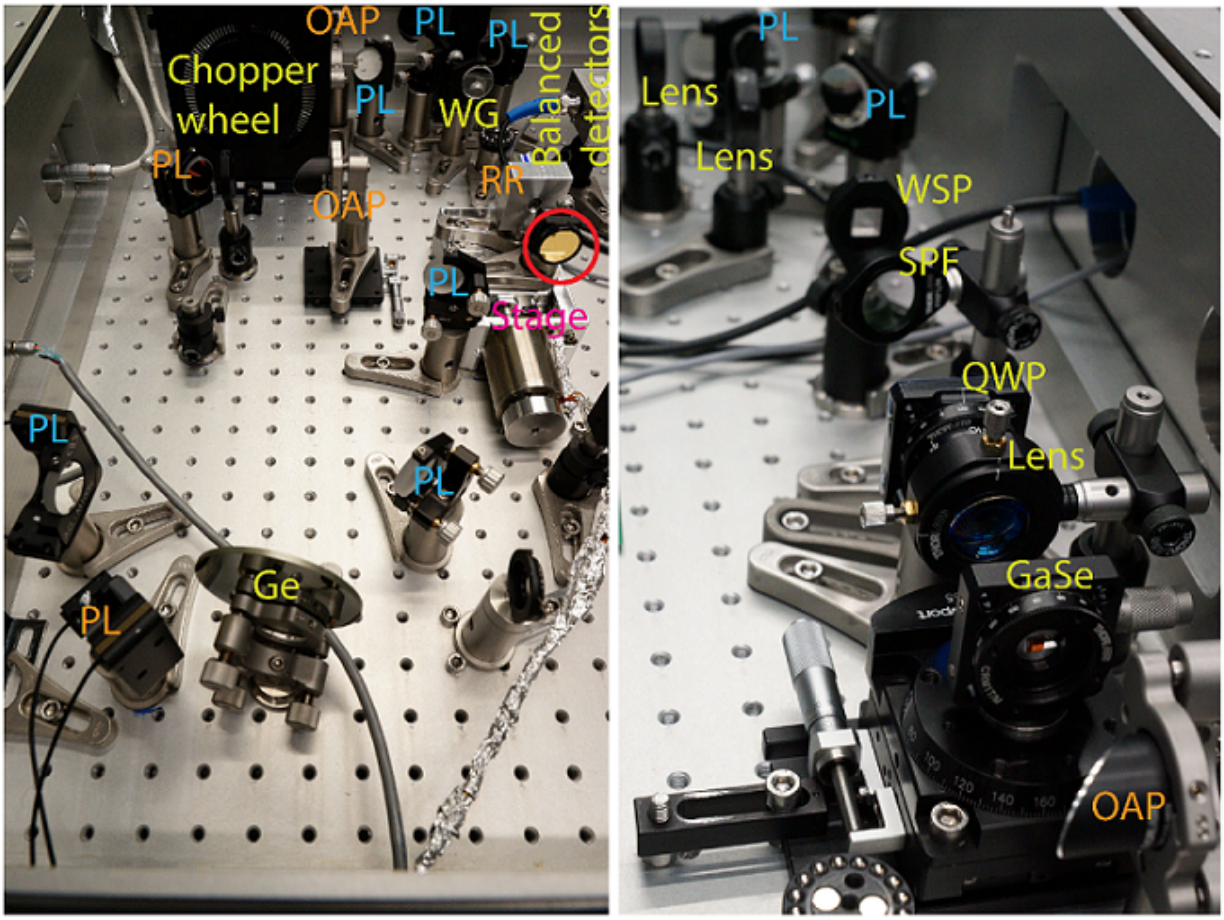

Figure 5.2: Photograph of the Electro-optic sampling setup. The figure shows all the main optical and mechanical components built in the EOS. PL: plane mirror, the blue-labeled plane mirrors are the silver-coated ones that are used for the NIR beam (gate) as well as the newly generated frequencies via the nonlinear upconversion process in the GaSe crystal, whereas the orange-labeled ones are the unprotected gold-coated mirrors. WG: uncoated wedge, OAP: 90° off-axis parabola, QWP: quarter waveplate, SPF: short pass filter, WSP: Wollaston prism, RR: retro-reflector, and the plane gold mirror placed behind it on the linear stage belong to the stage delay tracking. The beam pass is identical to the one shown in the schematic figure 5.1.

different spectra obtained utilizing EOS measurements for different IPDFG configurations. Each spectrum is plotted together with its detection noise in the same color. The latter is obtained by calculating the root mean squared value of the average data of all recorded noise traces for these specific measurement conditions: gate power, chopping frequency, and measurement time.
In the beginning, a GaSe crystal with a thickness of 50 µm is used, to sample the IPDFG results of a tandem configuration (LIO of 300 µm thickness and LGS of 500 µm thickness). The results show oscillations over the entire spectral coverage (gray dashed

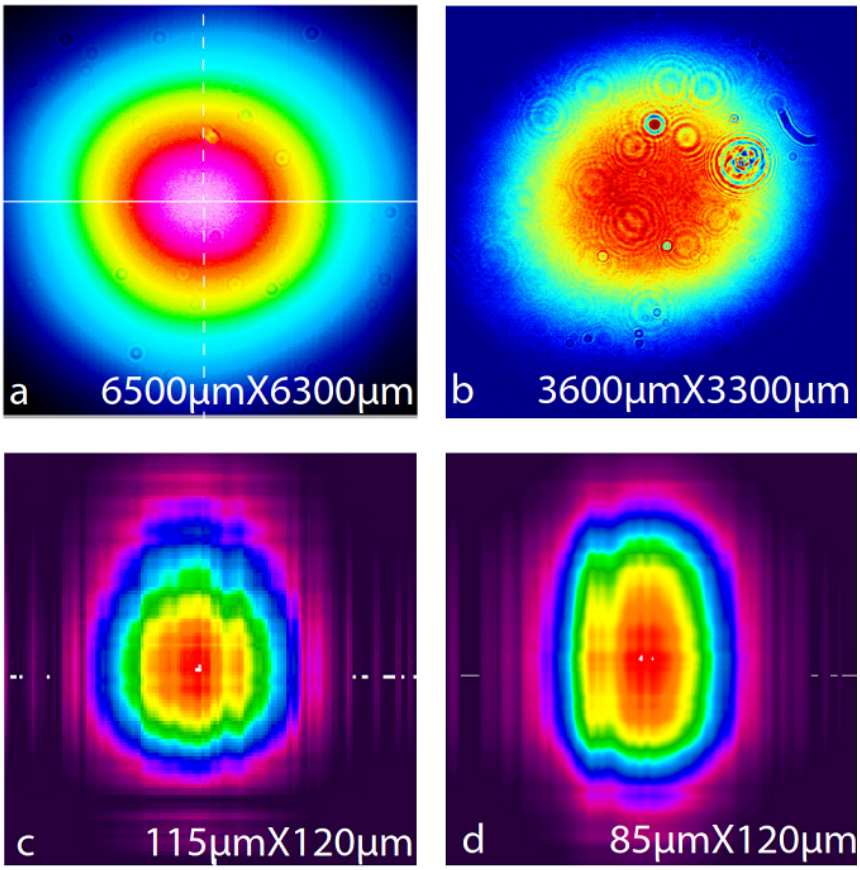

Figure 5.3: MIR and NIR beams collimated and focused at EOS crystal location. Respectively in a and b, we see the collimated MIR and NIR beam profiles before the OAP and at the foci after the OAP in c and d.

line, in Fig. 5.4), and the detection bandwidth is limited and narrower compared to the results of the 3 µm thick GaSe. For these reasons, additional EOS measurements were performed using a GaSe crystal with 3 µm thickness. One should mention that these measurements were done without taking noise scans, and for this reason, the detection noise of these measurements is not shown.

Further EOS measurements were recorded utilizing the ultra-thin GaSe (3 µm thick). For each measurement, 40 individual scans have been recorded with a measurement time of 4.5 seconds per scan. Single-crystal IPDFG results show a higher dynamic range compared to dual-crystal IPDFG, of $\sim 1\text{x}10^6$ (red line) and $\sim 3\text{x}10^5$ (blue line), for LIO and LGS, respectively. The dual-crystal IPDFG results are given in (the green line) and have shown a noticeable increase in the detection noise compared to the single-crystal case. The dynamic range of the latter case is $\sim 2\text{x}10^4$.

Figure 5.5 shows the EOS measurements of the three configurations: LIO only (a), LGS only (b), and LIO followed by LGS (c). The measurements presented in panel c were conducted on a different day from those in panels a and b. It should be noted that the

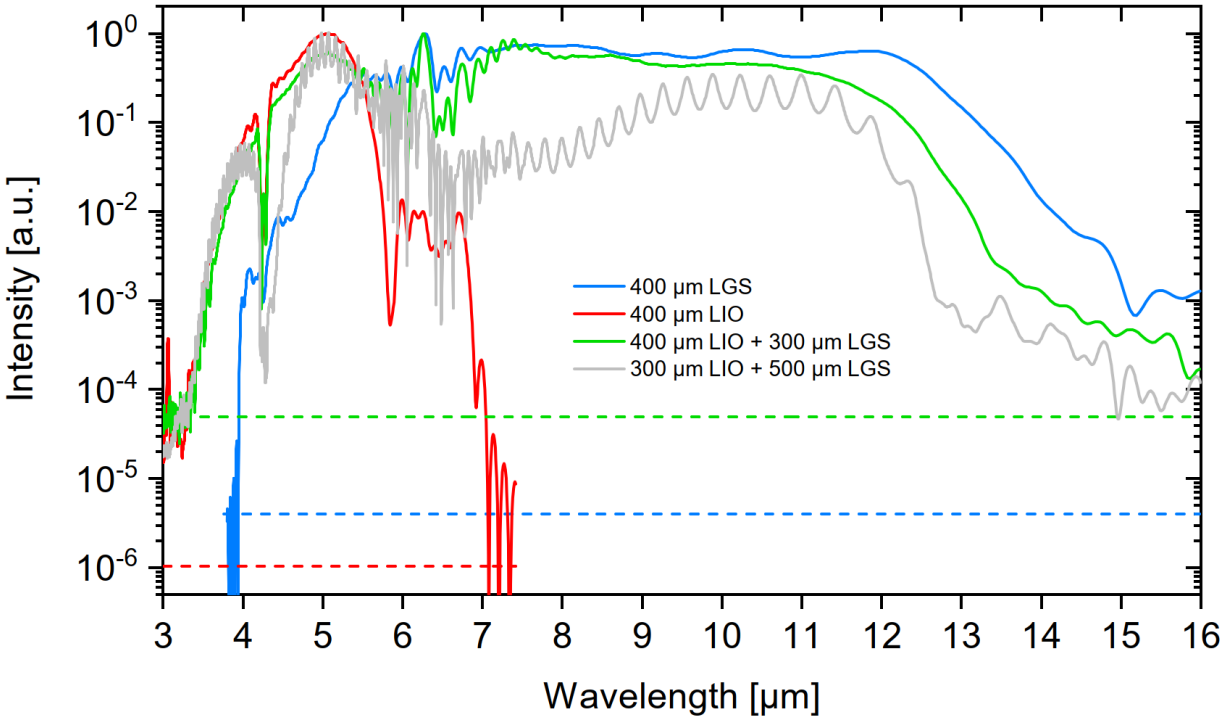

Figure 5.4: Spectral EOS results of different IPDFG configuration. Single crystal IPDFG done using LIO is given in red, Single crystal IPDFG done using LGS is given in blue, and dual crystals IPDfG is given in green and grey, where 3 µm GaSe and 50 µm Gase is used, respectively. Each spectrum is shown together with the measured detection noise floor in the same colored dashed line.

laser system had slightly worse noise performance during these measurements. Each configuration is represented by 40 individual scans (shown in gray), with a measurement time of 4.5 seconds per scan. Red lines indicate the average of the recorded scans.

5.3 Numerical simulation

To build a theoretical understanding of the nonlinear processes occurring in the crystals, we modeled these effects numerically employing the nonlinear wave equation in the slowly-evolving wave approximation [72]. We use literature values for the refractive indices and nonlinear coefficients of LGS [102], LIO [99], and GaSe [51, 115], which account for second and third order nonlinearities. The system was solved on a uniform three-dimensional grid (two spatial dimensions, plus time) and was numerically propagated in space through the optical system.
In the full simulation [1], the electric field of the driving pulse, whose temporal form was determined by a frequency-resolved optical gating measurement and assumed to be

[1]The simulation was done by Dr. Nick Karpowicz[72]

Gaussian in space, propagated nonlinearly through the LIO crystal, propagated through 11 mm of free space, then propagated nonlinearly through the LGS crystal. Finally, the carrier-envelope phase (CEP) and pulse energy of the input pulse were scanned to determine their influence on the noise characteristics of the final IPDFG field. The results for the mid-IR power spectral densities obtained with the numerical simulations are shown with dashed lines in Figure 4.12 for the three configurations (LIO, LGS, LIO followed by LGS). The agreement with the measured spectra validates our numerical model.

The instrument response function calculated with our numerical model, including the nonlinear propagation in the GaSe crystal and the filtered detection of the resulting polarization state of the gate pulse, is shown in Fig. 5.6. It exhibits a flat, broadband spectral response up to 2000 cm^{-1}, and falls off for higher wavenumbers.

In order to numerically verify the optical-phase stability of the generated mid-IR radiation, we repeated simulations with the CEP phase of the near-IR driving pulses varied from 0 to 2π in steps of $\pi/8$ rad and otherwise identical input values. The temporal phase of the resulting mid-IR field varied by less than 1 µrad in the output bandwidth, which is expected to be negligible in applications.

Figure 5.7 presents the simulations performed with near-IR driving pulses with opposing CEP values. The overlap between the EOS curves with different initial CEP values illustrates the expected optical-phase stability of the generated mid-IR field. The statistics of the measured EOS traces exhibit similar values for all cases, confirming the mid-IR waveform stability within our measurement uncertainty.

Figure 5.8 shows the Fourier transform limited of the MIR pulses for three different crystal cases: LIO, LGS, and LIO followed by LGS in the upper, middle, and lowest panels, respectively.

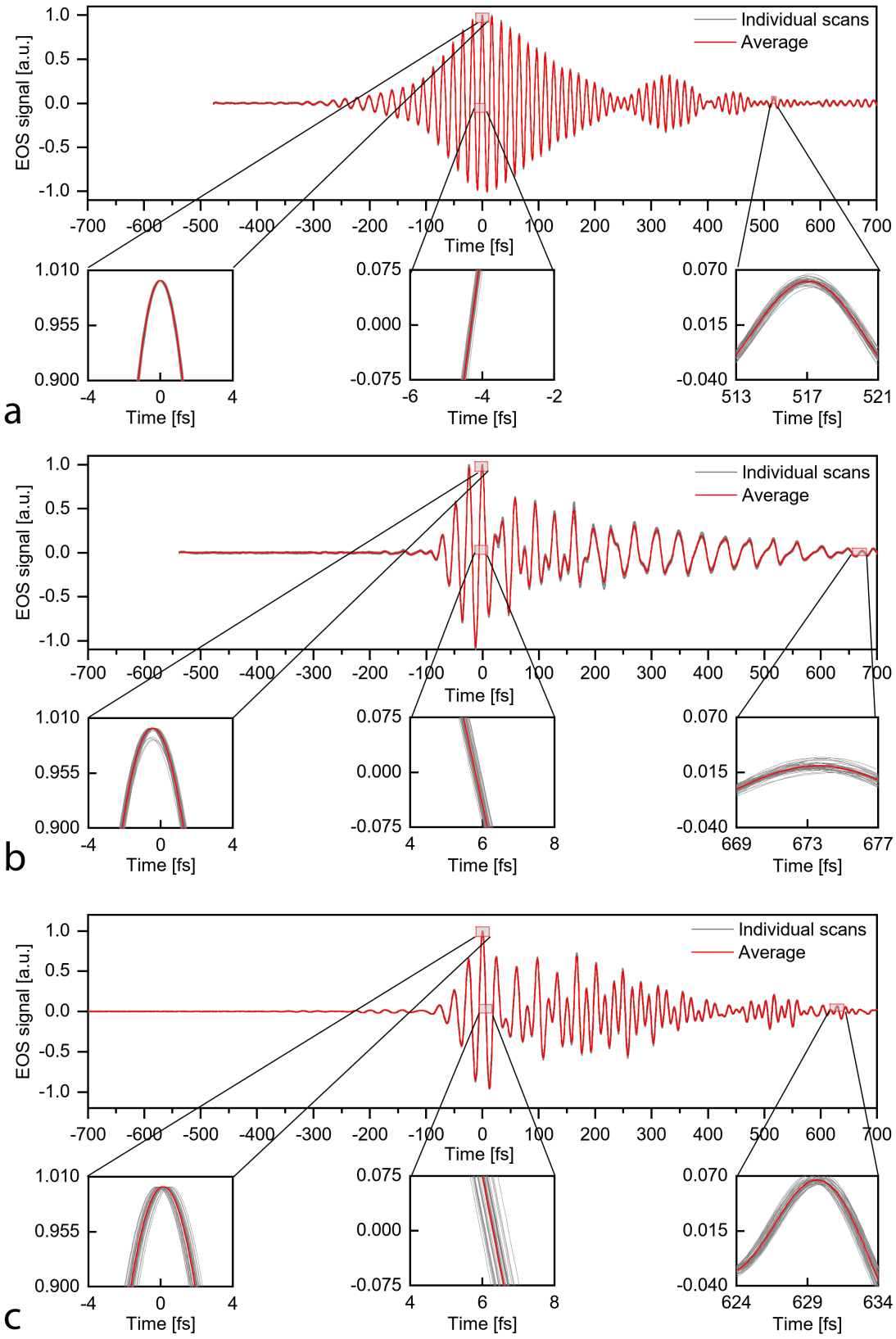

Figure 5.5: Waveform stability. EOS measurements for (a) LIO only, (b) LGS only, and (c) LIO followed by LGS. The measurements shown in panel c have been taken on a different day than those in panels a and b, with a slightly worse noise performance of the laser system. For each configuration, 40 individual scans are shown (grey), with a measurement time of 4.5 seconds per scan. Red lines: average of recorded scans.

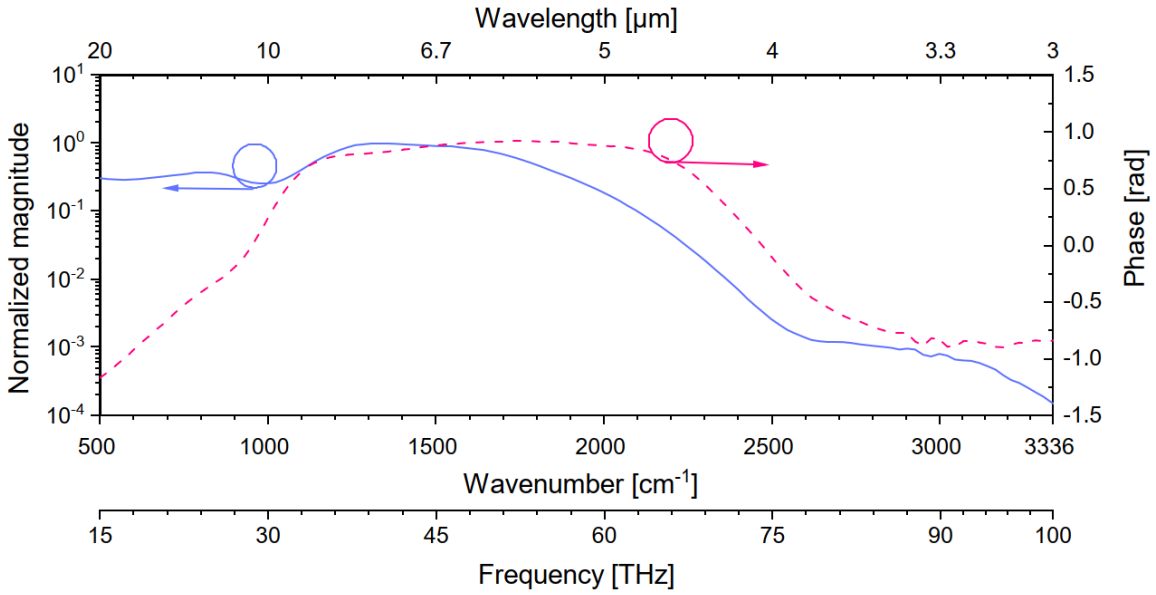

Figure 5.6: The instrument response function calculated with our numerical model. Spectral magnitude (normalized to its maximum, blue, continuous line) and spectral phase (red, dashed line) of the EOS instrument response function. Note that the response in the absorption of GaSe near 500 cm^{-1} is likely to be distorted by features of the complex refractive index not included in the Sellmeier equation used [51, 73, 115].

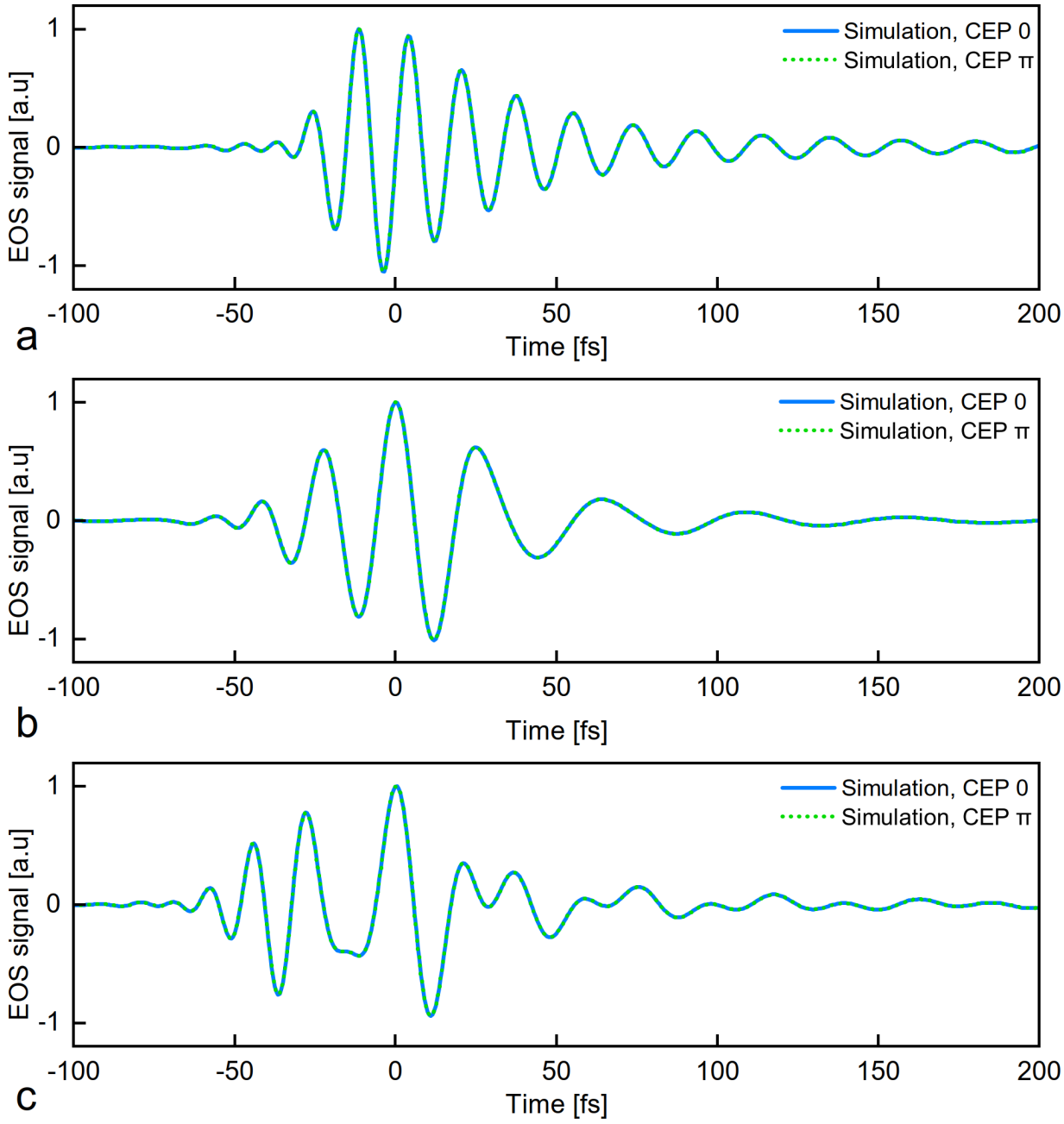

Figure 5.7: Simulated EOS traces for NIR driving pulses having opposing CEP values, illustrating the independence of the waveform obtained via IPDFG thereof. Panels a, b, and c represent LIO, LGS, and LIO + LGS cases, respectively. In the simulations, the propagation through ambient air was omitted, leading to qualitatively different time-domain EOS signal shapes.

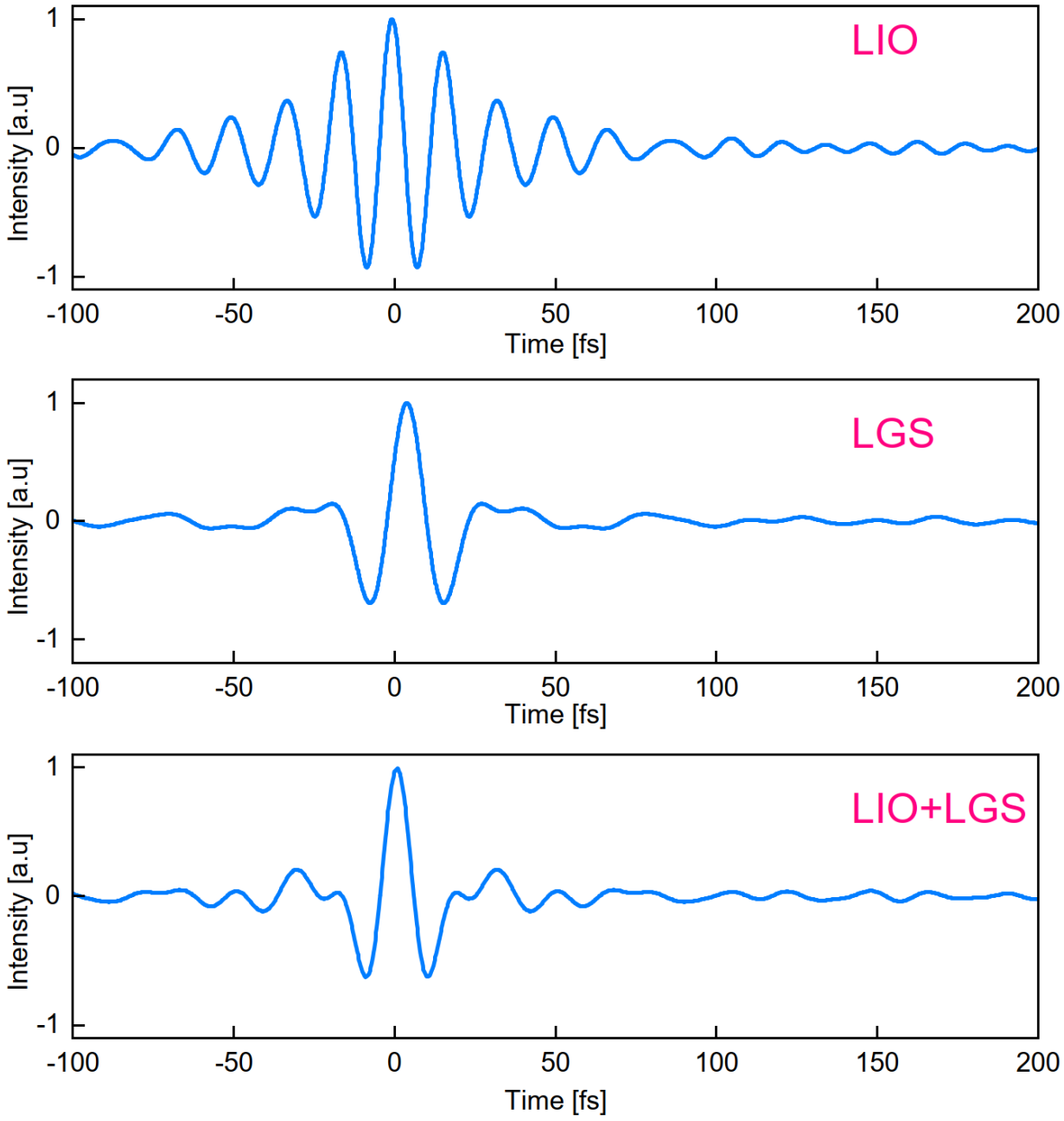

Figure 5.8: The figure presents the Fourier transform limited characteristics of MIR pulses for three different crystal cases: LIO, LGS, and a combination of LIO followed by LGS. These cases are represented in the upper, middle, and lowest panels, respectively.

Chapter 6

Summary and outlook

The results presented in this thesis introduce a femtosecond-laser-based IR radiation source that offers a set of properties highly desirable for broadband spectroscopy in the molecular fingerprint region. To the best of our knowledge, this source combines, for the first time, several key characteristics: It provides broad spectral coverage across the entire molecular fingerprint region while surpassing the brilliance of synchrotron IR beamlines by more than two orders of magnitude and up to a peak of four orders of magnitude. In addition, it exhibits both spatial and temporal coherence. Simultaneously, this femtosecond source maintains a conceptually simple in-line setup.

The front end of the setup consists of a Kerr-lens mode-locked femtosecond oscillator [107] and a multipass-cell spectral broadening technique. This combination, complemented by a distributed quasi waveguide (DQWG) [55], enables the generation of ultrashort pulses with a duration of 10.6 fs and a Fourier transform-limited duration as short as 9.8 fs while maintaining an excellent beam quality (M^2<1.2).

The simultaneous coverage of the entire molecular fingerprint region was made possible by employing intra-pulse difference-frequency generation (IPDFG) driven in two consecutive crystals, thus combining their phasematching bandwidths. We achieved record brilliance values for IPDFG sources driven by 1-µm wavelengths by tailoring the input field's polarization distribution. This opens new possibilities for advanced spectroscopic studies in a wide range of applications [14, 34, 135, 142].

We have verified the source's coherence properties in theory and experiment, the latter employing ultra-broadband electro-optic sampling. In order to develop a theoretical understanding of the nonlinear processes taking place in the crystals, we employed numerical modeling techniques. These effects were modeled using the nonlinear wave equation within the framework of the slowly-evolving wave approximation [72]. This modeling approach facilitated the exploration of various parameters and conditions, providing a deeper understanding of the underlying physics and the factors influencing the nonlinear processes in the crystals.

In addition to its suitability for Fourier-transform spectroscopy, this source is suitable for advanced spectroscopy techniques leveraging its temporal coherence. The spectrum of the high-repetition-rate phase-stable waveforms exhibits a single-parameter frequency

comb nature, which facilitates convenient implementations of various spectroscopy schemes such as ultra-broadband mid-IR frequency comb [89], dual-comb [77, 94, 132], and cavity-enhanced spectroscopy [129] covering the entire molecular fingerprint region. Furthermore, the waveform's stability allows for high-sensitivity field-level detection [20, 26, 27, 48, 59, 75, 77, 90, 100, 109, 110, 128, 149].
The generated mid-IR pulses, with an energy of 12.3 nJ, support a Fourier-transform limit of 13 fs. When temporally compressed, and tightly focused, its field strengths into the multi-MV/cm range come into reach, thus expanding the applicability of this source to nonlinear spectroscopy schemes [58, 120]. The multi-crystal IPDFG arrangement maintains phase stability, which opens up possibilities for synthesizing waveforms [88, 91] with specific shapes. Moreover, extending the coverage to even broader bandwidths seems feasible, particularly towards lower IR frequencies, while ensuring waveform stability.
Building on the results and insights presented in this thesis, several promising directions for further development have emerged. These offer the potential both for performance enhancements of our MIR radiation source, as well as for novel applications in ultrafast IR spectroscopy:

1. Exploring the influence of spectral content and chirp in the NIR driving pulse train on MIR waveform generation:

   In our experimental setup, the spectral content of the NIR driving pulse train and chirp influence the resulting MIR waveforms. Firstly, these waveforms exhibit repeated electric fields that are nearly identical, particularly within the overlapping range of spectra generated by the two crystals. Our findings demonstrate the feasibility of coherent spectral synthesis. Secondly, the spectral content and chirp of the NIR pulse train directly impact the shape of these reproducible waveforms, which can be approximately detected using broadband EOS technology. This suggests a promising avenue for customizing specific waveforms to meet desired requirements. Exploring this phenomenon in greater depth would undoubtedly be of great interest and is recommended as a potential avenue for future research.

2. Improving the stability and reproducibility of the MIR source through active noise suppression and beam stabilization systems:

   It is worth mentioning that the implementation of a few active beam stabilization systems would improve the long-term stability of the output power and the reproducibility of our MIR source. This observation is based on our experience with previous implementations of 1-µm-frontend-based FRS systems [66, 109, 110]. Therefore, the inclusion of at least one beam-pointing stabilizer before the DQWG and another one before the IPDFG would guarantee the preservation of both aforementioned properties over several hours. In addition to the active beam stabilization system, implementing an active intensity noise suppression like the one based on an acousto-optic-modulator (AOM) has been proven in earlier studies to achieve a RIN suppression of the MIR pulse train of up to a factor of 20 in the band between 1 Hz and 100 kHz [62].

3. Optimizing the MIR temporal waveform compression:

   The measured waveform deviates from a Fourier-transform-limited pulse due to the presence of strong absorptions in the molecules that constitute the laboratory atmosphere, as well as the effects of propagation through the 3-mm-ZnSe beam-splitters, the 2-mm Ge beam combiner for EOS, and the EOS response function. By carefully managing these factors, such as implementing nitrogen purging and utilizing MIR dispersive mirrors [5], there is significant potential for achieving temporal compression of the measured waveforms 5.8.

4. Optimizing the NLCs position in order to boost the IPDFG efficiency:

   The order in which the LIO and LGS crystals are placed in the in-line IPDFG is determined by the transparency of the NLCs. The LIO crystal can transmit up to 5µm, while the LGS crystal has broadband transmission. Consequently, the preferred order is LIO followed by LGS.

   However, it is important to note that the LIO crystal has a three times lower damage threshold (DT) compared to the LGS crystal. To ensure efficient IPDFG, where both crystals are placed in the beam at intensities of at most approximately $\sim 10\%$ below their DT, there are three options to consider: (i) Place LIO before the focus and place LGS between LIO and the focus. (ii) Place LIO before the focus and place LGS behind the focus. (iii) Place LIO behind the focus and place LGS behind LI, where in this case, the intensity for LGS is much smaller than its DT.

   In our experiment, we have chosen option (iii) because the driving beam is divergent at that point. Assuming that the MIR waves emerge from both crystals with flat wavefronts and then diverge, we anticipate that the wavefronts will align better in this configuration. However, it's worth noting that these considerations are currently speculative, and it would be highly valuable to obtain a comprehensive quantitative understanding of these effects. Therefore, conducting a thorough investigation of these three options, preferably through theoretical analysis and experimentation, and determining the optimal position for each crystal could potentially lead to a significant increase in the output power of the generated MIR radiation.

5. Investigate the impact of the first crystal (LIO) on the duration of the driving pulse and explore potential solutions to enhance the chirp of the NIR driving pulse following its passage through the LIO, such as utilizing appropriate dispersive elements (e.g., a pair of wedges) between consecutive nonlinear crystals [19].

By pursuing these directions of further development, we anticipate substantial improvements in the performance, versatility, and practicality of our MIR radiation source as an FRS instrument. These advancements will enable a wide range of applications in fields such as spectroscopy, material science, biomedical research, and environmental monitoring, opening up new avenues for scientific discoveries and technological advancements.

Bibliography

[1] *HITRAN on the Web.*

[2] F. Adler, K.C. Cossel, M.J. Thorpe, I. Hartl, M.E. Fermann und J. Ye, *Optics Letters* **34** (2009), 1330. Publisher: Optica Publishing Group.

[3] C.K. Akhgar, G. Ramer, M. Żbik, A. Trajnerowicz, J. Pawluczyk, A. Schwaighofer und B. Lendl, *Analytical Chemistry* **92** (2020), 9901. Publisher: American Chemical Society.

[4] T. Amochkina, D. Hahner, M. Trubetskov, H. Kassab, I. Pupeza, F. Krausz und V. Pervak: *Ultra-Broadband Near-Infrared/Mid-Infrared Beamsplitter for Bio-Medical Laser Applications. Ultra-Broadband Near-Infrared/Mid-Infrared Beamsplitter for Bio-Medical Laser Applications*, In *Optical Interference Coatings Conference (OIC) 2022 (2022), paper TA.11.* Optica Publishing Group (Juni 2022) Seite TA.11.

[5] T. Amochkina und M. Trubetskov, *Applied Optics* **62** (2023), B63. Publisher: Optica Publishing Group.

[6] K. Araki, N. Yagi, Y. Ikemoto, H. Yagi, C.J. Choong, H. Hayakawa, G. Beck, H. Sumi, H. Fujimura, T. Moriwaki, Y. Nagai, Y. Goto und H. Mochizuki, *Scientific Reports* **5** (2015), 17625. Number: 1 Publisher: Nature Publishing Group.

[7] F. Arecchi und R. Bonifacio, *IEEE Journal of Quantum Electronics* **1** (1965), 169. Conference Name: IEEE Journal of Quantum Electronics.

[8] M.J. Baker, S.R. Hussain, L. Lovergne, V. Untereiner, C. Hughes, R.A. Lukaszewski, G. Thiéfin und G.D. Sockalingum, *Chemical Society Reviews* **45** (2016), 1803. Publisher: The Royal Society of Chemistry.

[9] M.J. Baker, J. Trevisan, P. Bassan, R. Bhargava, H.J. Butler, K.M. Dorling, P.R. Fielden, S.W. Fogarty, N.J. Fullwood, K.A. Heys, C. Hughes, P. Lasch, P.L. Martin-Hirsch, B. Obinaju, G.D. Sockalingum, J. Sulé-Suso, R.J. Strong, M.J. Walsh, B.R. Wood, P. Gardner und F.L. Martin, *Nature Protocols* **9** (2014), 1771.

[10] P. Balla, A.B. Wahid, I. Sytcevich, C. Guo, A.L. Viotti, L. Silletti, A. Cartella, S. Alisauskas, H. Tavakol, U. Grosse-Wortmann, A. Schönberg, M. Seidel, A. Trabattoni, B. Manschwetus, T. Lang, F. Calegari, A. Couairon, A. L'Huillier, C.L. Arnold, I. Hartl und C.M. Heyl, *Optics Letters* **45** (2020), 2572. Publisher: Optica Publishing Group.

[11] A. Baltuška, T. Fuji und T. Kobayashi, *Physical Review Letters* **88** (2002), 133901. Publisher: American Physical Society.

[12] G. Barbiero, H. Wang, M. Grassl, S. Groebmeyer, D. Kimbaras, M. Neuhaus, V. Pervak, T. Nubbemeyer, H. Fattahi und M.F. Kling, *Optics Letters* **46** (2021), 5304. Place: Washington Publisher: Optical Soc Amer WOS:000713723300004.

[13] A. Barth und P.I. Haris: *Biological and Biomedical Infrared Spectroscopy.* IOS Press, 2009.

[14] B. Bernhardt, A. Ozawa, P. Jacquet, M. Jacquey, Y. Kobayashi, T. Udem, R. Holzwarth, G. Guelachvili, T.W. Hänsch und N. Picqué, *Nature Photonics* **4** (2010), 55. Number: 1 Publisher: Nature Publishing Group.

[15] J. Biegert, P.K. Bates und O. Chalus, *IEEE Journal of Selected Topics in Quantum Electronics* **18** (2012), 531.

[16] N. Bloembergen, R.K. Chang, S.S. Jha und C.H. Lee, *Physical Review* **174** (1968), 813. Publisher: American Physical Society.

[17] R. Bonifacio, R.M. Caloi und C. Maroli, *Optics Communications* **101** (1993), 185.

[18] A. Bonvalet, M. Joffre, J.L. Martin und A. Migus, *Applied Physics Letters* **67** (1995), 2907.

[19] Q. Bournet, Q. Bournet, M. Jonusas, A. Zheng, F. Guichard, M. Natile, Y. Zaouter, M. Joffre, A. Bonvalet, F. Druon, M. Hanna und P. Georges, *Optics Letters* **47** (2022), 4885. Publisher: Optica Publishing Group.

[20] Q. Bournet, F. Guichard, M. Natile, Y. Zaouter, M. Joffre, A. Bonvalet, I. Pupeza, C. Hofer, F. Druon, M. Hanna und P. Georges, *Optics Letters* **47** (2022), 261.

[21] T. Brabec und F. Krausz, *Reviews of Modern Physics* **72** (2000), 545. Publisher: American Physical Society.

[22] M. Brandstetter, L. Volgger, A. Genner, C. Jungbauer und B. Lendl, *Applied Physics B* **110** (2013), 233.

[23] C. Bree, A. Demircan und G. Steinmeyer, *IEEE Journal of Quantum Electronics* **46** (2010), 433.

[24] J. Brons, V. Pervak, D. Bauer, D. Sutter, O. Pronin und F. Krausz, *Optics Letters* **41** (2016), 3567. Publisher: Optica Publishing Group.

[25] T. Buberl, A. Alismail, H. Wang, N. Karpowicz und H. Fattahi, *Optics Express* **24** (2016), 10286.

[26] T.P. Butler, D. Gerz, C. Hofer, J. Xu, C. Gaida, T. Heuermann, M. Gebhardt, L. Vamos, W. Schweinberger, J.A. Gessner, T. Siefke, M. Heusinger, U. Zeitner, A. Apolonski, N. Karpowicz, J. Limpert, F. Krausz und I. Pupeza, *Optics Letters* **44** (2019), 1730. Publisher: Optica Publishing Group.

[27] T.P. Butler, N. Lilienfein, J. Xu, N. Nagl, C. Hofer, D. Gerz, K.F. Mak, C. Gaida, T. Heuermann, M. Gebhardt, J. Limpert, F. Krausz und I. Pupeza, *Journal of Physics: Photonics* **1** (2019), 044006. Publisher: IOP Publishing.

[28] F. Böhle, M. Kretschmar, A. Jullien, M. Kovacs, M. Miranda, R. Romero, H. Crespo, U. Morgner, P. Simon, R. Lopez-Martens und T. Nagy, *Laser Physics Letters* **11** (2014), 095401.

[29] Q. Cao, F.X. Kärtner und G. Chang, *Optics Express* **28** (2020), 1369.

[30] A. Catanese, J. Rutledge, M.C. Silfies, X. Li, H. Timmers, A.S. Kowligy, A. Lind, S.A. Diddams und T.K. Allison, *Optics Letters* **45** (2020), 1248. Publisher: Optica Publishing Group.

[31] G. Cerullo, A. Baltuška, O. Mücke und C. Vozzi, *Laser & Photonics Reviews* **5** (2011), 323. _eprint: https://onlinelibrary.wiley.com/doi/pdf/10.1002/lpor.201000013.

[32] B.H. Chen, T. Nagy und P. Baum, *Optics Letters* **43** (2018), 1742. Publisher: Optica Publishing Group.

[33] G. Cinque, M.D. Frogley und R. Bartolini, *Rendiconti Lincei* **22** (2011), 33.

[34] I. Coddington, W.C. Swann und N.R. Newbury, *Physical Review A* **82** (2010), 043817. Publisher: American Physical Society.

[35] W. Demtröder: *Molecular Physics: Theoretical Principles and Experimental Methods*. Wiley, Dezember 2005. Google-Books-ID: btc9AQAAIAAJ.

[36] S.S. Dhillon, M.S. Vitiello, E.H. Linfield, A.G. Davies, M.C. Hoffmann, J. Booske, C. Paoloni, M. Gensch, P. Weightman, G.P. Williams, E. Castro-Camus, D.R.S. Cumming, F. Simoens, I. Escorcia-Carranza, J. Grant, S. Lucyszyn, M. Kuwata-Gonokami, K. Konishi, M. Koch, C.A. Schmuttenmaer, T.L. Cocker, R. Huber, A.G. Markelz, Z.D. Taylor, V.P. Wallace, J.A. Zeitler, J. Sibik, T.M. Korter, B. Ellison, S. Rea, P. Goldsmith, K.B. Cooper, R. Appleby, D. Pardo, P.G. Huggard, V. Krozer, H. Shams, M. Fice, C. Renaud, A. Seeds, A. Stöhr,

M. Naftaly, N. Ridler, R. Clarke, J.E. Cunningham und M.B. Johnston, *Journal of Physics D: Applied Physics* **50** (2017), 043001. Publisher: IOP Publishing.

[37] J. Doherty, G. Cinque und P. Gardner, *Applied Spectroscopy Reviews* **52** (2017), 560. Publisher: Taylor & Francis _eprint: https://doi.org/10.1080/05704928.2016.1250214.

[38] A. Dubietis, G. Jonušauskas und A. Piskarskas, *Optics Communications* **88** (1992), 437.

[39] G.S. Edwards, R.H. Austin, F.E. Carroll, M.L. Copeland, M.E. Couprie, W.E. Gabella, R.F. Haglund, B.A. Hooper, M.S. Hutson, E.D. Jansen, K.M. Joos, D.P. Kiehart, I. Lindau, J. Miao, H.S. Pratisto, J.H. Shen, Y. Tokutake, A.F.G. van der Meer und A. Xie, *Review of Scientific Instruments* **74** (2003), 3207.

[40] U. Elu, M. Baudisch, H. Pires, F. Tani, M.H. Frosz, F. Köttig, A. Ermolov, P.S.J. Russell und J. Biegert, *Optica* **4** (2017), 1024. Publisher: Optica Publishing Group.

[41] U. Elu, L. Maidment, L. Vamos, F. Tani, D. Novoa, M.H. Frosz, V. Badikov, D. Badikov, V. Petrov, P. St. J. Russell und J. Biegert, *Nature Photonics* **15** (2021), 277.

[42] H. Fattahi, H.G. Barros, M. Gorjan, T. Nubbemeyer, B. Alsaif, C.Y. Teisset, M. Schultze, S. Prinz, M. Haefner, M. Ueffing, A. Alismail, L. Vámos, A. Schwarz, O. Pronin, J. Brons, X.T. Geng, G. Arisholm, M. Ciappina, V.S. Yakovlev, D.E. Kim, A.M. Azzeer, N. Karpowicz, D. Sutter, Z. Major, T. Metzger und F. Krausz, *Optica* **1** (2014), 45. Publisher: Optica Publishing Group.

[43] H. Fattahi, A. Schwarz, S. Keiber und N. Karpowicz, *Optics Letters* **38** (2013), 4216.

[44] X. Feng, F. Liu, C. Ning, J. Shi, P. Liu, J. Heng und Z. Zhang, *IEEE Photonics Journal* **13** (2021), 1. Conference Name: IEEE Photonics Journal.

[45] P.A. Franken, A.E. Hill, C.W. Peters und G. Weinreich, *Physical Review Letters* **7** (1961), 118. Publisher: American Physical Society.

[46] K. Fritsch, M. Poetzlberger, V. Pervak, J. Brons und O. Pronin, *Optics Letters* **43** (2018), 4643.

[47] S. G. P. Strohmaier. *ISO 11146-1:2005(en), Lasers and laser-related equipment — Test methods for laser beam widths, divergence angles and beam propagation ratios — Part 1: Stigmatic and simple astigmatic beams*, 1985.

[48] C. Gaida, M. Gebhardt, T. Heuermann, F. Stutzki, C. Jauregui, J. Antonio-Lopez, A. Schülzgen, R. Amezcua-Correa, A. Tünnermann, I. Pupeza und J. Limpert, *Light: Science & Applications* **7** (2018), 94. Number: 1 Publisher: Nature Publishing Group.

[49] G. Gallot und D. Grischkowsky, *JOSA B* **16** (1999), 1204. Publisher: Optica Publishing Group.

[50] H.A. Gebbie und G.A. Vanasse, *Nature* **178** (1956), 432. Number: 4530 Publisher: Nature Publishing Group.

[51] G. Ghosh, *Optics Communications* **163** (1999), 95.

[52] L.v. Grafenstein, M. Bock, D. Ueberschaer, K. Zawilski, P. Schunemann, U. Griebner und T. Elsaesser, *Optics Letters* **42** (2017), 3796. Publisher: Optica Publishing Group.

[53] C. Grebing, M. Müller, J. Buldt, H. Stark und J. Limpert, *Optics Letters* **45** (2020), 6250. Publisher: Optica Publishing Group.

[54] P.R. Griffiths und J.A. de Haseth. *Fourier Transform Infrared Spectrometry, 2nd Edition \textbar Wiley*, 2007. Publication Title: Wiley.com.

[55] S. Gröbmeyer: *High-power few-cycle pulse generation towards the gigawatt frontier.* Ludwig-Maximilians-Universität München, Text.PhDThesis, März 2022.

[56] S. Gröbmeyer, K. Fritsch, B. Schneider, M. Poetzlberger, V. Pervak, J. Brons und O. Pronin, *Applied Physics B* **126** (2020), 159.

[57] J. Haas und B. Mizaikoff, *Annual Review of Analytical Chemistry* **9** (2016), 45. _eprint: https://doi.org/10.1146/annurev-anchem-071015-041507.

[58] P. Hamm und M. Zanni: *Concepts and Methods of 2D Infrared Spectroscopy.* 1. Auflage. Cambridge University Press, Februar 2011.

[59] K. Hashimoto, V.R. Badarla, T. Imamura, T. Ideguchi und T. Ideguchi, *Optics Letters* **46** (2021), 5517. Publisher: Optica Publishing Group.

[60] M. Huber, K.V. Kepesidis, L. Voronina, M. Božić, M. Trubetskov, N. Harbeck, F. Krausz und M. Žigman, *Nature Communications* **12** (2021), 1511. Number: 1 Publisher: Nature Publishing Group.

[61] M. Huber, W. Schweinberger, S.A. Hussain, M. Trubetskov, C. Hofer, M. Zigman, F. Krausz und I. Pupeza: *Field-resolved infrared transmission spectroscopy of strongly absorbing samples. Field-resolved infrared transmission spectroscopy of strongly absorbing samples*, In *2019 Conference on Lasers and Electro-Optics Europe and European Quantum Electronics Conference (2019), paper ch_p_45.* Optica Publishing Group (Juni 2019) Seite ch_p_45.

[62] M. Huber, W. Schweinberger, F. Stutzki, J. Limpert, I. Pupeza und O. Pronin, *Optics Express* **25** (2017), 22499. Publisher: Optica Publishing Group.

[63] M. Huber, M. Trubetskov, S.A. Hussain, W. Schweinberger, C. Hofer und I. Pupeza, *Analytical Chemistry* **92** (2020), 7508. Publisher: American Chemical Society.

[64] R. Huber, A. Brodschelm, F. Tauser und A. Leitenstorfer, *Applied Physics Letters* **76** (2000), 3191.

[65] R. Huber, F. Tauser, A. Brodschelm, M. Bichler, G. Abstreiter und A. Leitenstorfer, *Nature* **414** (2001), 286. Number: 6861 Publisher: Nature Publishing Group.

[66] S.A. Hussain, W. Schweinberger, T. Buberl, C. Hofer und I. Pupeza: *Train of ultrashort mid-infrared pulses with sub-mrad carrier-envelope phase stability. Train of ultrashort mid-infrared pulses with sub-mrad carrier-envelope phase stability*, In *2019 Conference on Lasers and Electro-Optics Europe and European Quantum Electronics Conference (2019), paper ed_6_2*. Optica Publishing Group (Juni 2019) Seite ed_6_2.

[67] N. Ibrakovic, E.W. Larsen, G. Zinner und J. Mauritsson, *The European Physical Journal D* **72** (2018), 148.

[68] C. Jauregui, J. Limpert und A. Tünnermann, *Nature Photonics* **7** (2013), 861. Number: 11 Publisher: Nature Publishing Group.

[69] R.R. Jones, D.C. Hooper, L. Zhang, D. Wolverson und V.K. Valev, *Nanoscale Research Letters* **14** (2019), 231.

[70] R.A. Kaindl, F. Eickemeyer, M. Woerner und T. Elsaesser, *Applied Physics Letters* **75** (1999), 1060.

[71] R.A. Kaindl, D.C. Smith, M. Joschko, M.P. Hasselbeck, M. Woerner und T. Elsaesser, *Optics Letters* **23** (1998), 861. Publisher: Optica Publishing Group.

[72] N. Karpowicz. *NickKarpowicz/LightwaveExplorer*, Januar 2023. Original-date: 2022-03-07T20:43:02Z.

[73] T. Kawamori, P.G. Schunemann und K.L. Vodopyanov: *High-order mid-IR multiphoton absorption and nonlinear refraction in GaP, ZnSe, GaSe, and ZGP crystals. High-order mid-IR multiphoton absorption and nonlinear refraction in GaP, ZnSe, GaSe, and ZGP crystals*, In *Conference on Lasers and Electro-Optics (2021), paper STu4C.1*. Optica Publishing Group (Mai 2021) Seite STu4C.1.

[74] K. Kneipp, H. Kneipp, I. Itzkan, R.R. Dasari und M.S. Feld, *Journal of Physics: Condensed Matter* **14** (2002), R597.

[75] M. Knorr, P. Steinleitner, J. Raab, I. Gronwald, P. Merkl, C. Lange und R. Huber, *Optics Express* **26** (2018), 19059.

[76] M.R. Kole, R.K. Reddy, M.V. Schulmerich, M.K. Gelber und R. Bhargava, *Analytical Chemistry* **84** (2012), 10366. Publisher: American Chemical Society.

[77] A. Kowligy, H. Timmers, A. Lind, U. Elu Etxano, F. Da Cruz, P. Schunemann, J. Biegert und S. Diddams, *Science advances* **5** (2019), eaaw8794.

[78] F. Krausz und M. Ivanov, *Reviews of Modern Physics* **81** (2009), 163. Publisher: American Physical Society.

[79] J. Kröll, J. Darmo, S.S. Dhillon, X. Marcadet, M. Calligaro, C. Sirtori und K. Unterrainer, *Nature* **449** (2007), 698. Number: 7163 Publisher: Nature Publishing Group.

[80] I. Kubat, C.R. Petersen, U.V. Møller, A. Seddon, T. Benson, L. Brilland, D. Méchin, P.M. Moselund und O. Bang, *Optics Express* **22** (2014), 3959. Publisher: Optica Publishing Group.

[81] F.X. Kärtner: *Few-Cycle Laser Pulse Generation and Its Applications*. Springer Science & Business Media, September 2004. Google-Books-ID: wgbno3SFx34C.

[82] C. Kübler, R. Huber, S. Tübel und A. Leitenstorfer, *Applied Physics Letters* **85** (2004), 3360. Publisher: American Institute of Physics.

[83] A. Laubereau und W. Kaiser, *Reviews of Modern Physics* **50** (1978), 607.

[84] A. Leitenstorfer, S. Hunsche, J. Shah, M.C. Nuss und W.H. Knox, *Applied Physics Letters* **74** (1999), 1516. Publisher: American Institute of Physics.

[85] D.M.B. Lesko, H. Timmers, S. Xing, A. Kowligy, A.J. Lind und S.A. Diddams, *Nature Photonics* **15** (2021), 281. Number: 4 Publisher: Nature Publishing Group.

[86] C.H. Lu, T. Witting, A. Husakou, M.J.J. Vrakking, A.H. Kung und F.J. Furch, *Optics Express* **26** (2018), 8941. Publisher: Optica Publishing Group.

[87] R. Mankowsky, M. Först und A. Cavalleri, *Reports on Progress in Physics* **79** (2016), 064503. Publisher: IOP Publishing.

[88] C. Manzoni, O.D. Mücke, G. Cirmi, S. Fang, J. Moses, S.W. Huang, K.H. Hong, G. Cerullo und F.X. Kärtner, *Laser & Photonics Reviews* **9** (2015), 129. _eprint: https://onlinelibrary.wiley.com/doi/pdf/10.1002/lpor.201400181.

[89] P. Maslowski, K.F. Lee, A.C. Johansson, A. Khodabakhsh, G. Kowzan, L. Rutkowski, A.A. Mills, C. Mohr, J. Jiang, M.E. Fermann und A. Foltynowicz, *Physical Review A* **93** (2016), 021802. Publisher: American Physical Society.

[90] B. Mayer, C. Schmidt, J. Bühler, D.V. Seletskiy, D. Brida, A. Pashkin und A. Leitenstorfer, *New Journal of Physics* **16** (2014), 063033. Publisher: IOP Publishing.

[91] P. Merkl, M. Knorr, C. Meineke, L. Kastner, D. Peller und R. Huber, *Optics Letters* **44** (2019), 5521. Publisher: Optica Publishing Group.

[92] G. Mourou, *Reviews of Modern Physics* **91** (2019), 030501. Publisher: American Physical Society.

[93] Z. Movasaghi, S. Rehman und I.U. Rehman, *Applied Spectroscopy Reviews* **42** (2007), 493. Publisher: Taylor & Francis _eprint: https://doi.org/10.1080/05704920701551530.

[94] A.V. Muraviev, V.O. Smolski, Z.E. Loparo und K.L. Vodopyanov, *Nature Photonics* **12** (2018), 209. Number: 4 Publisher: Nature Publishing Group.

[95] U. Møller, Y. Yu, I. Kubat, C.R. Petersen, X. Gai, L. Brilland, D. Méchin, C. Caillaud, J. Troles, B. Luther-Davies und O. Bang, *Optics Express* **23** (2015), 3282. Publisher: Optica Publishing Group.

[96] M. Müller, J. Buldt, H. Stark, C. Grebing und J. Limpert, *Optics Letters* **46** (2021), 2678. Publisher: Optica Publishing Group.

[97] J. Neuhaus, J. Kleinbauer, A. Killi, S. Weiler, D. Sutter und T. Dekorsy, *Optics Letters* **33** (2008), 726. Publisher: Optica Publishing Group.

[98] S. Nie und S.R. Emory, *Science (New York, N.Y.)* **275** (1997), 1102.

[99] D.N. Nikogosyan: *Nonlinear Optical Crystals: A Complete Survey*. 2005. Auflage. Springer, New York, Januar 2005.

[100] M.T. Peschel, M. Högner, T. Buberl, D. Keefer, R. de Vivie-Riedle und I. Pupeza, *Nature Communications* **13** (2022), 5897. Number: 1 Publisher: Nature Publishing Group.

[101] C.R. Petersen, U. Møller, I. Kubat, B. Zhou, S. Dupont, J. Ramsay, T. Benson, S. Sujecki, N. Abdel-Moneim, Z. Tang, D. Furniss, A. Seddon und O. Bang, *Nature Photonics* **8** (2014), 830. Number: 11 Publisher: Nature Publishing Group.

[102] V. Petrov, A. Yelisseyev, L. Isaenko, S. Lobanov, A. Titov und J.J. Zondy, *Applied Physics B* **78** (2004), 543.

[103] N. Picqué und T.W. Hänsch, *Nature Photonics* **13** (2019), 146. Number: 3 Publisher: Nature Publishing Group.

[104] J.J. Pigeon, S.Y. Tochitsky, C. Gong und C. Joshi, *Optics Letters* **39** (2014), 3246. Publisher: Optica Publishing Group.

[105] M. Planck, *Physikalische Blätter* **4** (1900), 146. _eprint: https://onlinelibrary.wiley.com/doi/pdf/10.1002/phbl.19480040404.

[106] M. Planck, *Annalen der Physik* **309** (1901), 553. _eprint: https://onlinelibrary.wiley.com/doi/pdf/10.1002/andp.19013090310.

[107] M. Poetzlberger, J. Zhang, S. Gröbmeyer, D. Bauer, D. Sutter, J. Brons und O. Pronin, *Optics Letters* **44** (2019), 4227. Publisher: Optica Publishing Group.

[108] O. Pronin, M. Seidel, F. Lücking, J. Brons, E. Fedulova, M. Trubetskov, V. Pervak, A. Apolonski, T. Udem und F. Krausz, *Nature Communications* **6** (2015), 6988. Number: 1 Publisher: Nature Publishing Group.

[109] I. Pupeza, M. Huber, M. Trubetskov, W. Schweinberger, S.A. Hussain, C. Hofer, K. Fritsch, M. Poetzlberger, L. Vamos, E. Fill, T. Amotchkina, K.V. Kepesidis, A. Apolonski, N. Karpowicz, V. Pervak, O. Pronin, F. Fleischmann, A. Azzeer, M. Žigman und F. Krausz, *Nature* **577** (2020), 52. Number: 7788 Publisher: Nature Publishing Group.

[110] I. Pupeza, D. Sánchez, J. Zhang, N. Lilienfein, M. Seidel, N. Karpowicz, T. Paasch-Colberg, I. Znakovskaya, M. Pescher, W. Schweinberger, V. Pervak, E. Fill, O. Pronin, Z. Wei, F. Krausz, A. Apolonski und J. Biegert, *Nature Photonics* **9** (2015), 721. Number: 11 Publisher: Nature Publishing Group.

[111] L. Quaroni, *Infrared Physics & Technology* **105** (2020), 102779.

[112] D. Rand, D. Miller, D.J. Ripin und T.Y. Fan, *Optical Materials Express* **1** (2011), 434. Publisher: Optica Publishing Group.

[113] P. Rauter und F. Capasso, *Laser & Photonics Reviews* **9** (2015), 452. _eprint: https://onlinelibrary.wiley.com/doi/pdf/10.1002/lpor.201500095.

[114] C. Riek, D.V. Seletskiy, A.S. Moskalenko, J.F. Schmidt, P. Krauspe, S. Eckart, S. Eggert, G. Burkard und A. Leitenstorfer, *Science* **350** (2015), 420.

[115] D. Roberts, *IEEE Journal of Quantum Electronics* **28** (1992), 2057. Conference Name: IEEE Journal of Quantum Electronics.

[116] Q. Ru, T. Kawamori, P.G. Schunemann, S. Vasilyev, S.B. Mirov, S.B. Mirov und K.L. Vodopyanov, *Optics Letters* **46** (2021), 709. Publisher: Optica Publishing Group.

[117] P. Russbueldt, D. Hoffmann, M. Höfer, J. Löhring, J. Luttmann, A. Meissner, J. Weitenberg, M. Traub, T. Sartorius, D. Esser, R. Wester, P. Loosen und R. Poprawe, *IEEE Journal of Selected Topics in Quantum Electronics* **21** (2015), 447. Conference Name: IEEE Journal of Selected Topics in Quantum Electronics.

[118] D. Sanchez, M. Hemmer, M. Baudisch, S.L. Cousin, K. Zawilski, P. Schunemann, O. Chalus, C. Simon-Boisson und J. Biegert, *Optica* **3** (2016), 147. Publisher: Optica Publishing Group.

[119] A. Schliesser, N. Picqué und T.W. Hänsch, *Nature Photonics* **6** (2012), 440. Number: 7 Publisher: Nature Publishing Group.

[120] O. Schubert, M. Hohenleutner, F. Langer, B. Urbanek, C. Lange, U. Huttner, D. Golde, T. Meier, M. Kira, S.W. Koch und R. Huber, *Nature Photonics* **8** (2014), 119. Number: 2 Publisher: Nature Publishing Group.

[121] J. Schulte, T. Sartorius, J. Weitenberg, A. Vernaleken und P. Russbueldt, *Optics Letters* **41** (2016), 4511. Publisher: Optica Publishing Group.

[122] A. Schwaighofer, M. Brandstetter und B. Lendl, *Chemical Society Reviews* **46** (2017), 5903. Publisher: The Royal Society of Chemistry.

[123] M. Seidel, J. Brons, G. Arisholm, K. Fritsch, V. Pervak und O. Pronin, *Scientific Reports* **7** (2017), 1410. Number: 1 Publisher: Nature Publishing Group.

[124] M. Seidel, X. Xiao, S.A. Hussain, G. Arisholm, A. Hartung, K.T. Zawilski, P.G. Schunemann, F. Habel, M. Trubetskov, V. Pervak, O. Pronin und F. Krausz, *Science Advances* **4** (2018), eaaq1526. Publisher: American Association for the Advancement of Science.

[125] A. Sell, A. Leitenstorfer und R. Huber, *Optics Letters* **33** (2008), 2767. Publisher: Optica Publishing Group.

[126] A. Sennaroglu und J.G. Fujimoto, *Optics Express* **11** (2003), 1106. Publisher: Optica Publishing Group.

[127] T. Steinle, F. Mörz, A. Steinmann und H. Giessen, *Optics Letters* **41** (2016), 4863. Publisher: Optica Publishing Group.

[128] P. Steinleitner, N. Nagl, M. Kowalczyk, J. Zhang, V. Pervak, C. Hofer, A. Hudzikowski, J. Sotor, A. Weigel, F. Krausz und K.F. Mak, *Nature Photonics* **16** (2022), 512. Number: 7 Publisher: Nature Publishing Group.

[129] P. Sulzer, M. Högner, A.K. Raab, L. Fürst, E. Fill, D. Gerz, C. Hofer, L. Voronina und I. Pupeza, *Nature Photonics* **16** (2022), 692. Number: 10 Publisher: Nature Publishing Group.

[130] P. Sulzer, K. Oguchi, J. Huster, M. Kizmann, T.L.M. Guedes, A. Liehl, C. Beckh, A.S. Moskalenko, G. Burkard, D.V. Seletskiy und A. Leitenstorfer, *Physical Review A* **101** (2020), 033821.

[131] K. Tian, L. He, X. Yang und H. Liang, *Photonics* **8** (2021), 290. Number: 8 Publisher: Multidisciplinary Digital Publishing Institute.

[132] H. Timmers, A. Kowligy, A. Lind, F.C. Cruz, N. Nader, M. Silfies, G. Ycas, T.K. Allison, P.G. Schunemann, S.B. Papp und S.A. Diddams, *Optica* **5** (2018), 727. Publisher: Optica Publishing Group.

[133] C.L. Tsai, F. Meyer, A. Omar, Y. Wang, A.Y. Liang, C.H. Lu, M. Hoffmann, S.D. Yang und C.J. Saraceno, *Optics Letters* **44** (2019), 4115. Publisher: Optica Publishing Group.

[134] P. Täschler, M. Bertrand, B. Schneider, M. Singleton, P. Jouy, F. Kapsalidis, M. Beck und J. Faist, *Nature Photonics* **15** (2021), 919.

[135] T. Udem, R. Holzwarth und T.W. Hänsch, *Nature* **416** (2002), 233. Number: 6877 Publisher: Nature Publishing Group.

[136] J. Valdmanis und G. Mourou, *IEEE Journal of Quantum Electronics* **22** (1986), 69. Conference Name: IEEE Journal of Quantum Electronics.

[137] D.F. Vanderwerf: *The Story of Light Science*. Springer International Publishing, Cham, 2017.

[138] S. Vasilyev, I.S. Moskalev, V.O. Smolski, J.M. Peppers, M. Mirov, A.V. Muraviev, K. Zawilski, P.G. Schunemann, S.B. Mirov, K.L. Vodopyanov und V.P. Gapontsev, *Optica* **6** (2019), 111. Publisher: Optica Publishing Group.

[139] E. Vicentini, Y. Wang, D. Gatti, A. Gambetta, P. Laporta, G. Galzerano, K. Curtis, K. McEwan, C.R. Howle und N. Coluccelli, *Optics Express* **28** (2020), 4541. Publisher: Optica Publishing Group.

[140] M.S. Vitiello, G. Scalari, B. Williams und P.D. Natale, *Optics Express* **23** (2015), 5167. Publisher: Optica Publishing Group.

[141] R. W. Boyd, (2008).

[142] M.L. Weichman, P.B. Changala, J. Ye, Z. Chen, M. Yan und N. Picqué, *Journal of Molecular Spectroscopy* **355** (2019), 66.

[143] J. Weitenberg, T. Saule, J. Schulte und P. Rußbüldt, *IEEE Journal of Quantum Electronics* **53** (2017), 1. Conference Name: IEEE Journal of Quantum Electronics.

[144] J. Weitenberg, A. Vernaleken, J. Schulte, A. Ozawa, T. Sartorius, V. Pervak, H.D. Hoffmann, T. Udem, P. Russbüldt und T.W. Hänsch, *Optics Express* **25** (2017), 20502. Publisher: Optica Publishing Group.

[145] Q. Wu und X. Zhang, *Applied Physics Letters* **67** (1995), 3523. Publisher: American Institute of Physics.

[146] S. Xing, A.S. Kowligy, D.M.B. Lesko, A.J. Lind und S.A. Diddams, *Optics Letters* **45** (2020), 2660. Publisher: Optica Publishing Group.

[147] Y. Yu, X. Gai, P. Ma, D.Y. Choi, Z. Yang, R. Wang, S. Debbarma, S.J. Madden und B. Luther-Davies, *Laser & Photonics Reviews* **8** (2014), 792. _eprint: https://onlinelibrary.wiley.com/doi/pdf/10.1002/lpor.201400034.

[148] T. Zentgraf, R. Huber, N.C. Nielsen, D.S. Chemla und R.A. Kaindl, *Optics Express* **15** (2007), 5775. Publisher: Optica Publishing Group.

[149] J. Zhang, K. Fai Mak, N. Nagl, M. Seidel, D. Bauer, D. Sutter, V. Pervak, F. Krausz und O. Pronin, *Light: Science & Applications* **7** (2018), 17180. Number: 2 Publisher: Nature Publishing Group.

[150] J. Zhang, K. Fritsch, Q. Wang, F. Krausz, K.F. Mak und O. Pronin, *Optics Letters* **44** (2019), 2986. Place: Washington Publisher: Optical Soc Amer WOS:000471636700011.

List of Publications

1. T. Amochkina, D. Hahner, M. Trubetskov, **H. Kassab**, I. Pupeza, F. Krausz, and V. Pervak, "Ultra-Broadband Near-Infrared/Mid-Infrared Beamsplitter for Bio-Medical Laser Applications," in Optical Interference Coatings Conference (OIC) 2022 (2022), Paper TA.11 (Optica Publishing Group, 2022), p. TA.11.

2. **Hadil Kassab**, Sebastian Gröbmeyer, Wolfgang Schweinberger, Christina Hofer, Philipp Steinleitner, Maximilian Högner, Tatiana Amotchkina, Daniel Gerz, Matthias Knorr, Rupert Huber, Nicholas Karpowicz, and Ioachim Pupeza, "In-line synthesis of multi-octave phase-stable infrared light," in Optics Express, https://doi.org/10.1364/OE.493887

3. **Hadil Kassab**, Sebastian Gröbmeyer, Christina Hofer, Wolfgang Schweinberger, Philipp Steinleitner, Maximilian Högner, Tatiana Amotchkina, Matthias Knorr, Rupert Huber, Ferenc Krausz, Nicholas Karpowicz, Ioachim Pupeza, "Bright phase-stable waveforms covering the entire infrared molecular fingerprint region," in CLEO/Europe-EQEC Conference 2023

4. Simon Reiger, Mikhail Mamaikin, Dmitrii Kormin, Keyhan Golyari, **Hadil Kassab**, Maximilian Seeger, Volodymyr Pervak, Nicholas Karpowicz, Thomas Nubbemeyer, "Ultra-phase-stable infrared light source at Watt level," Submitted to Optica

Data Archiving

The experimental raw data, evaluation files, and figures can be found on the Data archive server of the Laboratory for Attosecond Physics at the Max Planck Institute of Quantum Optics:
$/afs/ipp-garching.mpg.de/mpq/lap/publication_archive/Theses/2023/HadilKassab(PhD)$
The main folder has five sub-folders for each chapter individually. In each of those sub-folders, there are sub-sub-folders for each of the figures and the raw data. There is also a Read-Me text file in each sub-folder and the mine folder. In case there was any python code used, it was also added.

Danksagung

Thanks to all my colleagues, Attoworld group, supervisors, and doctorate father, Ferenc, as well as to my family members for helping me to finish this Ph.D. without your contribution and support it would not have been possible!